Best Available Copy

AD-784 356

LASER-INTERACTION STUDIES. PART 1. A THEORETICAL INVESTIGATION OF LASER SUPPORTED COMBUSTION WAVES. PART 2. MEASUREMENTS OF THE EFFECT OF PARTI-CULATE, MATTER ON AIR BREAKDOWN BY 1.06u

A. A. Boni, et al

Systems Science and Software

SECURITY CLASSIFICATION OF THIS PAGE (When Data Entered)

REPORT DOCUMENTATION PAGE	READ INSTRUCTIONS BEFORE COMPLETING FORM

1 REPORT NUMBER	2. GOVT ACCESSION NO.	3 RECIPIENT'S CATALOG NUMBER
		AD 784356

4 TITLE (and Subtitle) Laser-Interaction Studies Part 1: A Theoretical Investigation of Laser Supported Combustion Waves Part 2: Measurements on the Effect of Particulate Matter on Air Breakdown by 1.06μ Laser Radiation	5 TYPE OF REPORT & PERIOD COVERED
	6 PERFORMING ORG. REPORT NUMBER SSS-R-74-2344

7 AUTHOR(s) Part 1: A.A. Boni, F.Y. Su, H.D. Cohen Part 2: A.A. Boni, D. Meskan	8 CONTRACT OR GRANT NUMBER(s) DAAH01-74-C-0386

9 PERFORMING ORGANIZATION NAME AND ADDRESS Systems, Science and Software Post Office Box 1620 La Jolla, California 92037	10 PROGRAM ELEMENT, PROJECT, TASK AREA & WORK UNIT NUMBERS

11 CONTROLLING OFFICE NAME AND ADDRESS Defense Advanced Research Projects Agency Washington, D.C.	12 REPORT DATE August 1974
	13 NUMBER OF PAGES

14 MONITORING AGENCY NAME & ADDRESS(if different from Controlling Office) U.S. Army Missile Command Redstone Arsenal Alabama 35809	15 SECURITY CLASS (of this report) Unclassified
	15a DECLASSIFICATION DOWNGRADING SCHEDULE

16 DISTRIBUTION STATEMENT (of this Report)

17 DISTRIBUTION STATEMENT (of the abstract entered in Block 20, if different from Report)

18 SUPPLEMENTARY NOTES

19 KEY WORDS (Continue on reverse side if necessary and identify by block number)

laser supported combustion wave
quasi-linearization
pulsed propagation
particle-induced air breakdown
laser-interaction with carbon and SiO_2 fibers

20 ABSTRACT (Continue on reverse side if necessary and identify by block number)

Two separate non-linear effects which influence pulsed laser propagation and target interaction have been studied, e.g., laser supported combustion wave (LSC) propagation and laser-induced gas breakdown. A theoretical model describing LSC propagation and which includes the non-linear contributions of the plasma transport and thermodynamic coefficients throughout the wave profile has been developed. The model is one-dimensional and the system of equations is solved by use of the method of quasilinearization. The model

DD FORM 1473 EDITION OF 1 NOV 65 IS OBSOLETE

i

utilizes the deflagration approximation which implies that pressure balance with the atmosphere exists. Numerical results of our calculations are in good quantitative agreement with available experimental data. Further numerical calculations have been performed by use of a one-dimensional, variable area hydrodynamic code. It is found that a precursor shock wave which is driven by the LSC wave precedes the LSC wave and that attainment of pressure balance with the atmosphere does not occur on a time and spatial scale consistent with experimental observations. These calculations have been performed including radial mass loss and beam divergence effects. It is postulated that two-dimensional' flow effects in the vicinity of the target, which have not been specifically included in the calculation may be important. Inclusion of such effects on an ad hoc basis results in good correlation with experimental data.

Experiments have been performed to determine the effect of particulate matter on laser-induced air breakdown for Nd laser wavelengths (1.06μ) and for pulse widths of 30 nsec. We have measured breakdown thresholds for air in the presence of SiO_2 and carbon fibers of 9μ, 6.6μ and 68μ diameters. It has been found that, as for interaction at 10.6μ, the breakdown thresholds are reduced due to the presence of particulate matter. Furthermore, the results obtained by us at 1.06μ are consistent with previous measurements at 10.6μ assuming that the breakdown threshold scales inversely until the square of the laser wavelength.

i a

SYSTEMS, SCIENCE AND SOFTWARE

SSS-R-74-2344

LASER-INTERACTION STUDIES

A Final Report

Part 1: A Theoretical Investigation of
Laser Supported Combustion Waves

Part 2: Measurements of the Effect of
Particulate Matter on Air Breakdown by 1.06μ

by

A.A. Boni
H.D. Cohen
D.A. Meskan
F.Y. Su

The views and conclusions contained in this document are those
of the authors and should not be interpreted as necessarily
representing the official policies, either or implied, of the
Defense Advanced Research Projects Agency of the U.S. Government.

Sponsored by:
DEFENSE ADVANCED RESEARCH PROJECTS AGENCY
DARPA Order No. 2113
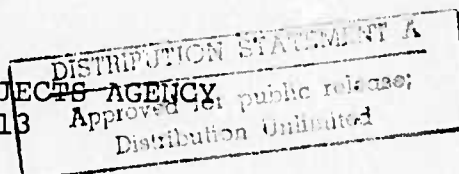
August 1974

ib

Part 1: A Theoretical Investigation of
Laser Supported Combustion Waves

A.A. Boni

H.D. Cohen

F.Y. Su

ic

ABSTRACT

Two separate non-linear effects which influence pulsed laser propagation and target interaction have been studied, e.g., laser supported combustion wave (LSC) propagation and laser-induced gas breakdown. A theoretical model describing LSC propagation and which includes the non-linear contributions of the plasma transport and thermodynamic coefficients throughout the wave profile has been developed. The model is one-dimensional and the system of equations is solved by use of the method of quasilinearization. The model utilizes the deflagration approximation which implies that pressure balance with the atmosphere exists. Numerical results of our calculations are in good quantitative agreement with available experimental data. Further numerical calculations have been performed by use of a one-dimensional, variable area hydrodynamic code. It is found that a precursor shock wave which is driven by the LSC wave precedes the LSC wave and that attainment of pressure balance with the atmosphere does not occur on a time and spatial scale consistent with experimental observations. These calculations have been performed including radial mass loss and beam divergence effects. It is postulated that two-dimensional flow effects in the vicinity of the target, which have not been specifically included in the calculation may be important. Inclusion of such effects on an <u>ad hoc</u> basis results in good correlation with experimental data.

Experiments have been performed to determine the effect of particulate matter on laser-induced air breakdown for Nd laser wavelengths (1.06μ) and for pulse widths of 30 nsec. We have measured breakdown thresholds for air in the presence of SiO_2 and carbon fibers of 9μ, 6.6μ and 68μ diameters. It

has been found that, as for interaction at 10.6µ, the break-down thresholds are reduced due to the presence of particulate matter. Furthermore, the results obtained by us at 1.06µ are consistent with previous measurments at 10.6µ assuming that the breakdown threshold scales inversely with the square of the laser wavelength.

ACKNOWLEDGEMENTS

CONTENTS   Page

1. INTRODUCTION AND SUMMARY

The work described in this report was performed at Systems, Science and Software (S^3) during the period 21 December 1973 through 21 June 1974 on Contract No. DAAH01-74-C-0386. The objective of the work is twofold; (1) to develop a theoretical model including a description of the various non-linear effects for laser supported combustion wave (LSC) propagation, and (2) to perform measurements at 1.06µ to determine the effect of particulate matter on laser-induced air breakdown. The latter work was performed by S^3 personnel at the Battelle Columbus Laboratories under a subcontract from S^3.

Previous work[1-6] has shown the existence of LSC waves initiated at target surfaces for laser fluxes as low as 4×10^4 watts/cm^2 for CO_2 laser radiation. The existence of such wave phenomena has important implications regarding the delivery of laser radiation directly to the surface since the waves are highly absorptive. Raizer[4] argued that the propagation and structure of such waves could be adequately described by a one-dimensional model which included propagation of the wave away from the surface by thermal conduction. He utilized a linearized analysis of the gasdynamics conservation equations to obtain estimates for the wave velocity as a function of the incident laser flux. The work at Mathematical Sciences Northwest[3] showed that the LSC wave velocity was much greater (about an order of magnitude) than could be predicted from Raizer's theory, and that the velocity did not scale with flux according to Raizer's prescription. Subsequently, we pointed out that in addition to thermal conduction, the transport of thermal radiation in the vacuum ultraviolet region was the dominant wave transport mechanism.[4,5]

Indeed, the order of magnitude discrepancy with experiment
was removed. However, our analysis was also based on a
linearized model. The present work, which is an extension
of of our previous work, removes the linearized assumptions
and includes the non-linear variation of transport and thermo-
dynamic coefficients in the analysis. Two separate analyses
are presented in Chapters 2 and 3. In Chapter 2, we utilize
the method of quasilinearization to solve the LSC propagation
problem. It is shown that the non-linear features of the
problem are profound and that by taking them into account,
good agreement is found with the MSNW[3] experimental results.

However, this work utilizes the deflagration approxima-
tion, i.e., the pressure ahead of and through the wave is
approximated as a constant. To verify this assumption and to
study the importance of potential 2-D effects, we describe in
Chapter 3 some numerical calculations based on a one-dimensional
variable-area hydrodynamics code. These calculations indicate
that a precursor shock wave exists ahead of the LSC wave, thus
jeopardizing the validity of the deflagration approximation.
It is shown that radial expansion of the laser-heated plasma
beyond the confines of the laser beam is not a significant
loss mechanism. However, we do find that the presence of the
target results in higher wave velocities than are predicted
by previous analyses. These velocities are higher than those
observed experimentally[3] at similar distances from the tar-
get. We conclude that mass loss from the plasma in the vicinity
of the target must be responsible for this more rapid attainment
of pressure balance with the atmosphere. Upon presuming on an
ad hoc basis the presence of such a loss mechanism, our calcu-
lations are in good agreement with the MSNW data as well as
with those results described in Chapter 2.

2

Finally, in Chapter 4, we discuss measurements performed by us at 1.06μ to determine the wavelength and pulse length scaling which exists between 10.6μ and 1.06μ and for pulse length variations between 300 nsec and 30 nsec. We performed measurements on SiO_2 and carbon fibers in an air environment and find significant reductions in the laser-induced breakdown threshold from the clean air value. For example, we find for a 68μ carbon fiber a reduction in breakdown threshold to 2.3×10^{10} watts/cm^2. A full order of magnitude less than the clean air value.

It is shown that the breakdown phenomena at both 10.6μ and 1.06μ are similar and that the breakdown thresholds (for a particular pulse length) scale as the inverse square of the wavelength. This conclusion is consistent with arguments based on inverse bremsstrahlung as the dominant absorption process.

2. NONLINEAR THEORY OF LASER SUPPORTED COMBUSTION WAVES

2.1 INTRODUCTION

It has been observed experimentally[1,2,3] that a sub-sonic wave can propagate and is supported by the addition of energy, e.g., laser radiation. The earlier theoretical work on laser supported combustion wave (LSC) propagation was based on a one-dimensional linear theory including thermal conduction as the only energy transport mechanism.[4] Later, it was pointed out by Boni and Su that thermal radiation in the vacuum ultraviolet (VUV) spectrum is the dominant energy transfer mechanism.[5] Depending upon the absorption coeffi-cient in the VUV band, we have demonstrated that the wave velocity can vary linearly (when the vacuum ultraviolet pre-cursor is not optically thick) with the incident flux or as a square root function of the incident laser flux (when the precursor can be considered as optically thick).[6] However, all the above results are based on analyses which result from a linearization of the governing equations. In order to obtain a better understanding of the interaction between the laser radiation and gasdynamic processes involved in LSC pro-pagation, a detailed treatment of the problem, which includes a description of the various non-linear effects is required. In this report, we first set up a nonlinear mathematical model for a one-dimensional steady state LSC wave propagating into air with real gasdynamic properties. Then we proceed to solve the problem by use of the method of quasilinearization,[7] which has been used quite extensively in boundary layer theory.[8,9,10] Since the equation is nonlinear, there are certain difficulties associated with the process of obtaining a convergent solution. We discuss these difficulties and finally present some solutions and compare with available experimental data.

2.2 FORMULATION OF THE PROBLEM

Assume a parallel, axially-symmetric laser beam with an intensity lower than the breakdown flux ($\leq 10^7$ watts/cm^2) incident onto a partially absorbing gas. Since the laser radiation cannot support a laser supported detonation (LSD) wave, any initial shock waves present due to target interaction have propagated far beyond the light-absorbing plasma. Therefore, we assume that the pressure in the absorption wave has equilibrated with the ambient and a constant pressure process is obtained.

Although it has been suggested that two-dimensional effects are important,[3] in this study we assume a one-dimension planar geometry in order to simplify the problem. However, the heat diffusion through the radial direction will be approximately included as Raizer suggested.[4] In Section 3, the two-dimensional (2-D) effects are studied by using a quasi one-dimensional approach and discussed.

We assume for the present that a continuous laser source is used such that the LSC can propagate at a steady speed, v_o, into the ambient gas with density ρ_o and temperature T_o. Accordingly, coordinates are transformed into the wave frame (Figure 1). In this coordinate system, the continuity equations can be simply integrated to give:

$$\rho u = \rho_o v_o \quad , \tag{1}$$

where ρ and u are the density and local velocity at any position in the wave. The energy equation can also be written as

$$\rho u \frac{dh}{dx} = \frac{d}{dx} \left(\lambda_c \frac{dT}{dx} \right) - \frac{dF_r}{dx} + \frac{d\phi}{dx} - j_c \quad , \tag{2}$$

5
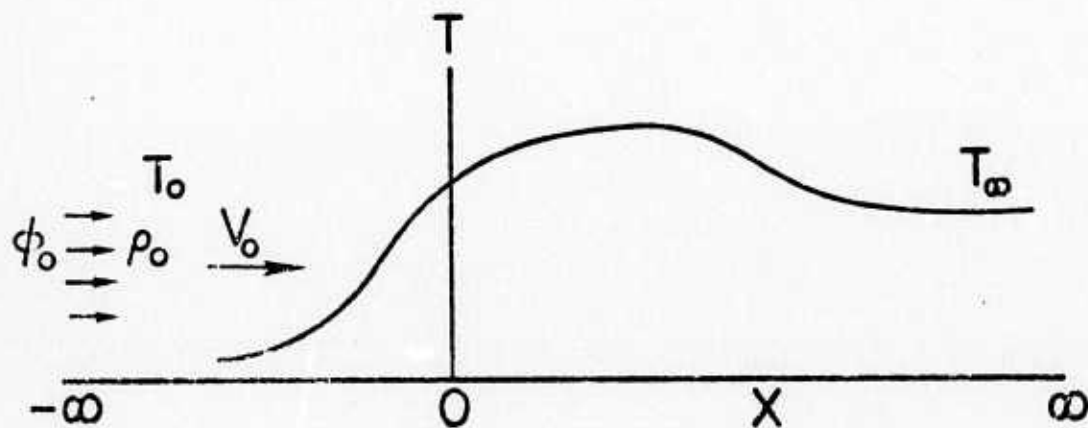
Figure 1   Schematic diagram for the propagation of LSC.

6

where h is the specific enthalpy and λ_c is the thermal conductivity. In the above equation, radiative transport is included through the terms F_r which is the integrated flux, and ψ which is the incident laser flux. The term j_c represents the volumetric energy loss through the lateral surface of the light channel. Assuming the plasma in the light channel to behave like a heated cylinder with strongly cooled walls, one can show that the two dimensional heat loss by conduction through the channel walls can be approximated as

$$j_c \; \alpha \; \frac{A \displaystyle\int_0^T \lambda_c dT}{R^2} \; , \tag{3}$$

where A is a constant of order of unity.[4]

The volumetric laser heating term obeys the following transport equation;

$$\frac{d\phi}{dx} = k_L \phi$$

with the boundary condition $\phi = \phi_0$ at $x = -\infty$ and k_L is the linear absorption coefficient (cm^{-1}).

The are three boundary conditions which the system of equations (1) and (2) must satisfy. At the far upstream boundary, the gas is cold at a temperature T_0, and also the thermal flux vanishes, i.e.,

$$T = T_0 \tag{4}$$

$$\left. \begin{array}{c} \\ \\ \\ \end{array} \right\} \quad \text{at } x = -\infty \; .$$

$$\frac{dT}{dx} = 0 \tag{5}$$

On the other hand, far downstream, the energy gain through absorption of the laser energy must be balanced by the energy loss through radiation and conduction; therefore

$$\frac{dT}{dx} = 0 \qquad at \qquad x = \infty \tag{6}$$

Hence the problem becomes an eigenvalue problem. A unique solution exists only at a discrete value of the velocity, v_o, which is the eigenvalue. This velocity is the one at which the wave propagates.

2.3   RADIATIVE AND GASDYNAMIC PROPERTIES OF THE PLASMA

In a high-temperature plasma, the absorption coefficient of the laser light with frequency v is dominated by the free-free bremsstrahlung radiation of electrons in both the ionic and atomic fields. The absorption coefficient for ionic bremsstrahlung may be calculated by the Kramer's formula, corrected for stimulated emission given below, [11]

$$k_L = \frac{4}{3} \left(\frac{2\pi}{3m_e kT}\right)^{1/2} \frac{z^2 e^6}{hcm_e v^3} N_+ N_e \; G\left[1 - e^{-h\nu/kT}\right] \; . \tag{7}$$

Here G is the Gaunt factor

$$G = \frac{\sqrt{3}}{\pi} \; \ell n \left(\frac{4kT}{Ze^2 N_e^{1/3}}\right) \qquad . \tag{8}$$

Assuming for the present that the state of ionization may be described by the Saha equation, [11] the number density of electrons (N_e) or ions (N_+) can then be calculated according to

$$\frac{N_e^2}{N - 2N_e} = 2\left(\frac{2 \; m_e kT}{h^2}\right)^{3/2} \frac{g_+}{g_a} \; e^{-I/kT} \quad ,$$

8

where N is the total number density ($N = P/kT$), where P is the total pressure due to atoms, ions, and electrons. The ratio g_+/g_a is approximately 1.9 for air, whereas the averaged ionization potential is given as 14.4 eV.[4]

As we have demonstrated before,[5] thermal radiation processes are very important for the gas in the temperature range from 1 eV to 2 eV. Since radiative properties are frequency dependent, it is common practice to use a step model (or a band model) in most of the high temperature gasdynamic calculations. Such a model consists of a different constant mean absorption coefficient in various frequency ranges. In this report, for simplicity, we adopt the two-step absorption coefficient model (Figure 2) to investigate the nonlinear effects of LSC wave propagation. Accordingly, the integrated radiative flux can be separated into two parts, $F = F_1 + F_2$, where F_1 covers the visible and infrared portions of the spectrum, and F_2 covers the vacuum ultraviolet (VUV) portion of the spectrum. The linear absorption coefficients, k_1 and k_2, by using Allen's data[12] can be simply correlated as[13] (at p = 1 atm)

$$k_1 = 0.00255 \left(\frac{T}{10^4}\right)^{4.34} \text{cm}^{-1} \quad 1130 \text{ Å} \leq \lambda \leq \infty \qquad (9)$$

$$k_2 = 1.776 \left(\frac{T}{10^4}\right)^{-0.71} \text{cm}^{-1} \quad 0 \leq \lambda \leq 1130 \text{ Å} . \qquad (10)$$

It can be seen that for a wave thickness of a few centimeters the long wavelength radiation can be considered as transparent, whereas for the VUV portion, the gas is not strictly optically thick. However, it can be shown by a simple calculation based on the exact integral expressions, that the flux calculated by the optically thick band approximation overestimates the radiative flux by at most a factor of two in the temperature range

9
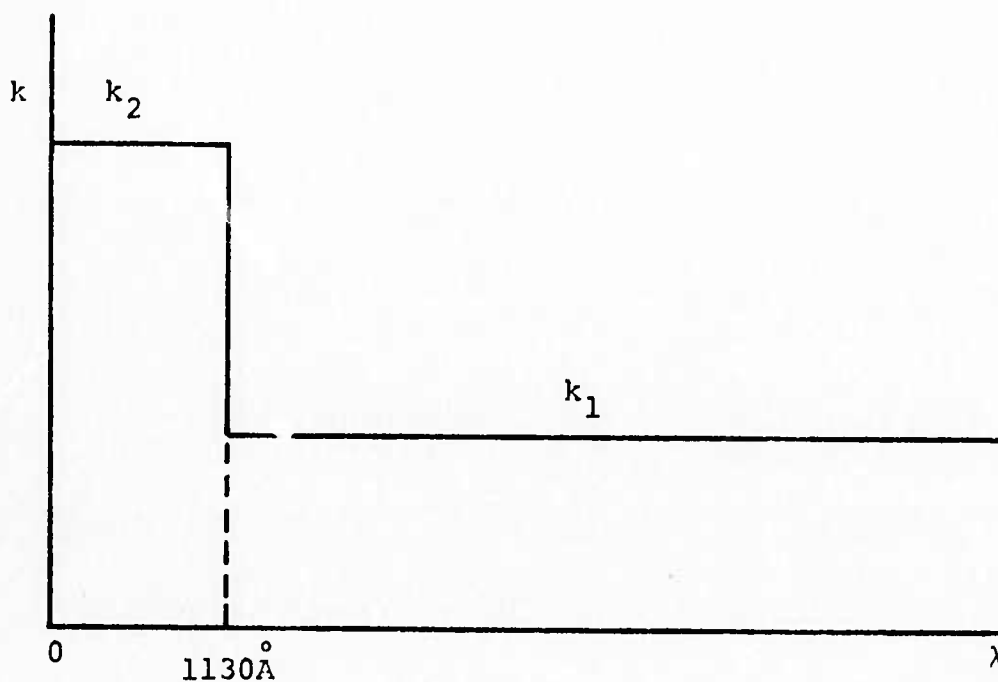
Figure 2   Schematic diagram of a two band absorption coefficient model.

10

of interest. It is our purpose in the present report to develop a simple numerical scheme in solving the LSC wave problem. Therefore, the simple optically thick band approximation is adopted in this report. Hence the radiative flux divergence in Equation (2) can be expressed as[5]

$$\frac{dF_r}{dx} = - \frac{d}{dx}\left(\lambda_r \frac{dT}{dx}\right) + j_r \quad , \tag{11}$$

where λ_r is the radiative conductivity defined as:

$$\lambda_r = \frac{4}{3k_2} \frac{dB_2}{dT}$$

$$= \frac{20}{\pi^4} \frac{\sigma T^3}{k_2} e^{-u_1}\left(u_1^4 + 4u_1^3 + 12u_1^2 + 24u_1 + 24\right) . \tag{12}$$

Also $u_1 = h\nu_1/kT$ and ν_1 corresponds to the wavelength $\lambda = 1130 \ \mathring{A}$. The term j_r represents the transparent cooling part. Since 95 percent of the blackbody energy falls within the visible and IR spectrum for the temperature range of interest, we simply approximate the cooling term as

$$j_r = 4\pi k_1 \int_0^\nu \left[B_\nu(T) - B_\nu(T_o) \ d\nu\right]$$

$$\approx 4\sigma k_1\left(T^4 - T_o^4\right) . \tag{13}$$

For the thermodynamic properties of high temperature air, it has been demonstrated by Su[14] that a simple power law correlation can retain both reality and simplicity. Under a constant pressure process (p = 1 atm), the enthalpy can be correlated as

$$h = 5.036 \times 10^{11} \left(\frac{T}{10^4}\right)^2 \ cm^2/sec^2$$

11

from Predvoditelev's[15] data (Figure 3). The thermal conductivity of high temperature air has been calculated by Hanson.[16] As one can see (Figure 4), the data are highly oscillatory because of the changes of chemical composition with temperature. However, because of the range of interest (1 eV > T > 2 eV) and simplicity, calculated λ_r (according to Equation 12) and λ_c are combined and correlated to two single exponential functions as shown in Figure 4,

$$\lambda(T) = \lambda_r + \lambda_c = 2.2 \times 10^8 \, e^{6.4(T/10^4 - 1.75)} \quad \text{erg/sec cm °K)}$$

$$T < 17500 \text{ °K}$$

$$= 2.2 \times 10^8 \, e^{3(T/10^4 - 1.75)} \quad \text{erg/sec cm °K}$$

$$T > 17500 \text{ °K} \quad . \quad (14)$$

On the other hand, in the conductive energy loss term j_r Equation (3), λ_c is simply correlated by the following formula as in Reference 17 (Figure 5):

$$\lambda_c = \frac{0.129 \times 10^7}{\left(\cosh 5\left(\frac{T}{10^4}\right) - 1.45\right)} \quad \text{erg/sec cm °K} \quad .$$

2.4   THEORY OF QUASILINEARIZATION

Because of the inherent nonlinearity of the LSC wave problem, as described above one has to resort to numerical integration of the governing differential equations. The principal difficulty in numerical analysis of this problem is the split, two-point nature of the boundary conditions. Since initial conditions are required to start the numerical integration, a guess based on physical intuition of the initial condition has to be made. In general, however, after the numerical integration, the boundary conditions on the
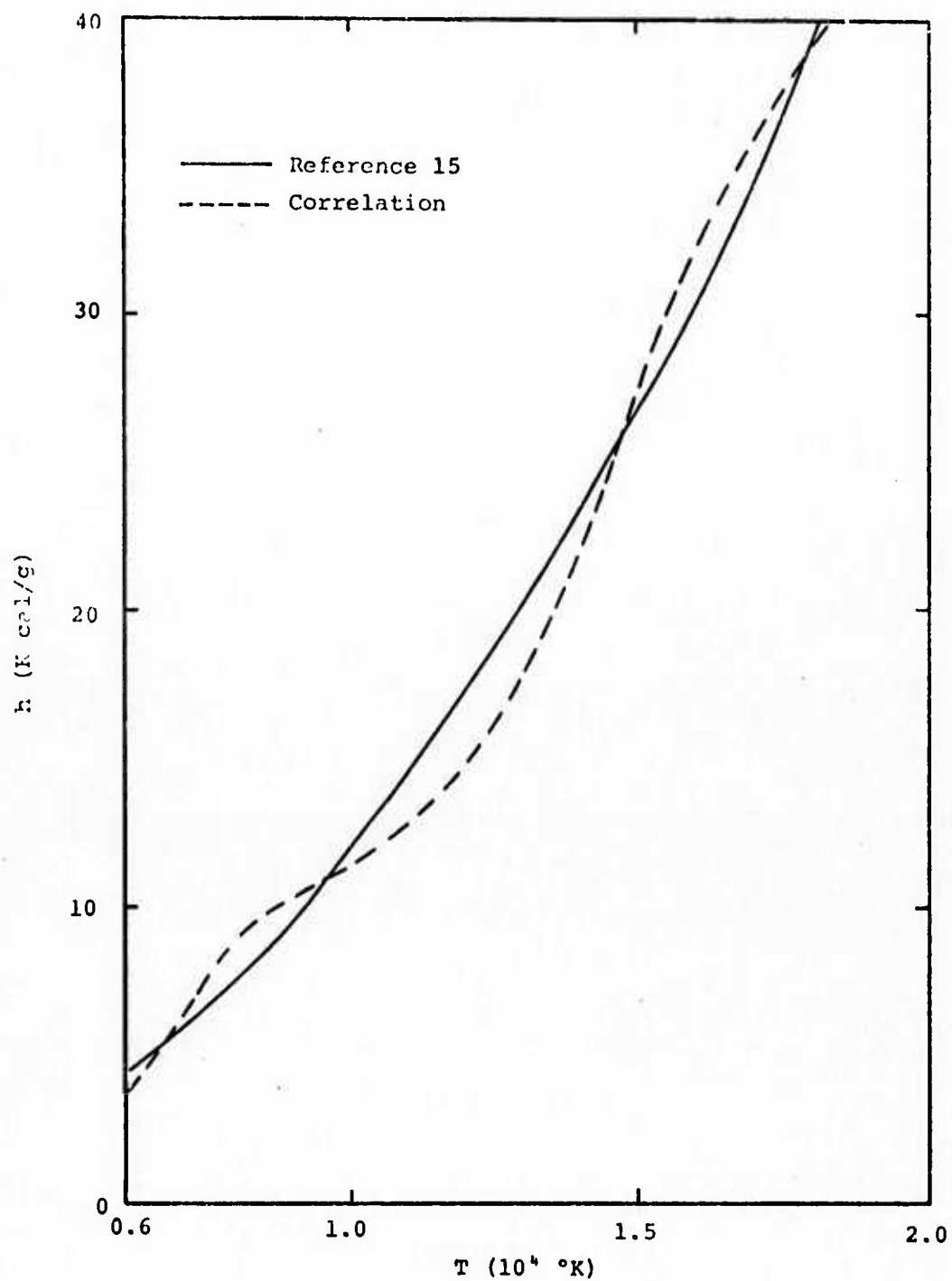
Figure 3   Correlation of enthalpy of high temperature equilib-
rium air.

13
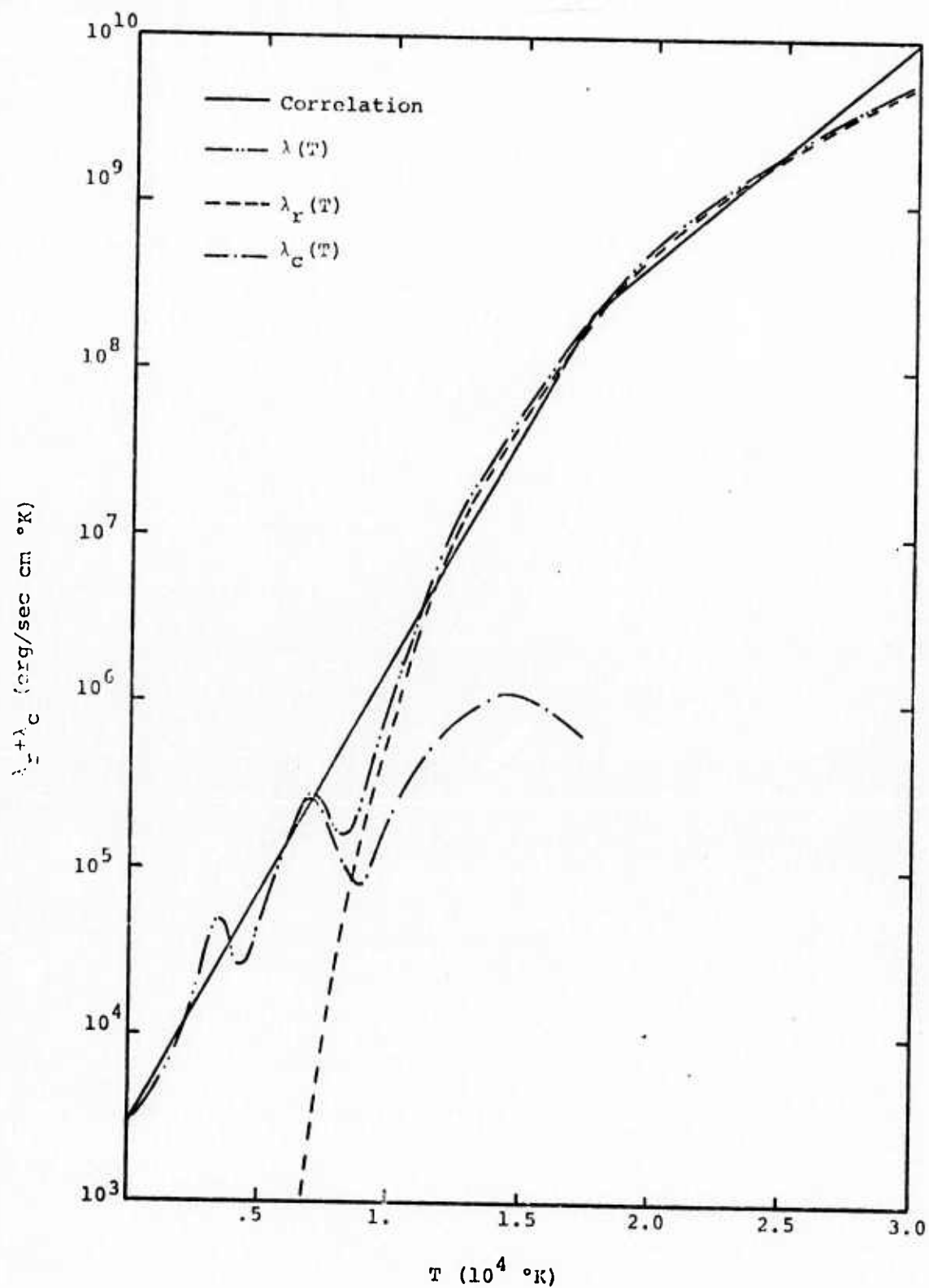
Figure 4   Correlation of $\lambda_r + \lambda_c$ of high temperature equilibrium air.

14
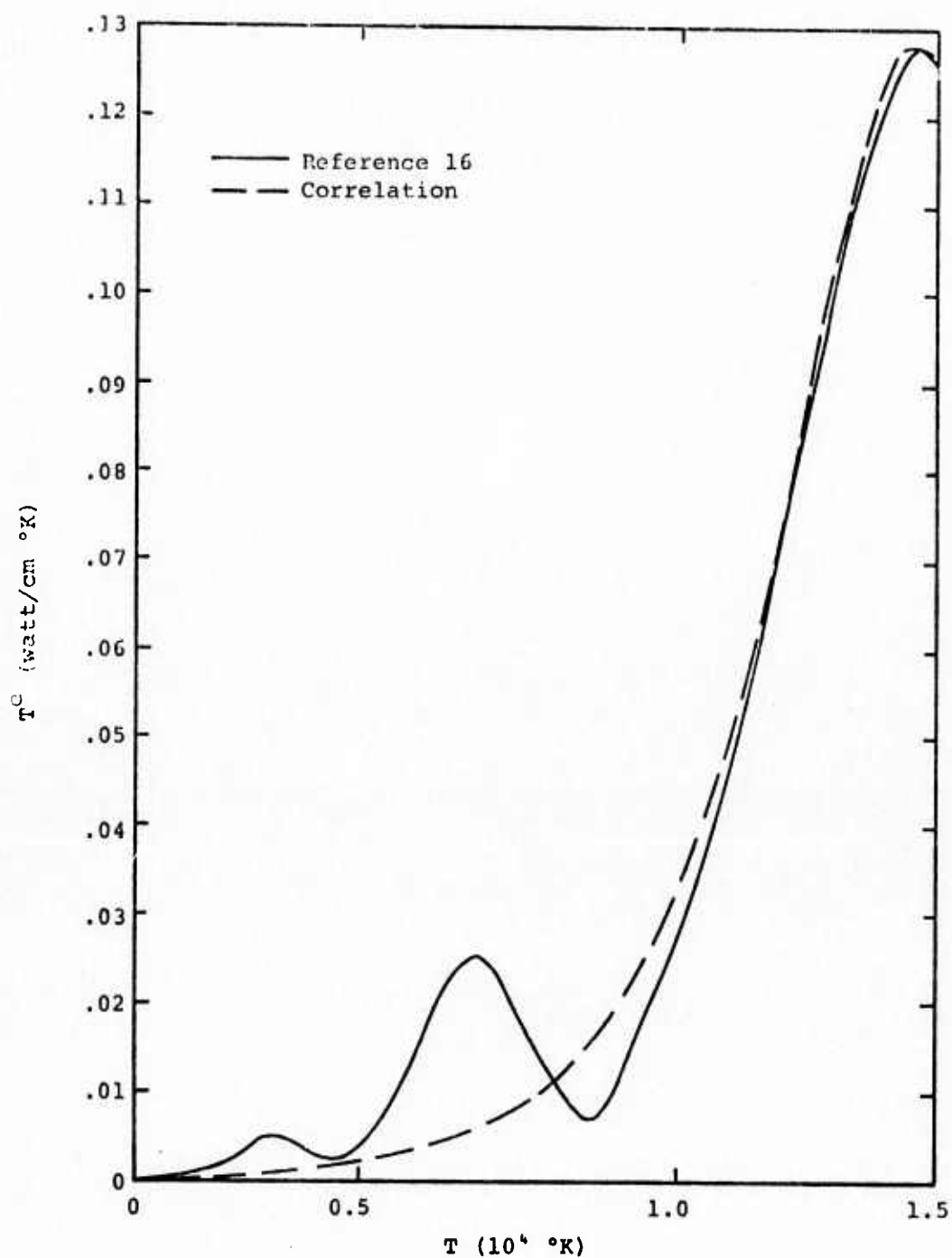
Figure 5   Correlation of thermal conductivity of high temperature equilibrium air.

end point are not satisfied. In order to satisfy the second
boundary condition, one must iterate until convergence, within
some predetermined accuracy criterion, is obtained. A common
method is to obtain additional solutions with different ini-
tial guesses, followed by inverse interpolation or extrapola-
tion on the boundary value attained at the end point. Another
method, called successive substitution, involves solving for
the highest derivative and substituting the results successive-
ly into the right hand side starting with an approximation
that satisfies the boundary conditions. Both methods require
a reasonable approximation to the boundary condition in the
first method and functions in the second method. Without a
sufficiently good initial guess, the processes may diverge or
converge very slowly. Such a technique is not, in general,
desirable.

Quasilinearization may be viewed as an extension of
Newton's method for the solution of algebraic equations to the
solution of differential equations.[7] This method has been
widely used in solving boundary layer problems[8,9,10] and
has been demonstrated to be a powerful method for handling
split point boundary conditions.

Consider a system of nonlinear first order ordinary
differential equations:

$$\frac{dy_i}{dx} = f_i(y_1, y_2 \cdots y_n) \qquad i = 1, 2 \cdots n \quad , \tag{15}$$

where y_i is the ith dependent variable, and x is the indepen-
dent variable, where some of the boundary conditions speci-
fied at x = 0,

$$y_i(0) = B_i \qquad i = 1, 2 \cdots \ell \quad , \tag{16}$$

and some are specified at the other boundary, x = a,

$$y_i(a) = B_i \qquad i = \ell+1, \cdots n \quad . \tag{17}$$

16

The $(k+1)$ approximation to the solution, $y_i^{(k+1)}$, can be obtained by expanding the right-hand side of the equation about the $k\underline{th}$ approximation and retaining only the linear terms:

$$\frac{dy_i^{k+1}}{dx} = f_i(y^k) + \sum_{j=1}^{n} \frac{\partial f_i(y^k)}{\partial y_j} \left[y_j^{k+1} - y_j^k \right]$$

$$i = 1,2,\cdots n \quad . \tag{18}$$

This equation is linear in y^{k+1}, and the system of equations can be solved by any standard numerical integration routine. Also, since it is a linear equation, the principal of superposition can be applied.

A particular solution, $P_i(x)$, may be obtained by integrating the entire equation, starting with the initial conditions:

$$Y_i(0) = P_i(0) = 0 \qquad i = 1,2,\cdots n \quad . \tag{19}$$

Then one homogeneous solution is obtained for each of the n boundary conditions with the initial conditions:

$$Y_i(0) = H_{ij}(0) = \delta_{ij} \qquad i,j = 1,2,\cdots n \tag{20}$$

where δ_{ij} is the Kronecker delta, $\delta_{ij} = 1$ when $i = j$ and $\delta_{ij} = 0$ when $i \neq j$. The requirement that the sums of the particular and homogeneous solutions satisfy the boundary conditions determines the combination constant C_j:

$$\sum_{j=1}^{n} C_j H_{ij}(b_i) = B_i - P_i(b_i) \qquad i = 1,2,\cdots n \quad , \tag{21}$$

where $b_i = 0$ for $i = 1,2,\cdots \ell$, and $b_i = a$ for $i = \ell+1\cdots n$.

17

The new approximation, y^{k+1}, is then calculated at each point by summing the stored values of P and H

$$y_i^{k+1}(x) = P_i(x) + \sum_{j=1}^{n} C_j H_{ij}(x) \quad , \tag{22}$$

or by obtaining the initial conditions in this way and integrating forward.

Notice that if the particular solution, P, is required to satisfy the ℓ known initial conditions, then there are only $(n-\ell)$ remaining boundary conditions to satisfy, or there are only $(n-\ell)$ homogeneous equations to solve, which drastically reduces the integration time.

Combining Equations (1), (2) and (11) gives a second order nonlinear equation governing the propagation and structue of the LSC wave.

$$\frac{d}{dx}\left[\left(\lambda_c + \lambda_r\right)\frac{dT}{dx}\right] - \rho_o v_o \frac{dh}{dx} + k_L \phi - j_c - j_r = 0 \quad . \tag{22a}$$

Here λ_c, λ_r, h, $k_L \phi$, j_e and j_r are all complicated, non-linear functions of T. Defining $\lambda = \lambda_c + \lambda_r$ and $j = j_c + j_r$, it is shown in Appendix A that Equation (22a) can be rewritten as

$$\frac{d^2 T^{k+1}}{dx^2} - p^k \frac{dT^{j+1}}{dx} - r^k T^{k+1} + s^k = 0 \tag{23}$$

for $-\infty < x < +\infty$, where

$$s^k = p^k \frac{dT^k}{dx} + r^k T^k - H^k \quad . \tag{24}$$

Details of the method of solution and it's associated difficulties appear in Appendix A. The interested reader should refer to that section of the report for further discussion of the implementation of the method of quasilinearization and its intricacies.

18

2.5 RESULTS AND DISCUSSION

Before we discuss the results of nonlinear calculations, let us briefly describe some of the linear results from References 6 and 17 which will be used for comparison. For a linear model, Equation (2) can be simplified as

$$\frac{d^2T}{dx^2} - \frac{\rho_o v_o C_p}{\lambda} \frac{dT}{dx} - \frac{G}{\lambda} T = 0 \quad \text{for} \quad T < T_{in}$$
$$x < 0 \quad , \quad (25)$$

with boundary conditions

$$\frac{dT}{dx} = 0 \quad \text{at} \quad x = \pm\infty$$
and
$$T = 0 \quad \text{at} \quad x = -\infty$$

All the coefficients in Equation (25) are constants. Comparing Equation (25) with Equation (22a), one recognizes that $C_p T$ is equivalent to $k(T)$ and GT is equivalent to $j_c(T) + j_r(T)$. Since Equation (25) is a linear equation, it can be solved analytically to give

$$v_o = \frac{\lambda_c}{\rho_o C_p} \sqrt{\frac{k_L \phi_o}{\lambda_c T_{in}}} \sqrt{1 + \frac{\lambda_r}{\lambda_c} \left[\left(1 - \frac{2GT_{in}}{k_L \phi_o}\right)\left(1 - \frac{GT_{in}}{k_L \phi_o}\right)^{-1/2}\right]} \, ,$$
$$(26)$$

where T_{in} is the ignition temperature at $x = 0$ (usually $T_{in} = 12,000$ °K). The temperature profile is given by the equations

$$T = T_{in} e^{-\alpha_1 |x|} \qquad x < 0$$
$$(27)$$
$$T = T_{in} e^{\alpha_2 x} + \frac{k_L \phi_o/\lambda}{\alpha_1 \alpha_2} \left(e^{\alpha_2 x} - 1\right) \quad x > 0 \ ,$$

where

$$\left\{ \begin{array}{c} \alpha_1 \\ \\ \alpha_2 \end{array} \right\} = \frac{\rho_o v_o C_p}{2\lambda} \pm \sqrt{\left(\frac{\rho_o v_o C_p}{2\lambda}\right)^2 + \frac{G}{\lambda}} \quad .$$

Again, to present some of the nonlinear calculations, we perform calculations for the experiment of Bunkin, et al.[1] They indicate that for an experiment utilizing Nd laser-irradiated air, the temperature (T_∞) in the downstream portion of the wave is estimated around 18,000 °K for p = 1 atm. The laser power was 1,100 kw incident onto a 0.25 cm spot which yields a flux of $\phi_o = 2.25 \times 10^7$ watts/cm^2. The measured laser absorption coefficient is about 7×10^{-3} cm^{-1}. Therefore in the downstream portion of the wave, the absorbed radiative energy can be approximated as $k_L \phi \approx 1.57 \times 10^5$ watts/cm^3, where in the upstream, practically no energy is absorbed (or $k_L \approx 0$). Using averaged values of λ, C_p and G, the energy losses through radiation and conduction account for 21.6% of the total energy absorbed. With these losses the velocity predicted by the linear theory is about 9.36 m/sec.[6] The temperature profile is then calculated from Eq. (27) and plotted in Figure 6. The wave front thickness is greater than 10 cm and the temperature reaches 54,000 °K (this can be seen simply by letting dT/dx = 0, and then $T_\infty = k_L \phi_o/G$). Now let us examine the nonlinear effects on the LSC wave by gradually replacing the linear coefficients in Eq. (25) with the corresponding nonlinear terms. By introducing the real equation of state (curve B in Figure 6), the wave front spreads even more (final temperature reaches 54,000 °K at a distance of about 35cm downstream), due to the fact that most of the energy absorbed in the wave front is used to ionize the gas first
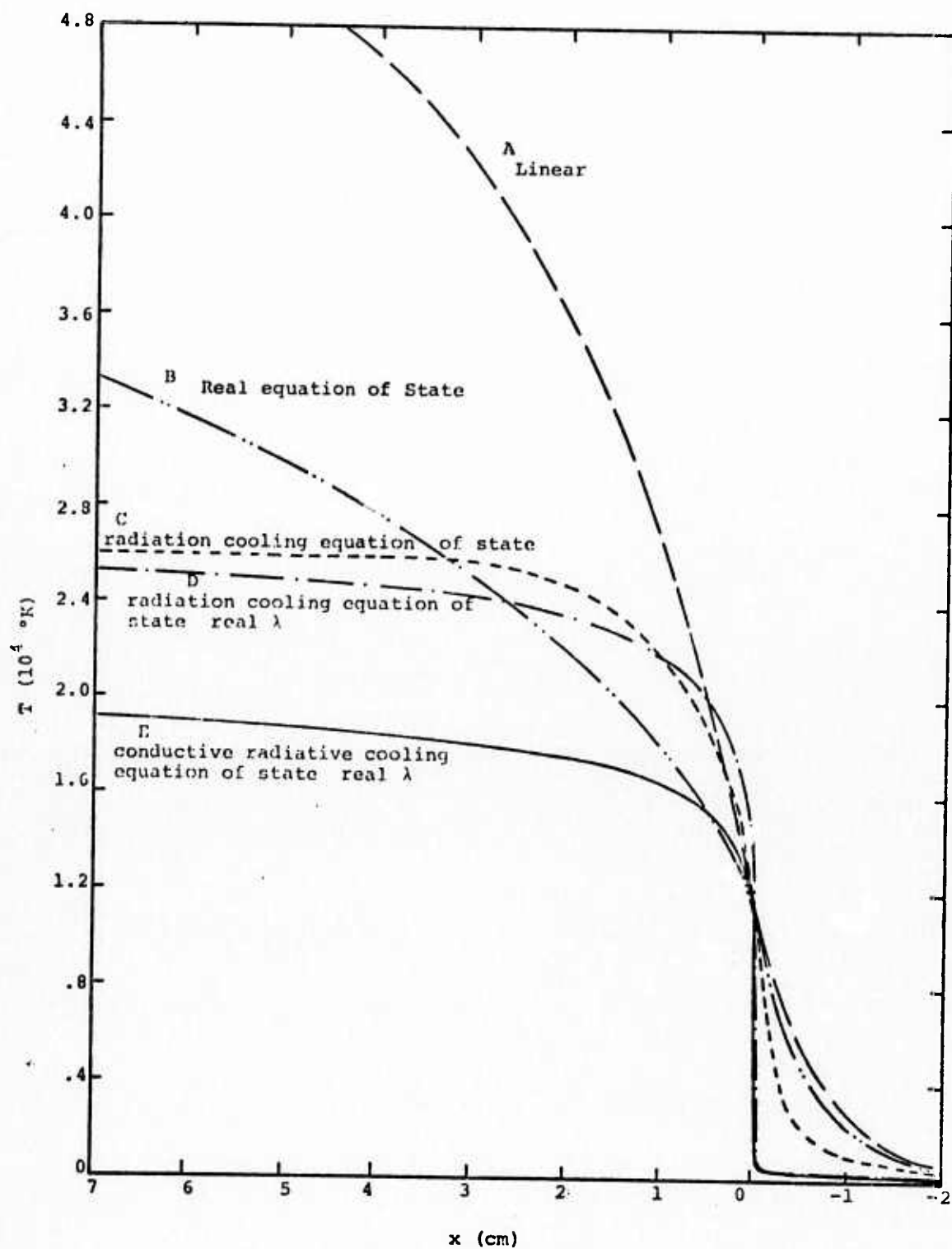
20

Figure 6   Nonlinear effects of various terms in Equation 22a.

21

instead of increasing the temperature linearly as in the ideal gas law. Next, the radiative energy loss in the linear equation is replaced by the real loss; Eq. (13). This has a tremendous influence on the temperature profile (curve C in Figure 6) since the real radiative loss term is proportionate to T^4 rather than T. This effect reduces the downstream temperature from 54,000 °K to about 26,000 °K, and at the same time the wave front thickness is reduced to 4 cm. The temperature profile steepens even more as the nonlinear diffusivity $[\lambda = \lambda_c(T) + \lambda_r(T)]$ is introduced (curve D in Figure 6). It can be seen that a definite wave front is formed within about 2 cm. Finally, with the nonlinear conductive loss included (curve E in Figure 6), the downstream temperature drops even further, to a reasonable range $T_\infty \approx 19,400$ °K. From the above discussion, it is clear that the nonlinear radiative and conductive diffusivity establish the shape of the wave front whereas the radiative and conductive loss mechanisms determine the final temperature profile behind the wave. The wave speed predicted by the above cases varies from 4.0 m/sec (case E) to 13.2 m/sec (case D). We will discuss more about the wave velocity in the next few paragraphs.

Figures 7 and 8 compare the energy balance for the following three cases a) $k_L\phi_o = 2.5\times10^5$ watts/cm^3 and R = 0.125 cm [where R is the radius of the spot, Eq. (14)], b) $k_L\phi_o = 1.57\times10^5$ watts/cm^3 and R = 0.125 cm and c) $k_L\phi_o = 1.57\times10^5$ watts/cm^3 and R = 0.25 cm. We plot the temperature profiles of the above three cases in Figure 7. The wave fronts are almost exactly the same whereas the downstream temperatures in the three cases are different. With high absorbed energy, Case A shows a higher temperature than Case B. However, with the different spot size, the temperature of the LSC wave with lower energy addition (Curve C) can be higher than the temperature profile with larger energy
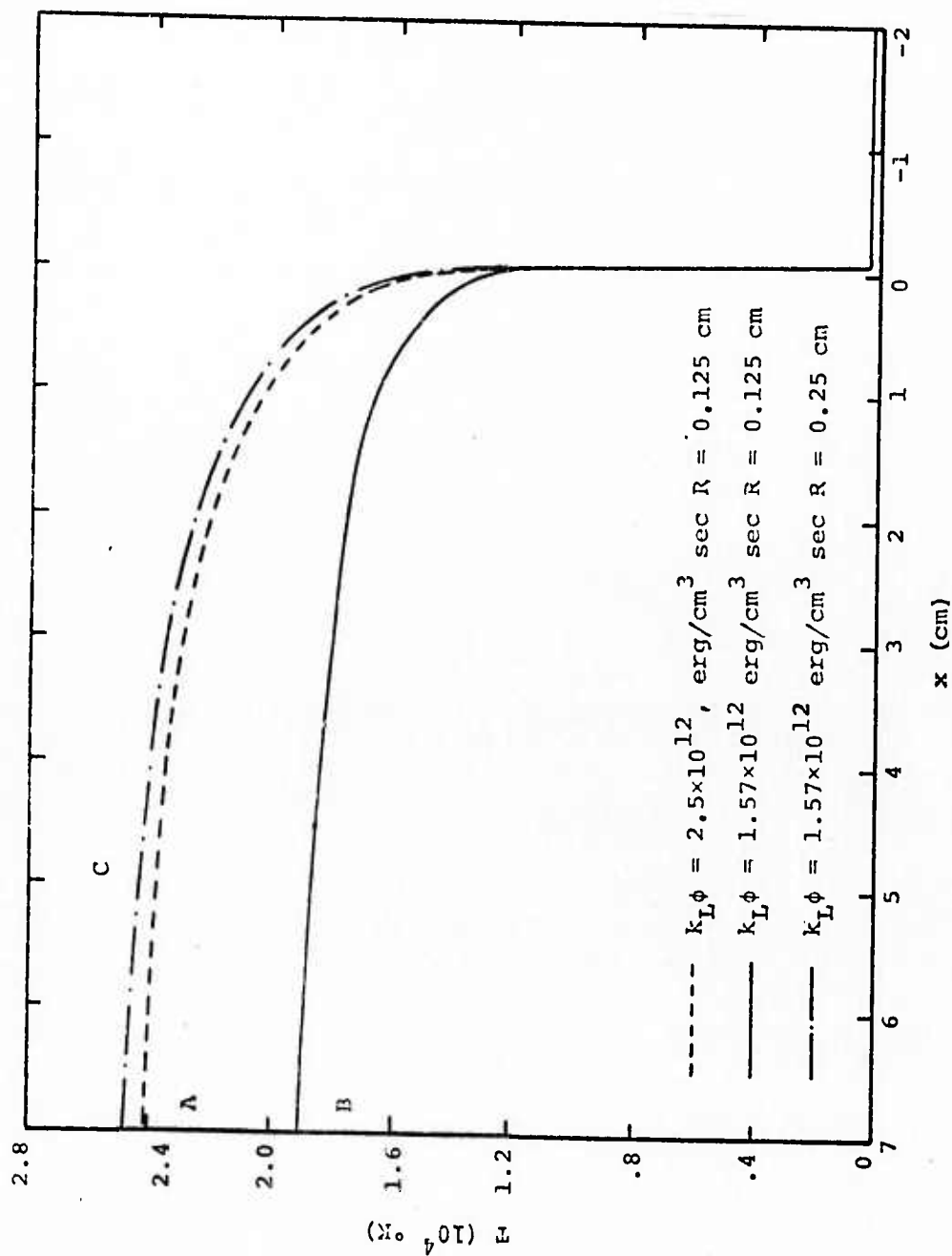
Figure 7   Temperature profiles of three different cases.   (A) $k_2\phi$ = 2.5 x 10^5 watts/cm^3 and R = 0.125 cm; (B) $k_2\phi$ = 1.57 x 10^5 watts/cm^3 and R = 0.125 cm; and (C) $k_2\phi$ = 1.57 x 10^5 watts/cm^3 and R = 0.25 cm.

23
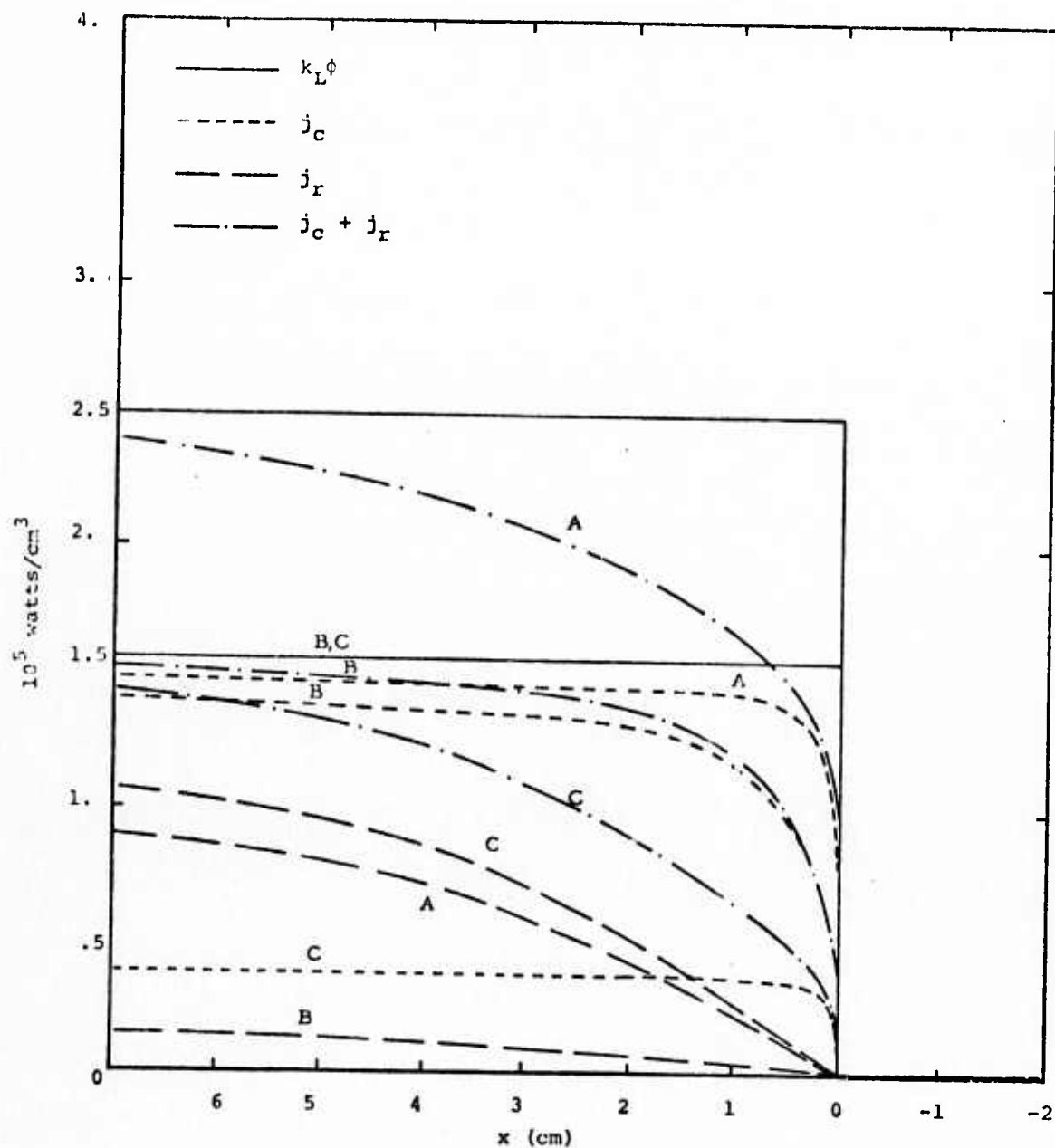
Figure 8   Energy balance for three different cases. (A) $k_2\phi =$
2.5 x 10^5 watts/cm^3 and R = 0.125 cm. (B) $k_2\phi =$
1.57 x 10^5 watts/cm^3 and R = 0.125 cm and (C)
$k_2\phi$ = 1.57 x 10^5 watts/cm^3 and R = 0.25 cm.

addition (Curve A). It is not surprising, since the conductive energy is inversely proportional to the spot size, i.e., $j_r \propto 1/R^2$. Therefore in Case C the conductive loss is only about one fourth of the loss in Case A. Figure 8 shows the comparison of absorbed energy, radiative loss term and conductive loss term for all three cases. For Cases A and B the conductive losses are comparable while the radiative losses show a tremendous difference. This effect is in part due to the smaller thermal conductivity at higher temperature (see Figure 4) and the strong temperature dependence of the radiative energy loss. The absorbed energy in Cases B and C are the same, however, Case B is dominated by conduction loss and radiative loss dominates for Case C. It is interesting to notice that the area of $k_L \phi_0 - j_r - j_c$ of Case A and C are about the same. This is the reason why the temperature profile are about the same for Case A and C shown in Figure 7, even though their dominant loss mechanism is different. Since the wave velocity depends upon the amount of energy transported from downstream to upstream, we expect that the wave speeds for Case A and C will be similar. In fact, we obtain $v_0 = 10.2$ m/sec for Case C and $v_0 = 9.8$ m/sec for Case A. Notice that the slope of Curve C in Figure 7 is slightly greater than the slope of A therefore the wave speed of C is also slightly higher despite the larger absorbed energy in Case A. Curve C has a much slower velocity; $v_0 \simeq 4$ m/sec due to smaller gradient at the wave front.

Figure 9 summarizes our calculations for the wave velocity as a function of absorbed energy with various beam radii. As R decreases, conductive energy loss through the radial direction increases. When j_r becomes the dominant loss mechanism the wave velocity decreases drastically with decreasing radius. This effect can be seen more clearly in
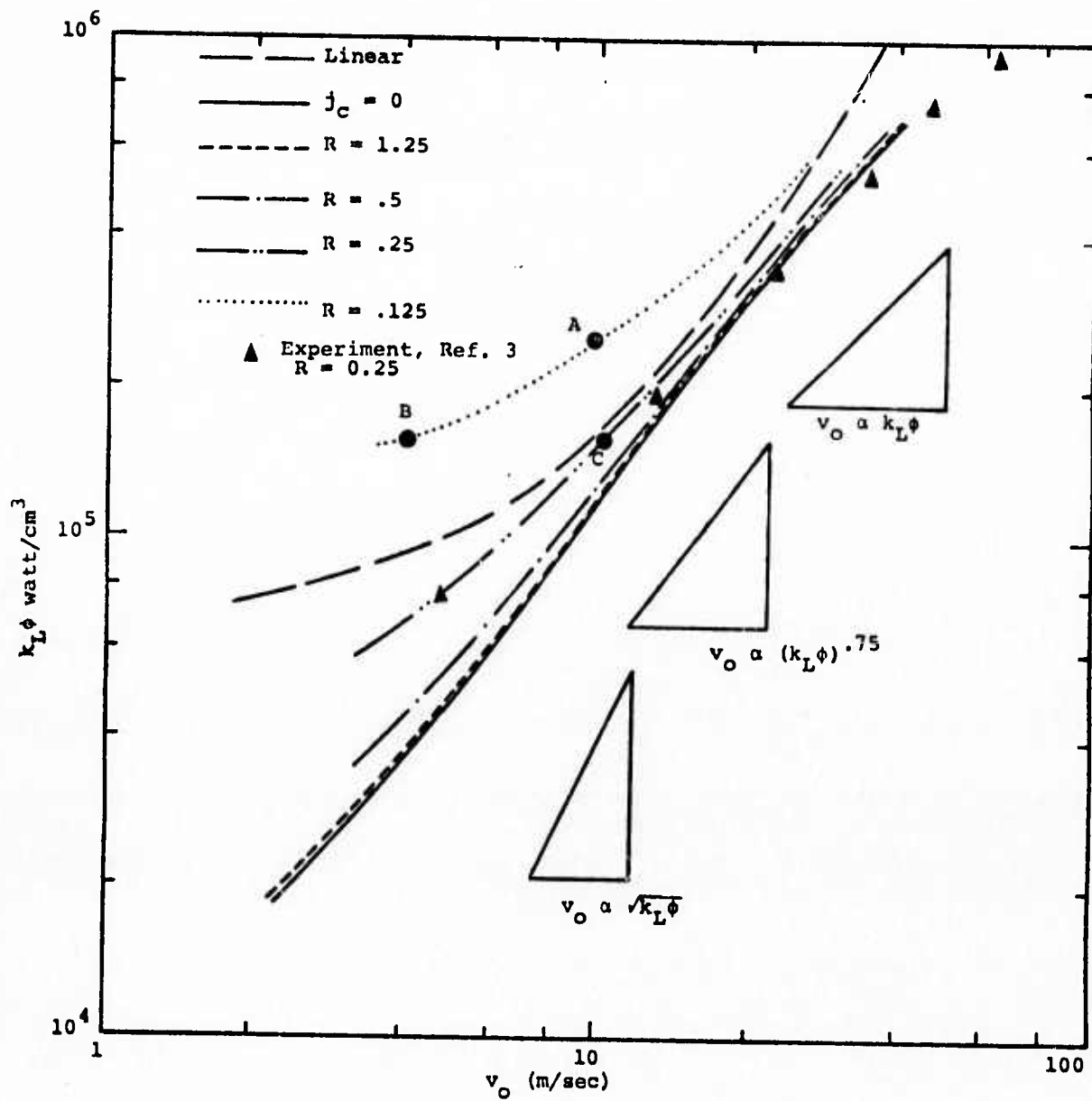
Figure 9   LSC propagation velocity as a function of absorbed energy rate at various laser beam radii.

26

Figure 10 where wave speed is plotted as a function of radius
with various absorbed energy levels as a parameter. When the
spot size is larger than one centimeter (or R > 0.5 cm) the
beam radius has little effect on the wave propagation speed.
In fact, for all practical purposes, the velocity can be pre-
dicted without including the conductive energy loss for
R > 0.5 cm in most cases (except at very low $k_L \phi_o$). The rea-
son for neglecting j_R for R > 0.5 cm is obviously shown in
Figure 8, Case C where the radiative energy loss term dominates
the conductive energy loss even at R = 0.25. In the range
for R < 0.5, in general the velocity varies from linear to
square term of radius (Figure 10). It is also interesting to
note that for most of the cases, the wave speed is neither in
the linear regime ($v_o \propto k_L \phi_o$), nor square root regime
($v_o \propto \sqrt{k_L \phi_o}$), but is proportional to $(k_L \phi_o)^{.75}$.

For comparison, the prediction of wave speed from a
linear model is also plotted in Figure 9. It is shown that
the wave speed has a square root dependence on $k_L \phi_o$ if $k_L \phi_o$
is large, and a linear dependence close to the threshold as
previously discussed. Judging from the simplicity of the
linear theory, the prediction of wave speed has a reasonable
agreement in comparison with the nonlinear theory, except
for the cases where R is very small. However, as we pointed
out before, [5] a correct value of R is not very well defined
in a focused laser beam. Conductive loss calculated in
Eq. (3) is strictly applied only to cylindrical-like plasma.
Therefore, for a simple estimate of wave propagation velocity
it is our opinion that either a phenomenological analysis or
a linear model is sufficient.

So far we have not included in our analysis the non-
linear variation of absorption coefficient, and have treated
the cases where absorbed flux can be approximated as $k_L \phi_o$.
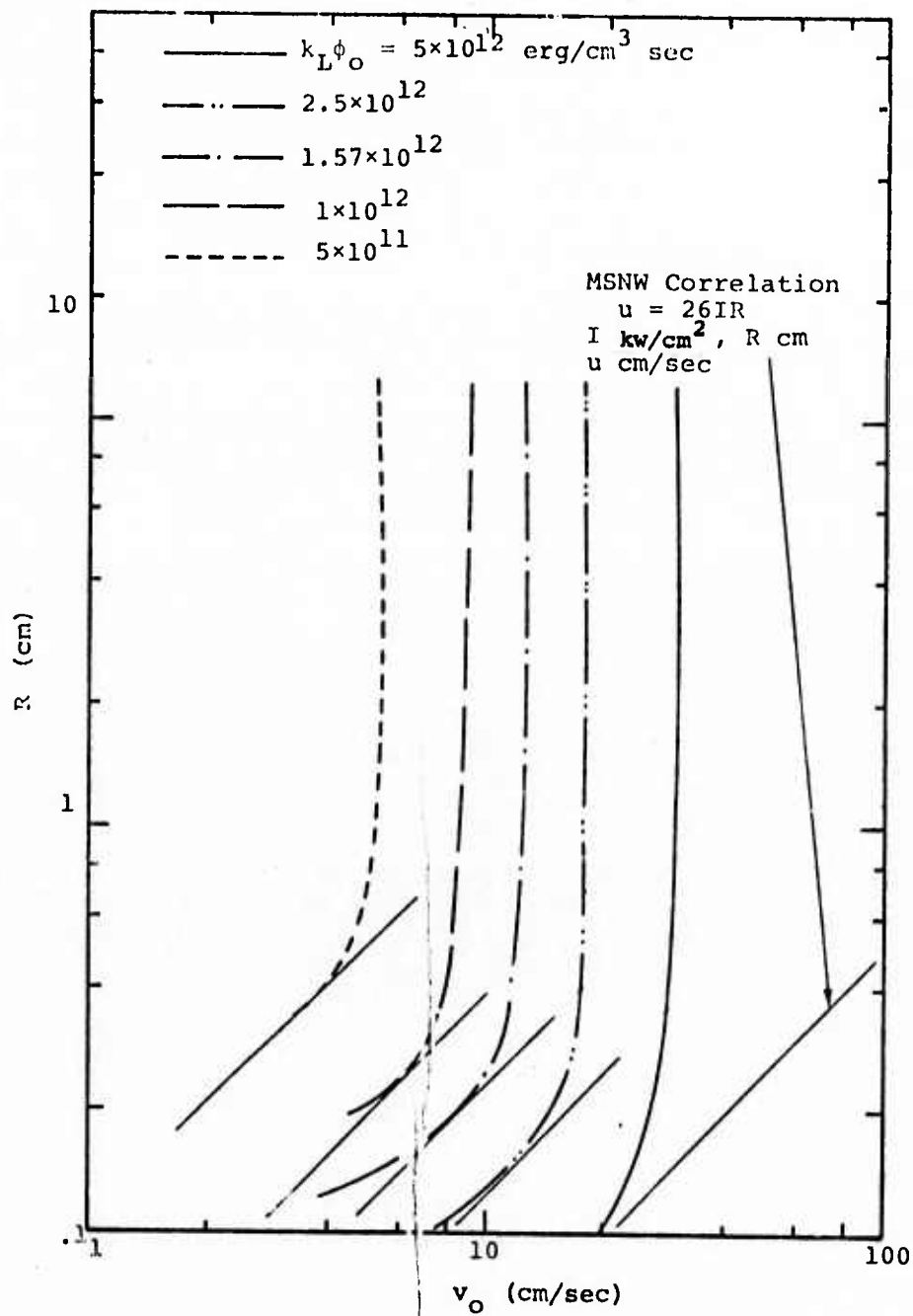
Figure 10   LSC propagation velocity as a function of radius at various absorbed rates.

28

It is unfortunate that we have found that there exists a strong singularity downstream if the flux at any point is treated as

$$\phi(x) = \phi_o e^{-\int_{-\infty}^{x} k(T)dx} \quad .$$

As the LSC wave propagates the incident flux is absorbed by the wave front, and therefore attenuated by the hot plasma. When most of the incoming energy is absorbed, the temperature at the far downstream is expected to decrease as shown in Figure 1. Hence there is a maximum temperature existing in the downstream. At that maximum temperature the gradient of the temperature profile is zero; $dT/dx|_{x_m} = 0$. Then the derivative of ϕ with respect to T (where T is treated as an independent variable in the method of quasilinearization) is singular at s_m; i.e.,

$$\frac{d}{dT}\bigg|_{x_m} = \frac{d}{dx}\frac{dx}{dT}\bigg|_{x_m}$$

Hence the method of quasilinearization fails to apply in the region around x_m.

Although the nonlinear absorption effect has not been included, we feel that we have already demonstrated the importance of energy loss mechanisms and the diffusive effects in predicting the temperature profile and wave velocity of a LSC wave. We feel that the parameter $k_L\phi_o$ (or the total absorbed flux) is a useful parameter in interpreting any experimental data. For example the data of LSC experiments performed by Klosterman, et al.,[3] using a CO_2 laser incident on an Aℓ target in air has been plotted on Figure 9 with an estimated absorption coefficient of order unity. It shows

29

very good agreement with the non-linear theory, especially the dependence on the absorbed flux.

In conclusion, we have used the method of quasilinearization to study nonlinear effects of a propagating LSC wave. It is found that nonlinear effects are very important in predicting the temperature profile and has less effect in calculating the wave velocity. However, for any spot size which is smaller than .5 cm, the conductive heat loss through radial direction dominates the temperature profile and thereby affects the wave speed. It is found that at higher absorbed flux level $k_L\phi_o > 1\times10^5$ watts/cm^3 and large beam diameter (R > 0.5 cm) a simplified linear theory or phenomenological analysis can be used in predicting the wave velocity.

3. A NUMERICAL STUDY OF SOME POTENTIAL TWO-DIMENSIONAL AND TARGET-INDUCED HYDRODYNAMIC EFFECTS ON LSC WAVE PROPAGATION

3.1 INTRODUCTION

In Section 2, and in our previous studies, we have presented a theoretical formulation which seems to adequately reproduce the experimentally observed features of LSC wave propagation. In particular, it is shown in Figure 9, that our model, which includes radiative pre-heating as the primary transport mechanism of the wave predicts both the magnitude and scaling of LSC velocity with absorbed flux reasonably accurately. Furthermore, we show in Figure 10, that the variation of wave velocity with beam radius can be approximated as nearly linear for a small range of beam radii near the LSC threshold as found by JSNW. [3b] We also indicate lower theoretical predictions for the LSC velocity than experiment at the larger beam diameters. Since the experimental data are sparse and the beam radius variation is not great, the transition to independence of v_O on beam radius has not yet been verified experimentally. As has been stated, this model embodies three principal simplifying assumptions. They are (1) the model is one dimensional, (2) the deflagration approximation is used, i.e., the wave is in pressure balance with the atmosphere at $p = 1$ atm, and (3) the wave is far from the target so that wave interactions with the solid boundary imposed by the target are negligible.

In spite of the previously mentioned reproduction of the experimental observations by our model, there are certain features of the experimental observations which are not predicted. As has been pointed out by Klosterman and Byron, [3]

31

a simplified one-dimensional theory produces results for the wave propagation velocity which are less than the experimental measurements. Including all of the non-linear effects and associated loss mechanisms, however, we find the theoretical predictions of velocity to be in reasonable agreement with the experimental observations, c.f., Figure 9. Since a 1-D theory should place an upper bound on the LSC velocity, Klosterman and Byron argue that 2-D effects must be responsible for their observed discrepancy. The small discrepancy in itself is little reason for concern, but as has been shown,[3] the discrepancy becomes larger as the laser beam diameter is increased - in apparent disagreement with physical intuition. Indeed, holographic records obtained in the excellent study by MSNW indicate that the wave front is anything but planar, and 1-D, and that the LSC wave does expand radially beyond the diameter irradiated by the laser beam. Thus, a more detailed investigation into the 2-D effects on LSC wave propagation is in order. Also, certain other features, such as target effects have not yet been studied.

In summary, 2-D effects can be produced by the following mechanisms:

1. A focused laser beam geometry, wherein the LSC wave propagates from regions of higher laser fluence into regions of lower laser fluence.

2. Due to non-perfect attainment of pressure balance with the atmosphere, on the time scale of the interaction, regions of higher than atmospheric pressure can exist in the heated plasma. Hence, the plasma can expand radially, thus reducing the mass of gas heated by the laser beam.

3. The incident laser pulse is not necessarily spatially uniform as a function of radius. Typically the beam is Gaussian, or near-Gaussian. Thus, the central portions of the wave are subject to greater heating than the

periphery, resulting in radial gradients in
the thermodynamic and kinematic variables.

It is not clear to us, however, that these are the only
effects which may result in inadequacies of the 1-D theories
to reproduce all details of the experimental observations.
One additional feature of the model which warrants further
investigation is that associated with the target-free propa-
gation assumption. Thus, two additional complications nay
arise. They are:

4. As the ambient gas is entrained by the LSC
   wave, it is accelerated sharply. Near a
   solid surface, the heated gas is accelerated
   into the surface, stagnating at the center-
   line and then flowing radially out across
   the surface. This in itself, is a 2-D ef-
   fect. However, a 1-D effect results as well.
   It is

5. A compression wave which propagates back onto
   the target surface is reflected by the surface
   (since zero axial velocity must obtain at the
   wall) and propagates back toward the propa-
   gating LSC. Hence, an LSC which lies within
   a round trip acoustic transit time from the
   target is subject to acceleration by the re-
   flected wave. This wave can propagate at a
   steady velocity and thus appears independent
   of the target, however, the velocity of such
   a wave can be as much as an order of magnitude
   higher than the free-space LSC wave subject to
   the same laser flux.

While a detailed study of each of these effects is re-
quired before firm conclusions regarding their relative and
absolute importance can be reached, we have not carried out
such an exhaustive study here. A full 2-D treatment is re-
quired. Instead, we have chosen to investigate a subset of
these effects from which pertinent conclusions can be reached
by use of a quasi- one-dimensional code; i.e., 1-D, but with
variable laser beam area. Hence, we address in the following

sections, items (1), (2) and (5). Our effort is directed to an understanding of the propagation of LSC waves and not on the ignition per se. Hence, in our numerical calculations as discussed in Section 3.2, we assume that a partially ionized plasma which has been produced by energy transport from the heated target exists in front of the target. The results of our calculations, which are presented in Section 3.2 and 3.3 are based on modification of a one-dimensional, variable area code, HELVA, developed previously by Chapman at S^3.[20] Our modifications to this code for the present study are detailed in Section 3.4.

3.2   TECHNICAL DISCUSSION AND RESULTS

Calculations were performed on a laser supported combustion wave propagating down a cylinder or conoidal frustrum. The shape of these geometrical volumes is determined by the characteristics of the assumed focusing system of the laser. The initial conditions for such a system are shown in Figure 11. Here, we have the laser shining from the right onto the ambient gas. It passes, virtually unattenuated, through the cold zone, and is absorbed in the transition and hot zones. The hot zone is initially set to some appropriately high temperature (e.g., 15,000 °K) and the temperature is allowed to decline linearly through the transition zone to the ambient temperature of 300 °K. The length of the transition zone (typically, one centimeter) and the initial temperature of the hot zone was not found to be very critical in the final results obtained.

One of the critical parameters of the calculation is the initial size of the hot plasma, e.g., the ignition mechanism. The reason for this sensitivity is due to the complicated gasdynamical wave interactions which will now be discussed.
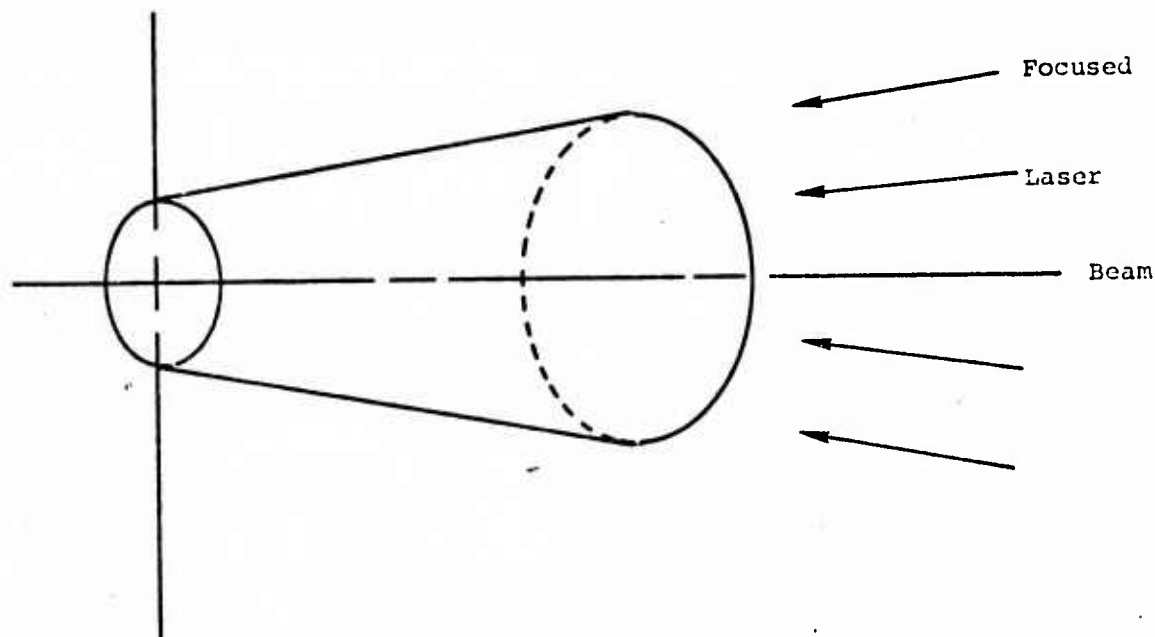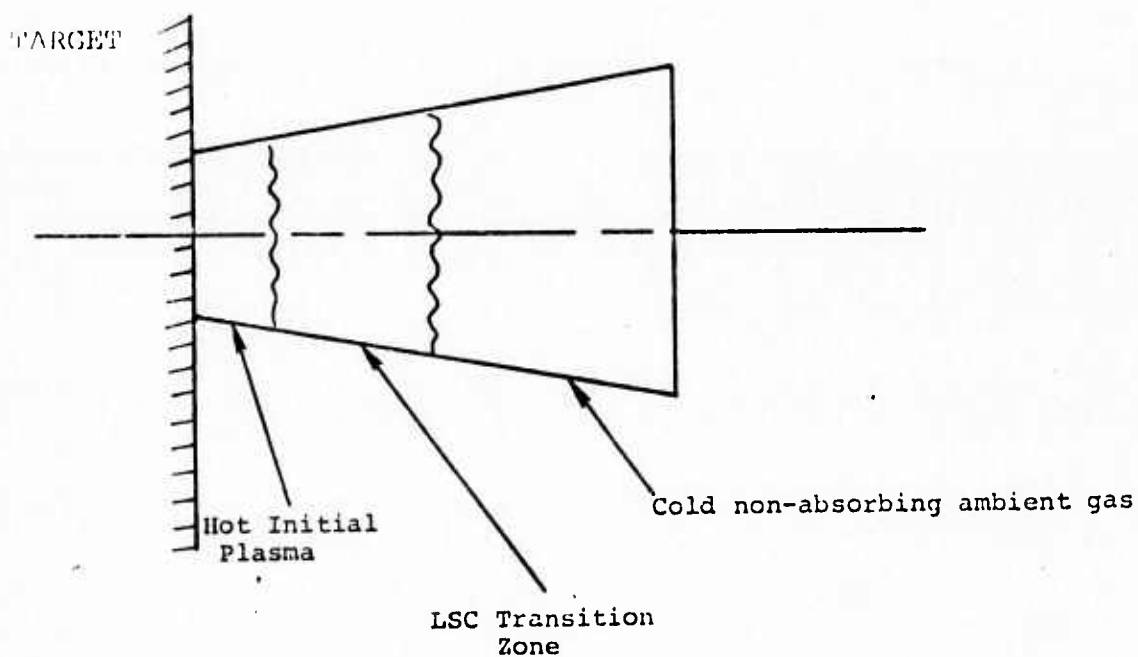
Plan View

Figure 11. Geometry for variable-area LSC wave propagation
calculation.

35

We illustrate the evolution and propagation from an initially hot plasma of length 1 cm in Figure 12(a)-(d). Here, the laser is incident at a flux of 3×10^5 watts/cm^2 onto a focal spot of 0.25 cm radius. The laser is assumed to be unfocused here, i.e., the incident rays are parallel. As the laser is turned on, the plasma begins to expand by hydrodynamic processes and the LSC wave front begins to form by radiation transport into the cold gas ahead. The radiation front (or inverse bleaching wave) compresses and accelerates the gas ahead of it. The acceleration leads to the formation of a gasdynamic shock. Hence, there exists two transition regions in the flow field - the gasdynamic precursor shock and the LSC which serves as a "leaky piston" and supports the shock wave. Simultaneously with the formation of the LSC front and the precursor shock wave, a shock is formed at the front surface of the plasma which propagates back toward the target surface. This shock is formed as a result of the momentum imparted to the plasma surface by the gas which expands away from its surface due to the deposition of laser radiation and subsequent acceleration away from the target by the precursor shock. Since the flow velocity behind the LSC front is directed towards the target, the shock easily propagates back and reflects from the target surface. The shock then propagates back through the plasma, but cannot overtake the LSC or precursor shock due to the high flow velocity of the plasma towards the target. However, the existence of the trailing shock serves to "tell the flow ahead" of the presence of the wall. This can be seen in Figure 12(d), where the LSC velocity increases sharply at about the time the secondary shock reflects from the target surface. Two important conclusions are apparent from Figure 12(d); (1) the reflected shock communicates the presence of a target (reflecting surface) to the LSC wave which propagates at a higher velocity than if the surface were absent, and (2) the precursor shock propagates at constant velocity with the energy required to support such propagation supplied by the piston (LSC)
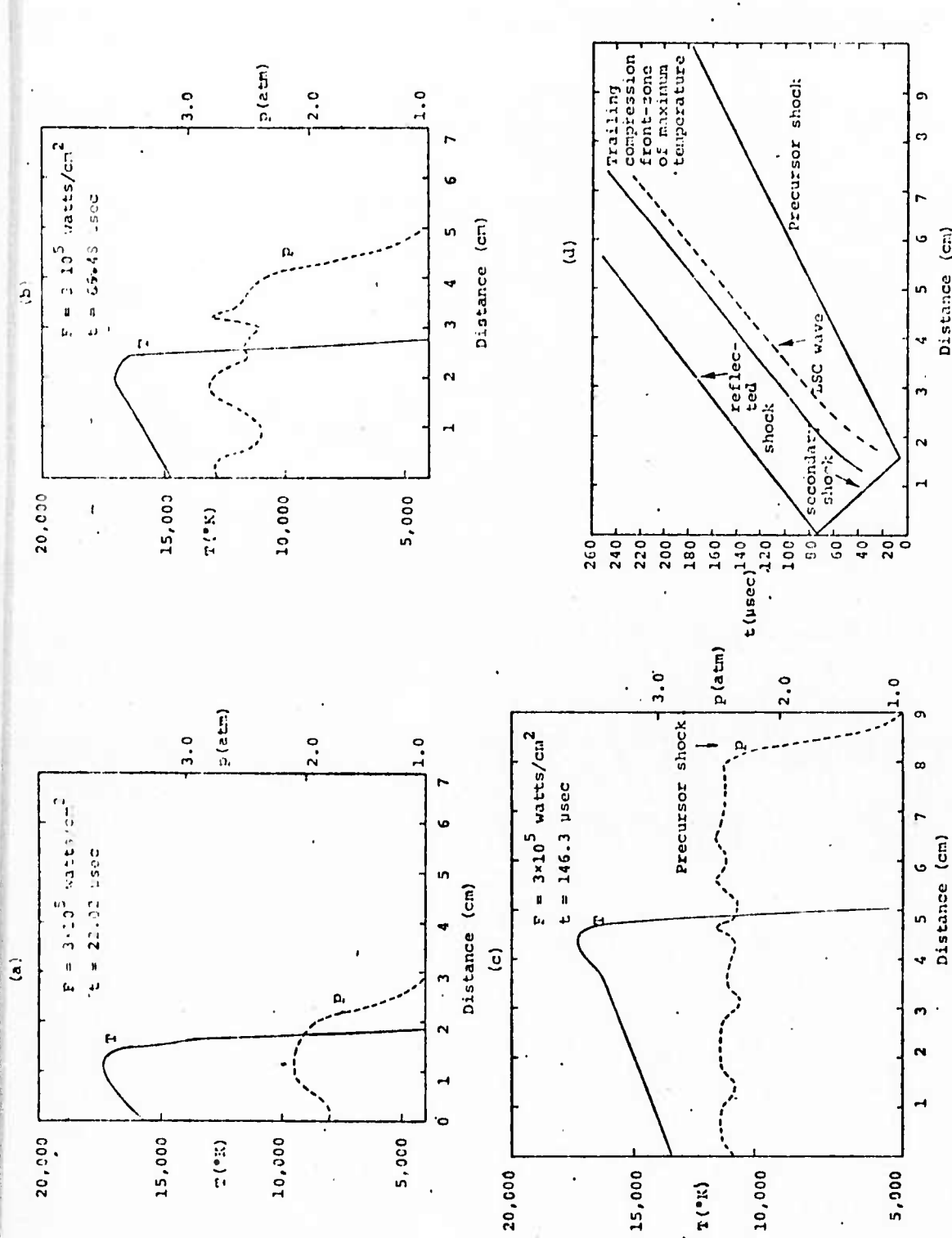
Figure 12. Plots of temperature and pressure for an incident flux level of 3×10^5 watts/cm² for times of (a) 22.02 μsec, (b) 66.47 μsec and (c) 146.3 μsec. In (d) we show an x-t diagram of the shock-LSC wave system.

via the absorption of laser radiation. It can be shown that the mechanical energy is a small fraction of the total energy absorbed by the plasma. Furthermore, the presence of the precursor shock produces a high pressure, high density region into which the LSC propagates. The formation and propagation of the LSC-shock is shown in Figure 12(a)-(c) where we plot temperature and pressure as a function of distance from the target for times of 22.02, 66.48 and 146.3 μsec respectively. It can be seen that the LSC wave propagates into a "modified ambient" pressure of about 2.5 atm, as opposed to the one atmosphere assumption implicit in the common deflagration assumption. However, it can be seen that the pressure is maintained nearly constant throughout the wave which is consistent with the deflagration approximation.

Before leaving Figure 12, an additional feature is included on Figure 12(d) which should be noted. We have shown the position of the LSC front as determined arbitrarily from the location of the 8,000 °K isotherm, i.e., the position of maximum brightness to the visible detector. Also, for comparison we show the position of a trailing compression front which in fact corresponds to the region of maximum temperature behind the wave. The separation between the two corresponds to the region of photon absorption and thus is the absorption length of the laser radiation.

For purposes of comparison, we include in Figure 13, an analogous calculation at a laser flux of 5×10^5 watts/cm^2. Due to the larger laser flux, it can be seen that the secondary shock reflects from the target in a shorter time. Also, we include on Figure 13(c) in addition to the temperature and pressure, the density profile. The existence of the precursor shock is evidenced by the sharp rise in p and ρ at about 9.6 cm. The pressure remains constant at about 3.5 atm. through the LSC wave front, whereas the density decreases
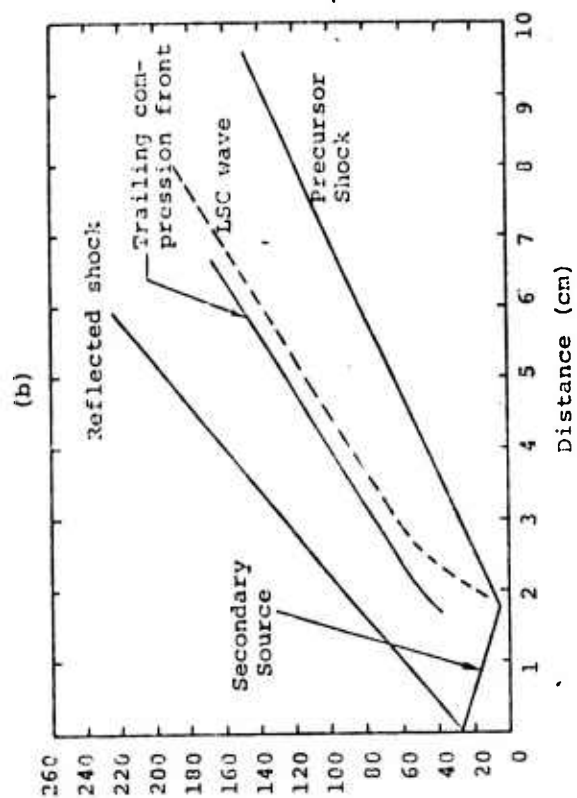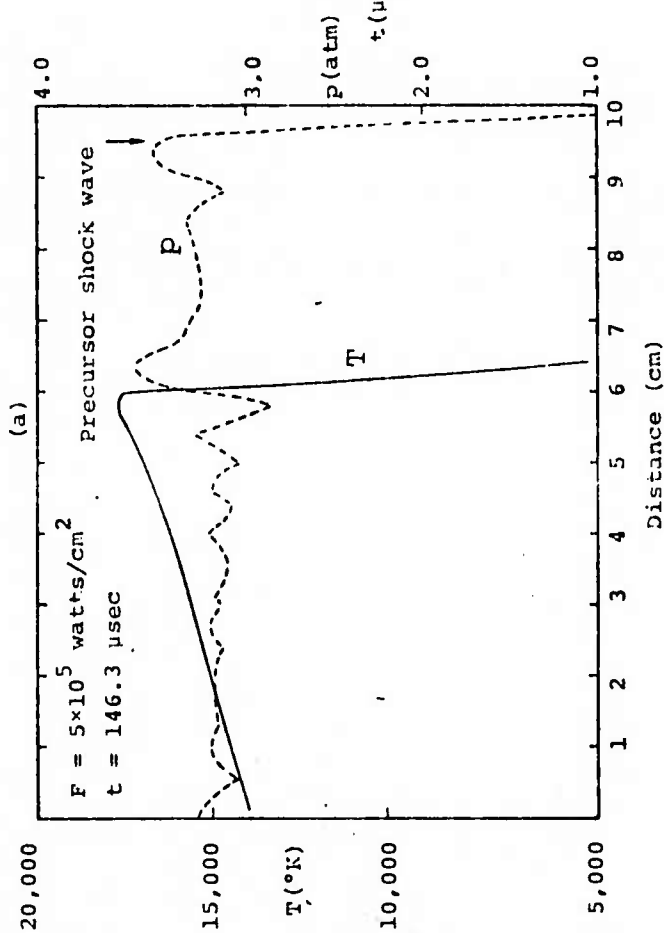
Figure 13 Plots of temperature and pressure for a flux level of 5×10^5 watts/cm^2.
(a) Time of 146.3 μsec, (b) x-t diagram of the shock-LSC wave system,
(c) logarithmic plot for the same case as (a) but including the density
variation.

39

(c)
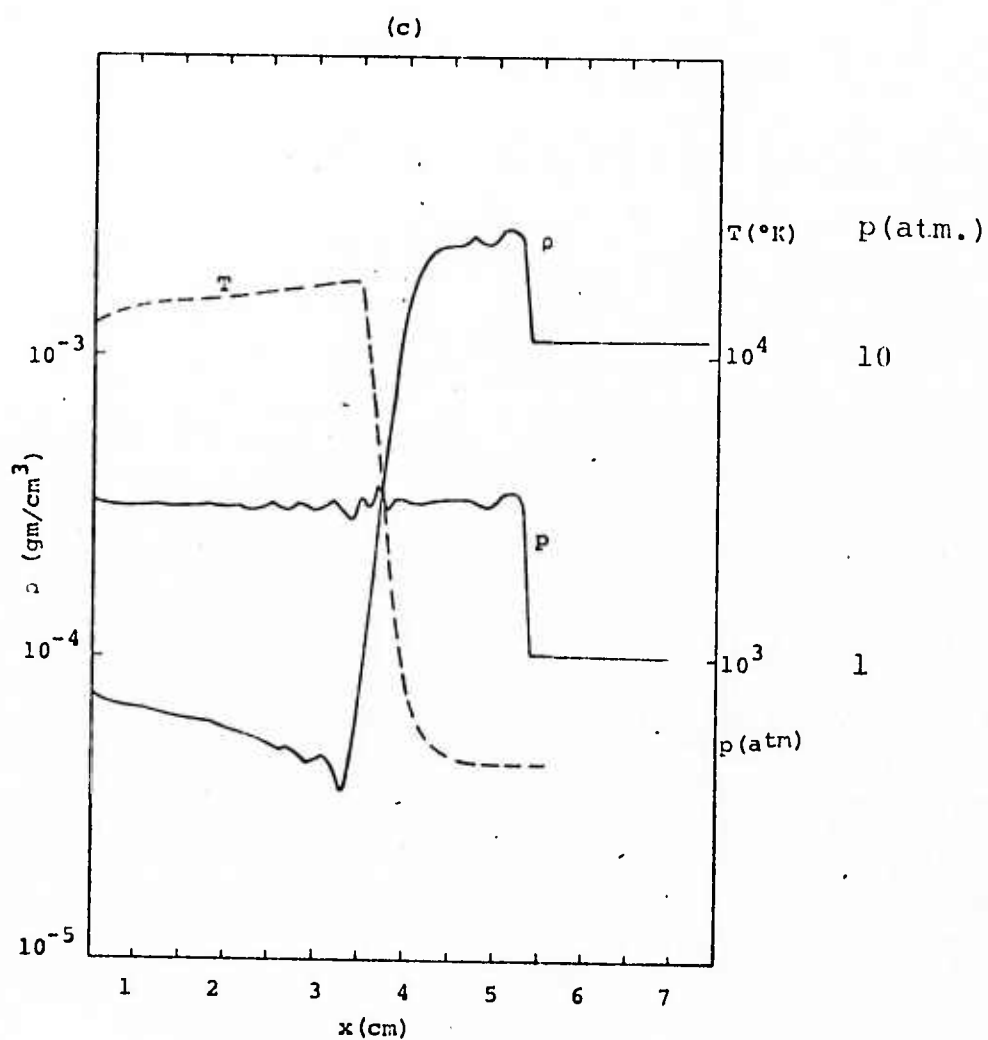
Figure 13 (continued)

40

sharply as the temperature increases due to laser heating. Evidence of subsequent compression of the plasma is apparent as the wave cools behind the maximum temperature region.

A summary of our calculations is shown in Figure 14, where we plot LSC wave velocity as a function of flux. For comparison, we plot the experimental correlation curve obtained at MSNW;[3b] $v = 13 \, Fpd$ (cm/sec) for flux density F(kw/cm^2), pressure p(atm) and beam diameter d(cm) for $p = 1$ atm and $d = 0.5$ cm.

The first observation is that our computed velocities are considerably higher than the experimental curve. This is due directly to the influence of the target on our calculated results. As we have indicated in Figures 12 and 13, the target influence persists to distances of at least 10 cm and a time scale of at least 200 μsec after LSC formation. The MSNW measurements were made at similar times and distances and it was maintained that "target free propagation" was observed due to the steady propagation of the LSC. This discrepancy with experiment will be discussed in Section 3.3.

Secondly, we show two velocity curves entitled long zone and short zone. The long zone calculation corresponds to an initial plasma length of 7 cm, whereas the second curve corresponds to a short zone of 1 cm length. The long zone curve shows a lower propagation velocity than the short zone calculation. This result indicates the sensitivity of the calculated results to the initial (ignition) conditions. The long zone case remains more free from the target (although not entirely free) than the short zone due to the longer time for the secondary shock to reflect from the wall and its attenuation.

Finally, we numerically "force" the computer code to reproduce the deflagration approximation (of constant one atmosphere propagation) by artificially compelling the pressure to remaind at one atmosphere. This technique serves

41
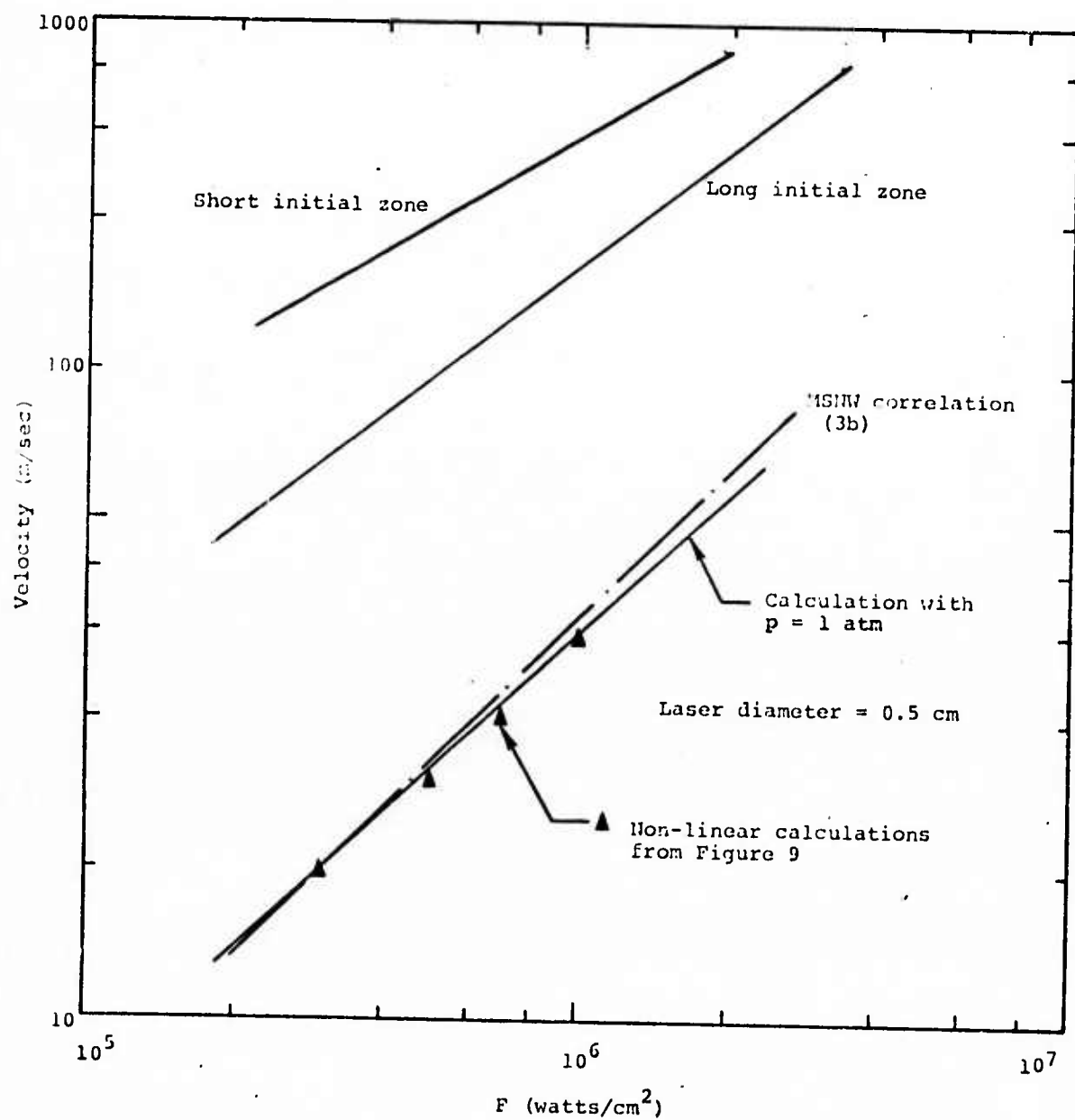
Figure 14. Plot a LSC wave velocity vs incident laser flux and comparison with experimental data.

two purposes; (1) by maintaining the pressure at one atmosphere, shock formation and target induced hydrodynamic processes are eliminated, thus the target free propagation mode is reproduced, and (2) mass is "artificially" lost from the system, albeit at a rate which is not necessarily real. The results obtained by this method of solution reproduce the MSNW correlation rather well. Finally, we also show for comparison, results from our non-linear solution obtained by the quasilinearization model discussed in Section 2. Both calculation techniques reproduce the results identically.

One further calculation was performed in which we placed a constant pressure (1 atm) boundary condition on the left end of the "tube", i.e., at the target surface. The secondary wave is thus not allowed to reflect. Results obtained by this technique lie midway between the "long zone" and "pressure uniformly equal to one atmosphere" results.

In order to convince ourselves that the initial temperature distribution was not too artificial and not having an exaggerated effect on the fluid dynamics, a calculation was performed for fifteen microseconds with the pressure held to one atmosphere, and then the calculation was continued in the normal way. The results seem to be quite similar for thermodynamic profiles and for the LSC wave trajectory.

3.3 DISCUSSION OF FOCUSED GEOMETRIC AND LATERAL EXPANSION EFFECTS

As was indicated in Section 3.1, two potential 2-D effects which we have studied are expansion due to focused laser beam geometry and radial expansion of the plasma beyond the confines of the laser channel.

If the beam is focused, the laser flux will be greater near the focus (say at the target surface) than at some distance away from the target. The LSC will thus propagate into regions of lower flux, thus explicitly reducing the velocity. Furthermore, due to the nonparallel channel into which the LSC propagates, the area through which flow occurs increases. The flow process corresponds to variable area flow in a channel with heat addition. Since the flow is subsonic, the area increase reduces the flow velocity. Results obtained from a series of calculations are shown in Figure 14. Here we plotted the position of the LSC front for the same laser flux at the focus but for channels with divergence half-angles of 0°, 2.58°, and 5.43° respectively. As can be seen, the trajectories are very similar for about the first 20 μsec of propagation. After that, however, the LSC velocity becomes progressively smaller as the divergence angle is increased.

In order to interpret these results, we must separate the effect of the reduced flux at a particular channel location from the purely hydrodynamic effect of increased channel area. If $v \propto Fr$ where F is the laser flux and r the channel radius, we find that simply from the reduced flux, that for a divergence half angle of ~5°, we would expect a velocity reduction of about 75% from the velocity of constant area flow. Within the uncertainty of locating the position of the front, we find from Figure 15, that the velocity reduction is about the same. We conclude, therefore, that the radial hydrodynamical expansion due to the increased channel area has negligible influence on the propagation velocity.

One further aspect of two-dimensional flow was studied. That is the radial expansion through the lateral boundaries of the propagation channel defined by the laser. As was indicated earlier and as is evident from Figures 12 and 13, the pressure behind the LSC wave and between the precursor shock

44
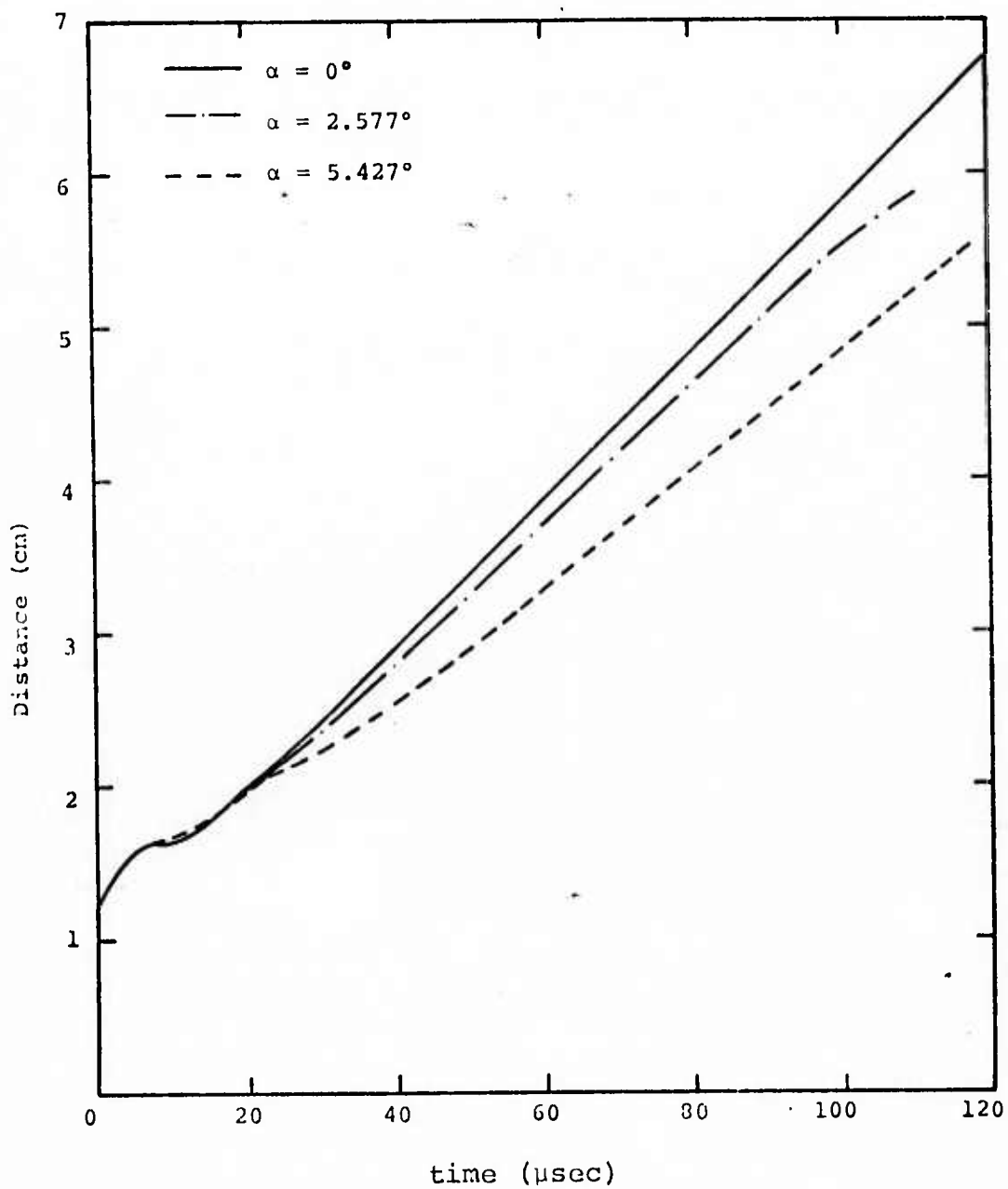
Figure 15. Distance-time plot for beam divergence angles of
0°, 2.577°, and 5.427°.

45

and the LSC wave is considerably greater than atmospheric.
Due to this pressure difference, it is expected that flow
will be induced in the radial direction. In order to obtain
a reasonable estimate - or to establish an upper bound on
this effect - we chose to implement the model which is pre-
sented in Appendix C. We reason that the maximum velocity
at which the flow could expand rapidly would be if the pres-
sure in the cylindrical plasma would induce a cylindrical
blast wave which propagates radially away from the plasma.
The model presented in Appendix C was used to calculate the
velocity at the channel boundary induced by such an outwardly
propagating blast. This velocity is then used to compute the
mass convected through the lateral channel boundary, which is
thus removed from each computational zone during the calcula-
tion. This model was used for all of our calculations, thus
its effect is included in all of the results included herein,
e.g., Figures 12, 13, 14. Accordingly, we find that even
including such radial mass loss from the flow field, our
calculations do not agree with the MSNW correlation (except
for the $p = 1$ atm calculation). This indicates that the
radial mass loss is not adequate to reduce the pressure
behind the precursor shock-LSC system over the distance and
time scale for which the calculations were performed; i.e.,
~ 200 μsec and 10 cm from the target. That this is true can
be seen from Figures 12 and 13 which indicate that the pres-
sure levels remain high over the duration of the calculation.
For instance, we find that for the case shown in Figure 3
(5×10^5 watts/cm^2, R = .25 cm), the mass loss rate from a
zone between the shock and the LSC is of order 0.5 grams/sec.
Since the mass per zone is about 10×10^{-5} grams, the charac-
teristic decay time, 10×10^{-5} grams/0.5 grams/sec = 2×10^{-4}
sec, is about 200 μsec. That is, about 200 μsec subsequent
to passage of the wave. We find no evidence of a signifi-
cant pressure reduction behind the wave in our calculations,
however. But, we do find that the combined effect of a

radial velocity and radial conduction is of sufficient magnitude to produce a plasma extending beyond the confines of the light channel as found in the holograms and framing photographs obtained by MSNW.[3a,b]

We are thus faced with the conclusion that according to our numerical calculations, the 2-D effects of radial flow and channel expansion due to the focal geometry are not adequate to explain the experimental results obtained by MSNW. However, use of the deflagration approximation brings our calculations into good agreement, thus indicating that any target effects present in the MSNW experiments are small indeed. We must therefore conclude that according to the experimental data, more target decoupling occurs in reality than is predicted by a one-dimensional calculation. The two-dimensional expansion over the target surface must weaken the reflected shock wave and result in additional decoupling over the time scale of the experiment.

In order to model this phenomena, a 2-D calculation is desirable. However, we feel that the stagnation point flow field is undoubtedly highly complicated by turbulent mixing with the expanding target material. A calculation of this complicated phenomena, including a reasonable description for the target vapor-shock wave interaction is beyond the scope of the present study. Further work in this area is necessary before such a computation will bear any resemblance to reality - and thus be worth pursuing.

At the present time, however, for the purpose of systems studies, interpretation of data and experimental guidance, we feel that either our non-linear model, or the one-dimensional variable area model described herein when coupled with the deflagration approximation is adequate. Inclusion of

47

non-linear effects and loss terms remove most of the discre-
pancies noted by MSNW. The results obtained by us as dis-
cussed in this section and in Section 2 seem to be physically
consistent, and when interpreted properly are consistent with
experimental observations.

One area which has not been studied, however, and which
could be addressed by technique such as those described in
Section 3, is the transition from LSC to the LSD mode. This
could be very important for systems implications when using
repetitively pulsed lasers operating at low cw, but high-
peak powers. We have shown the existence of a precursor
shock whose strength increases with increasing laser fluence.
The electron-cascade breakdown behind the precursor shock is
responsible for absorption in the shock zone and ultimate
decoupling of the shock from the LSC. The flux region above
about 5×10^6 watts/cm^2 will thus be dominated by this transi-
tion regime which evidences combined LSC and LSD phenomena,
and must be studied by numerical techniques due to the com-
plexity of the hydrodynamic processes involved.

3.4   THE COMBUSTION WAVE MODEL

The problem was solved from the numerical integration
of the Eulerian conservation equations for mass,

$$\frac{\partial \rho}{\partial t} + \nabla \cdot (\rho \underset{\sim}{u}) = 0 \qquad , \tag{28}$$

for momentum,

$$\frac{\partial (\rho u)}{\partial t} + \nabla (\rho \underset{\sim}{u}^2) + \nabla p = 0 \qquad , \tag{29}$$

and for energy,

$$\frac{\partial (\rho e)}{\partial t} + \nabla \cdot (\rho \underset{\sim}{u} e) + p \nabla \cdot \underset{\sim}{u} + \nabla \cdot \underset{\sim}{q} = 0 \qquad , \tag{30}$$

48

where ρ is the density, u is the velocity, p is the pressure, e is the specific internal energy and q is the generalized heat flux (from radiative absorption and conductive and radiative conduction).

To integrate these terms numerically, an integration scheme developed by Chapman[20] has been used. The scheme used is explicitly given by Chapman and differs in the integration of his Equation 3.21:

$$\frac{\left(\Lambda_{j+\frac{1}{2}}^{n+1} e_{j+\frac{1}{2}}^{n+1} - \Lambda_{j+\frac{1}{2}}^{n} e_{j+\frac{1}{2}}^{n}\right)}{\Delta t} = C + W + L \tag{31}$$

where C is the conduction term,

$$C = (\rho U_e A)_j^{n+\frac{1}{2}} - (\rho U_e A)_j^{n-\frac{1}{2}} \tag{32}$$

W is the work term,

$$W = PQ_{j+\frac{1}{2}}^{n+\frac{1}{2}} \left(A_{j+1} U_{j+1}^{n+\frac{1}{2}} - A_j U_j^{n+\frac{1}{2}}\right) \tag{33}$$

and L is the term peculiar to the LSC problem,

$$L = J_R + J_C + C_R + C_C + A \tag{34}$$

Here J_R and J_C are the leakage of energy from the section by lateral radiative and conductive diffusion, C_R and C_C are the transmission of energy between mesh cells by radiative and conductive diffusion,

$$C_R = \left\{\left[(\lambda_R)_{j+1}^{n+1} A_{j+1} + (\lambda_R)_j^{n+1} A_j\right]\left[T_{j+1}^{n+1} - T_j^{n+1}\right]\right. \tag{35}$$

$$\left. - \left[(\lambda_R)_j^{n+1} A_j + (\lambda_R)_{j-1}^{n+1} A_{j-1}\right]\left[T_j^{n+1} - T_{j-1}^{n+1}\right]\right\} \Big/ (2\Delta X) \quad,$$

$$C_C = \left\{ \left[(\lambda_C)_{j+1}^{n+1} A_{j+1} + (\lambda_C)_j^{n+1} A_j \right] \left[T_{j+1}^{n+1} - T_j^{n+1} \right] \right. \tag{36}$$

$$\left. - \left[(\lambda_C)_j^{n+1} A_j - (\lambda_C)_{j-1}^{n+1} A_{j-1} \right] \left[T_j^{n+1} - T_{j-1}^{n+1} \right] \right\} \Big/ (2\Delta X) \quad ,$$

and A is the absorption of energy from the laser beam

$$A = 1 - \exp -\kappa_j^{n+1} \Delta x \quad \Delta F_{j+1}^{n+1} A_{j+1} \qquad . \tag{37}$$

F_{j+1} is the laser flux impinging on mesh cell j from the direction of j+1. The flux is attenuated by the formula

$$F_j^{n+1} = F_{j+1}^{n+1} \left[1_m - \exp\left(\kappa_{j+1}^{n+1} \Delta x \right) \right] A_{j+1} / A_j \qquad , \tag{38}$$

where $F_{j+1}^{n+1} = F_o$, the incident flux. The notation used in defining C and W are given by Chapman and the formulas for the terms contained in L are given in Section 3.2 of Boni, Cohen and Su.[17]

The energy difference equation is solved iteratively since W and L are functions of $e_{j+\frac{1}{2}}^{n+1}$. This is due to the fact that the work term contains pressure,

$$P_{j+\frac{1}{2}}^{n+1} = P\left(\rho_{j+\frac{1}{2}}^{n+1} , e_{j+\frac{1}{2}}^{n+1} \right) \qquad ,$$

and L is a function of the temperature,

$$T_{j+\frac{1}{2}}^{n+1} = T\left(\rho_{j+\frac{1}{2}}^{n+1} , e_{j+\frac{1}{2}}^{n+1} \right) \qquad .$$

These two intrinsic functions are determined, in the case of air, by a simple fit to Predvoditelev's data,[15]

$$e = 5.036 \times 10^3 T^2 - P/\rho \qquad ,$$

for temperatures greater than 2000 °K, and by a perfect gas approximation for lower temperatures,

$$e = \frac{5}{2} kT \qquad .$$

This equation of state is plotted in Figure 16. The pressure is given by the formula

$$p = (n_e + n_m)kT \qquad ,$$

where n_e and n_m are the densities of free electrons and molecules, respectively. The density of free electrons is calculated assuming Saha equilibrium

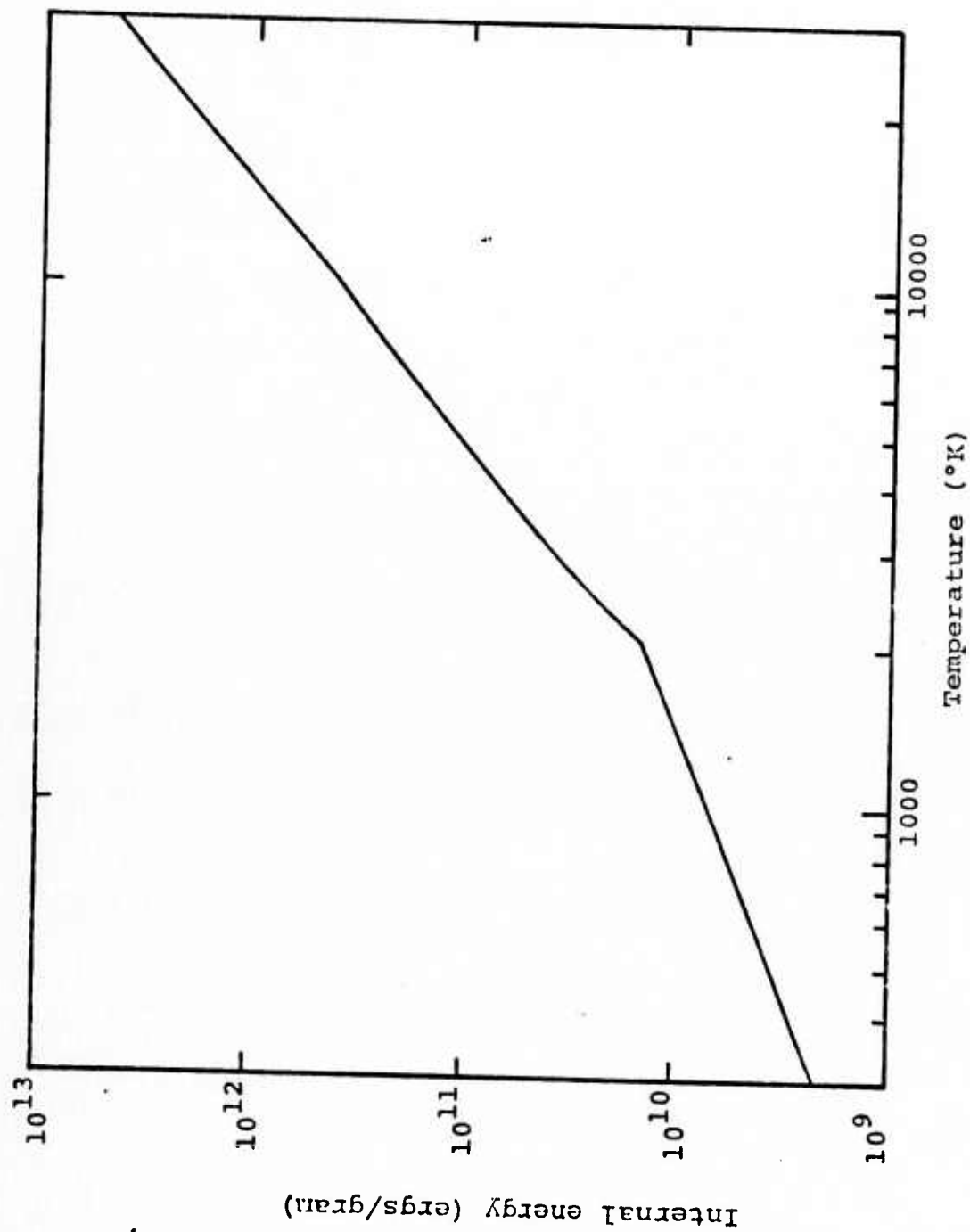$$\frac{n_e^2}{n_m - 2n_e} = 2\left(\frac{2m_e kT}{h^2}\right)^{3/2} \frac{g_+}{g_a} e^{-I/kT} \qquad .$$

Figure 16. Equation of state for air used in the numerical calculation.

52

Part 2: Measurements on the Effect of
Particulate Matter on Air Breakdown by 1.06μ

A.A. Boni

D.A. Meskan

4. EXPERIMENTAL INVESTIGATION OF THE EFFECTS OF PARTICULATE MATTER ON SHORT WAVELENGTH PULSED LASER PROPAGATION

4.1 INTRODUCTION AND BACKGROUND

During the past several years, theoretical work at S [22] as well as work at the Air Force Weapons Laboratory[23] has been reasonably successful as a framework for the interpretation of observations based on dirty-air breakdown experiments conducted at Avco-Everett Research Laboratory[24], Lincoln Laboratory[25] and at United Aircraft Research Laboratories[26]. Theoretical calculations have been performed which are based on a model of particle induced breakdown which considers vaporization of the particle due to laser heating, followed by an electron cascade process initiated either in the heated particle vapor or in the adjacent air which has been shock-heated as a result of the rapidly expanding particle vapor. It has been pointed out that this picture of the dirty-air breakdown problem is similar in many respects to the target-interaction problem except for the different geometry and spatial scale. Indeed, the experimental LSD thresholds as observed by Hall for plane-target interactions — "infinite diameter particles" — are about the same as those observed in the above mentioned air breakdown experiments. Specifically, as we have pointed out previously[26] the laser fluence associated with containment breakdown in air and for the LSD thresholds are both of order 10 joules/cm^2 for pulse times of order 10^{-7} sec and are consistent with an infinite diameter particle extrapolation. In any event, it has been shown both theoretically and experimentally that the breakdown threshold for a particle-laden atmosphere may be several orders of magnitude less than the clean air breakdown threshold of about 3×10^9 watts/cm^2 for CO_2 wavelengths depending on pulse length and the particulate concentration and particle size distribution.

53

The main thrust of the effort in the community over the past several years has been to correlate and to understand both the long-pulse and short-pulse experimental data for CO_2 laser propagation, i.e., at 10.6μ including the effect of atmospheric particulate impurities. However, since it has been shown that high fluence CO_2 laser propagation through the atmosphere is limited due to non-linear effects, viz, thermal blooming and gas breakdown, and that more optimum propagation characteristics may exist at reduced wavelengths, a large amount of work has been initiated to develop a high-intensity laser source which operates efficiently at wavelengths lower than 10.6μ. Accordingly, a significant amount of work has gone into developing chemical lasers, such as the DF laser, cold cathode electron beam stimulated lasers such as the CO laser, hybrid chemical-electrical excitation lasers, and finally most recently, relativistic electron beam stimulated lasers which operate in the visible and UV regions of the spectrum.

Based on inverse bremstrahlung scaling as discussed in Appendix D, it is anticipated that breakdown thresholds at reduced wavelength should scale directly with the square of the laser frequency ω. Accordingly, the non-linear problem associated with gas breakdown may be less restrictive at lower wavelengths and a higher fluence laser pulse may be propagated. Furthermore, it is expected that the breakdown threshold flux increases as the laser pulse length becomes shorter. These observations follow from the classical limit of a simple energy balance equation, c.f. Appendix D, which relates the rate of growth of average electron energy to the electromagnetic field of the laser.

It is obvious that many potentially complicated effects could and have been included in calculations such as those carried out by us previously for CO_2 laser interactions. However, the utility of a simplified approach is highly desirable.

54

The importance of timely, accurate and relevant experimental data in the guidance and formulation of theoretical model development is recognized as essential for the attainment of a reliable solution to the objectives of the DARPA laser program. For this reason, and because of the importance of obtaining answers to the wavelength and pulse length scaling question, we have performed a small number of measurements related to dirty-air breakdown at Nd-laser wavelengths. The choice of the Nd laser (1.06μ wavelength) was based on the availability of an operational, high fluence laser facility at reduced wavelength and pulse length so that interim information could be obtained prior to the availability of appropriate gas laser systems.

Experimental data are obtained and results presented for breakdown of filtered air, SiO_2 fibers (9μ) and carbon fibers (6.6μ and 68μ) by 30 nsec, 1.06μ laser pulses. It is shown that the results correlate well with data obtained at 10.6μ and that the breakdown thresholds scale, within the experimental uncertainties, with the square of the laser frequency between 1.06μ and 10.6μ. The lowest threshold measured is for the 68μ carbon fiber and is 2.3×10^{10} watts/cm^2 for the 30 nsec pulse length. Lower values are expected for longer pulses. The smaller diameter impurities result in increased breakdown thresholds approaching the flux limited value of 3×10^{11} watts/cm^2 for clean air. As has been found for breakdown at 10.6μ, we find an independence of breakdown threshold on the material composition of the impurity.

4.2   EXPERIMENTAL

The test matrix included a limited number of experiments related to dirty-air environments but was principally concerned with breakdown of single, small diameter fibers. We performed measurements on SiO_2 fibers (9μ diameter) and carbon fibers (6.6μ and 68μ diameter) in both air and argon atmospheres. In addition, the breakdown threshold for filtered air (0.1μ filters) was measured. As mentioned, the experiments were conducted by S^3 at the Battelle Columbus Laboratories on the CGE 640 Nd: Glass facility with the laser operated in the single pulse, 30 nsec FWHM mode. This facility is capable of producing up to 450 joules at 30 nsec, although we used significantly less energy in our experiments. A schematic layout of the experimental arrangement is shown in Figure 17.

A one foot diameter, one foot high, evacuable metal cylinder was used as the test chamber. The chamber was equipped with a number of ports around its circumference for diagnostic access. The main laser pulse is brought into the chamber unfocused, with a diameter of 7 cms. All of the beam focusing was performed inside the chamber with a lens of focal length 3 meters. An extension port to facilitate the long focal length lens was provided. The flux density at the focal volume was varied by changing the laser operating parameters, i.e., by varying the energy input and number of amplification stages, rather than by repeated changes of the focusing lens and/or the size and location of the focal volumes which was maintained constant throughout the experiment. Laser beam diagnostics include incident energy, beam size and spatial distribution, and time dependence of the incident pulse. The incident energy and pulse time dependence and focal position was monitored for each shot.

Diagnostics of the breakdown event for each shot included the following: (1) a measurement of the transmission of the pulse through the focal region, and the time dependence
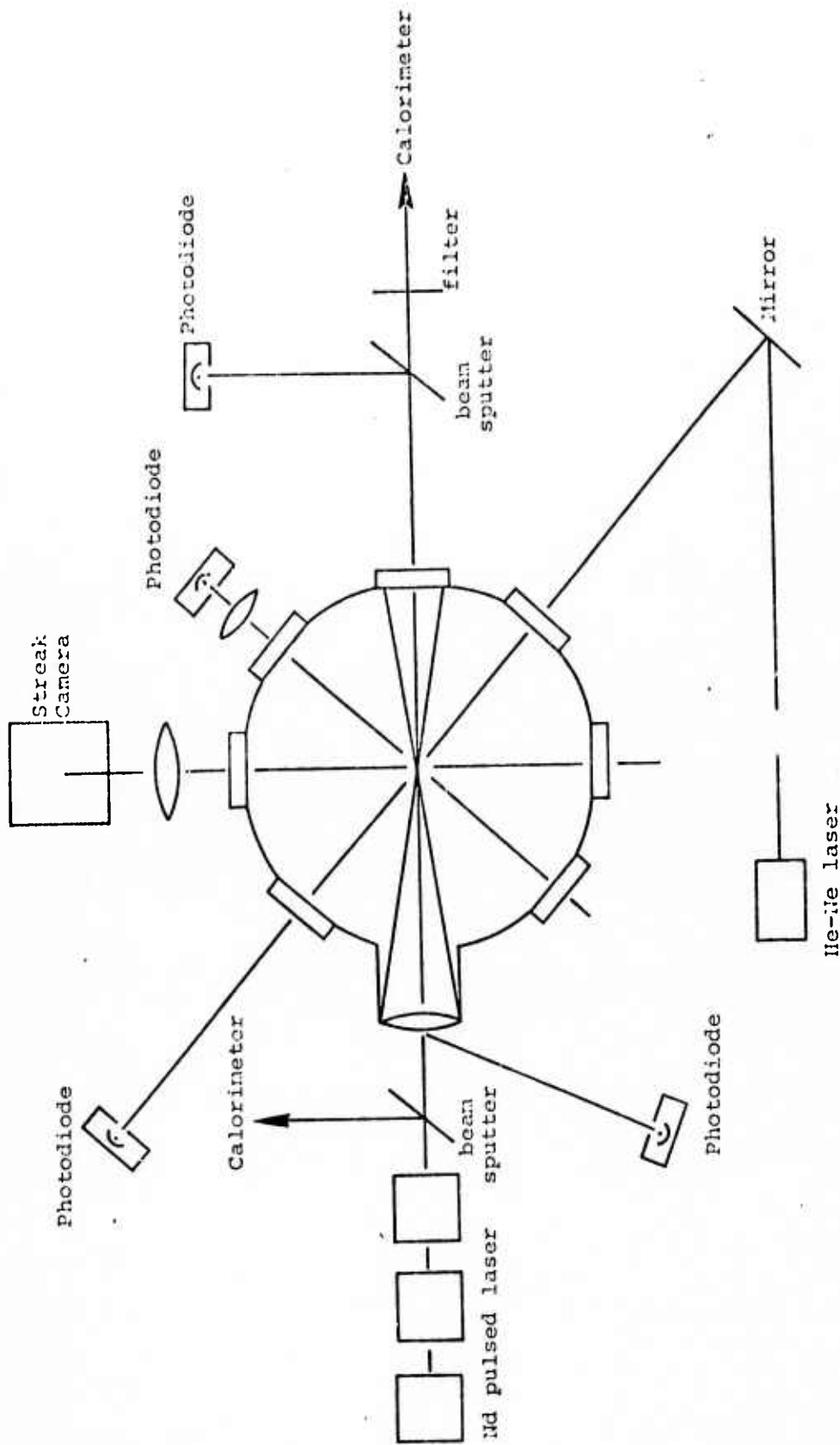
56

Figure 17. Experimental arrangement for breakdown studies.

57

of the transmitted pulse, (2) a measurement of the time-resolved emission from the breakdown region, (3) open-shutter photography of the breakdown region, (4) streak camera photography of the breakdown region, and (5) time resolved cross beam absorption by use of a He-Ne laser.

It was determined that the transmitted laser pulse and plasma emission measurements were good indicators of the breakdown event. The streak camera records were useful in establishing the location of plasma luminosity at distances away from the fibers; however, a time-delay fault in the camera (of 123 nsec) did not allow the plasma motion during the laser pulse to be measured. Since the program funding provided for only a one week stay at Battelle, the problem was not resolved and accordingly the streak camera records were of limited usefulness. One additional difficulty encountered with the experiment was with the cross-beam transmission measurement. It was discovered that due to a predominance of fiber material in the plasma, plasma emission at 6328A was sufficiently great that meaningful absorption measurements could not be obtained. In retrospect, a polarizer placed in front of the photodiode should be adequate to eliminate the unpolarized plasma emission from interference with the polarized He-Ne radiation.

In any event, good and reproducible data were obtained on laser transmission through the focal volume, plasma emission and open shutter photography. By a combination and intercomparison of these diagnostics we could determine whether breakdown occurred and at what time during the pulse, the per cent transmission through the focal region and the shape of the breakdown plasma so produced. Also, measurements of the plasma emission have been found to be useful indicators of breakdown and correlate well with the through-transmission measurements. Due to the emission from the heated and vaporizing fiber, the emission level increases during the laser

pulse and then decays well after the laser is turned off.
However, the initiation of gas breakdown causes a significant
increase in the emission level over and above that present
due to fiber heating and vaporization. The duration of the
"plasma flash" then indicates both the existence and the
duration of the breakdown plasma.

The size of the laser beam at the focal point was
measured by calibrated "burn paper." It was determined that
the focal spot was 0.075 cm in diameter (mean diameter for
a slightly oblong spot of .070 x .080 cm) at the one-half
power point.

4.3   EXPERIMENTAL RESULTS

First of all, we discuss features of our observations.
For the air breakdown experiments, a typical plot of the
incident and transmitted laser pulse and the plasma luminosity
trace is shown in Figure 18. It is shown that breakdown
occurs very near the peak power point as evidenced by the sharp
reduction in the transmitted pulse trace. The plasma luminos-
ity trace indicates that the emission increases to a maximum
and then decays over a time period of about 1 μsec. This
value of decay time is typical of all our results. The photo-
diode used to monitor the plasma emission was displayed on a
much longer time scale than the laser pulse, thus the emission
rise time was not determined. The maximum value of the plasma
intensity and the decay time were the primary parameters of
interest.

Two separate methods were utilized to establish the
breakdown threshold and will be illustrated for the case of
the filtered air. First of all we plotted the percent trans-
mission through the focal region as a function of energy
incident onto the focal spot. As is shown in Figure 19, the
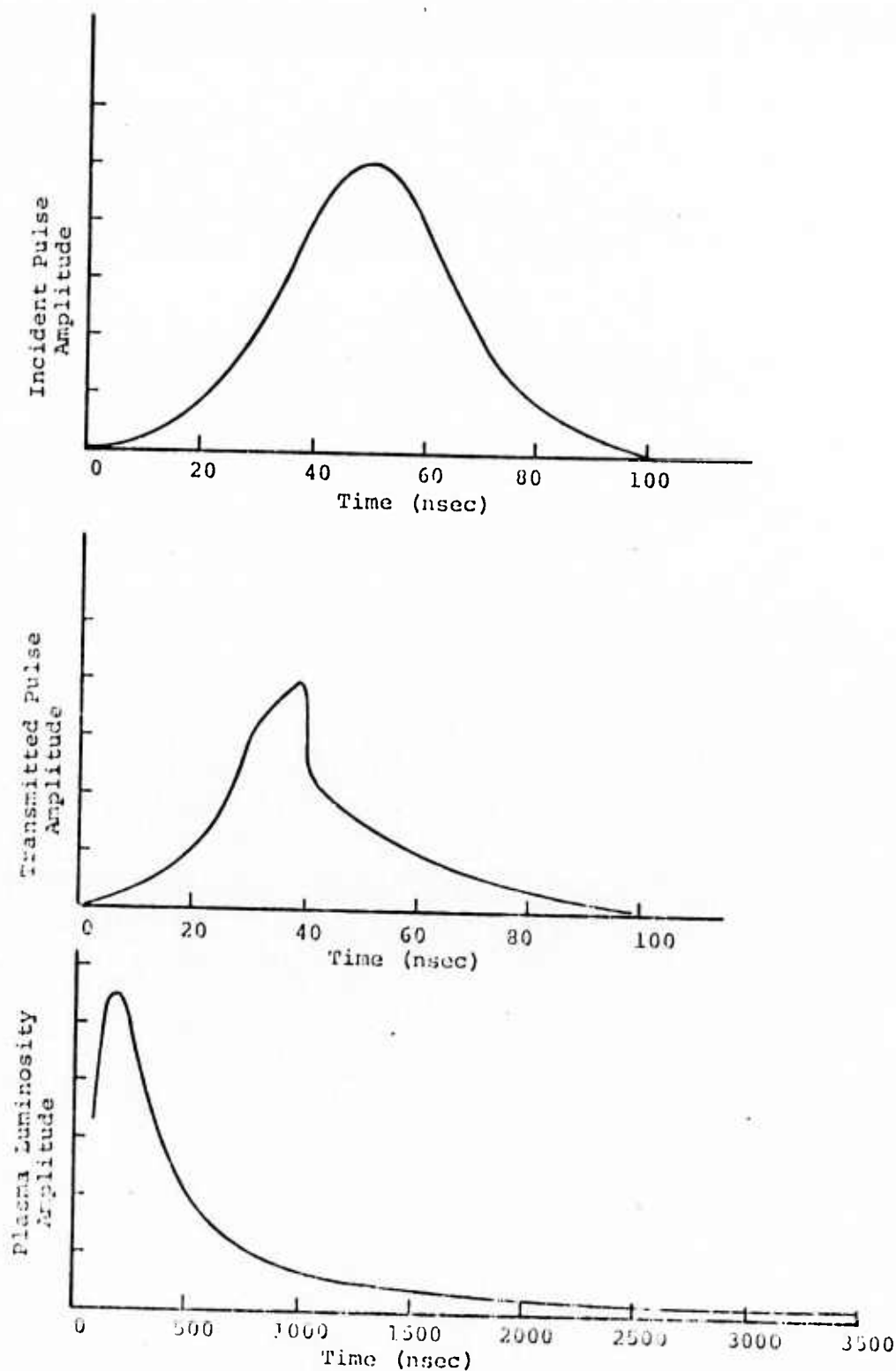transmission remains at a constant high value until the

Figure 18. Incident laser pulse, transmission through the focal region for air breakdown, and emission from the breakdown plasma.
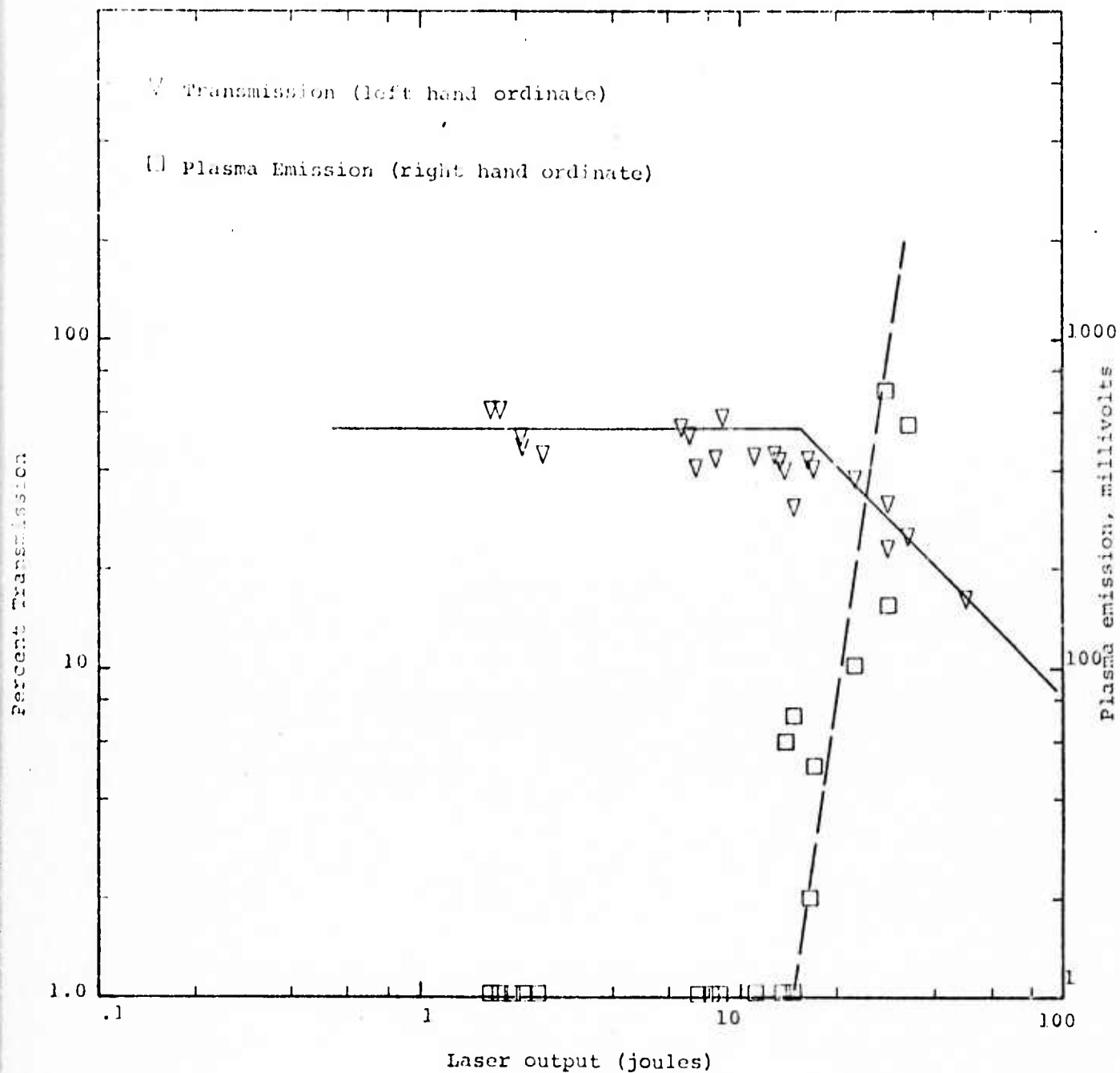
Figure 19. A plot of percent transmission through the focal region and emission from the breakdown plasma as a function of laser energy incident onto filtered air.

15 joule point, at which a sharp break occurs and the trans-
mission drops rapidly to less than 10%. Also on Figure 19, we
plot the emission from the breakdown region as measured by a
monitor photodiode. It is seen that below 15 joules, no de-
tectable radiation is emitted, whereas for laser energies
greater than 15 joules, the emission from the plasma rises
rapidly as the laser fluence is increased. This is the visible
spark or flash which occurs upon breakdown. It is believed
that these two methods utilized simultaneously (along with the
observation of a sudden drop in the transmitted laser pulse
trace) present a clear and unambiguous determination of the
existence of breakdown.

The energy of 15 joules onto a focal spot area of
4.4×10^{-3} cm^2 for a 30 nsec pulse yields a breakdown threshold
of 1.1×10^{11} watts/cm^2. Since the focal spot diameter is
about 0.075 cm, it is believed on the basis of theoretical cal-
culations[22] that diffusion losses are negligible. The value
for breakdown threshold is about a factor of 2-3 lower than
the commonly accepted value for clean air. Even though we
filtered the inlet air by use of a 0.1μ filter and evacuated
the test chamber before admitting the test gas, the reduction
in threshold from the clean air value indicates that presence
of some impurity particles of diameter as great as 1μ. This
observation is not surprising, if one recognizes that the focal
volume subject to the breakdown fluence in our experiments was
relatively large due to the use of a three meter focal length
lens. Thus the peak intensity region was over 1 cm long and
the presence of a very low number density of impurities could
lead to the existence of containment particles within such a
large focal volume. For instance, with a focal volume of
4×10^{-3} cm^3, a particle number density of about 2.2×10^2 cm^{-3}
would lead to the existance of one particle within the focal
volume. Indeed, the open shutter photographs indicated that the
breakdown region was not localized to one spot from shot to

shot for the air shots, indicating the presence of particles within the focal volume. Also we saw cases of more than one breakdown within the focal volume. (Placement of the fiber within the focal volume, however, always localized the break-down origin at the fiber.) In any event, the purpose of mea-suring the air breakdown threshold in these experiments was to characterize the environment in which the fiber breakdown experiments would take place. It has been shown that the back-ground gas breakdown threshold is considerably greater than that measured for the smallest fiber and thus does not affect determination of the particle induced breakdown thresholds.

Subsequent to characterizing the background gas environ-ment, we proceeded to determine the breakdown threshold of the SiO_2 and carbon fibers. A data reduction technique similar to that described previously for the filtered air was employed. The only significant difference between the data reduction pro-cedure for the fibers and that for the air is that the fibers affected the nature of the plasma emission curves due to the heating and vaporization of the surface of the fibers. In-stead of a non-detectable level of plasma emission until break-down occurred, it was noted that the plasma emission rose slow-ly with increasing laser fluence. Then, at the threshold, a break in the curve occurred and the emission rose much more rapidly with increasing laser fluence.

One other interesting feature of the transmission curves is illustrated in Figure 20 for the case of the 68μ carbon fiber. Here, we present two transmitted pulse curves, illus-trating the behavior very near the breakdown threshold. It is shown that just under threshold, breakdown begins at the peak power point. However, the breakdown is not self-sustain-ing and dissipates quickly as the laser fluence decreases. The plasma emission remains low as is shown.

Just slightly over threshold, however, the breakdown begins before the peak power point is attained. High beam
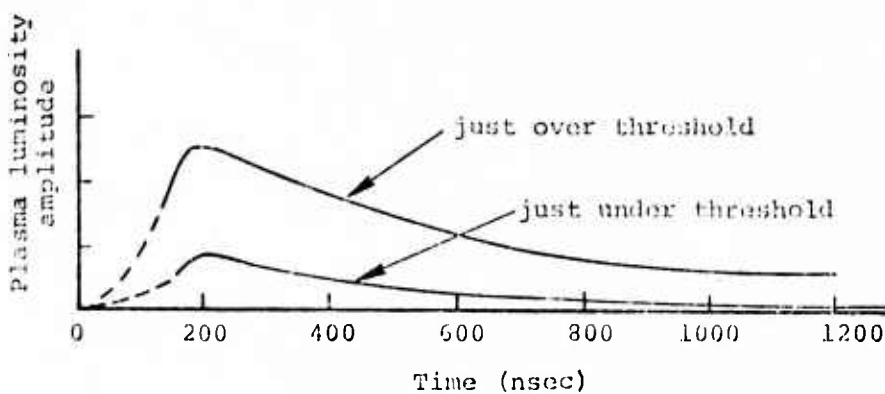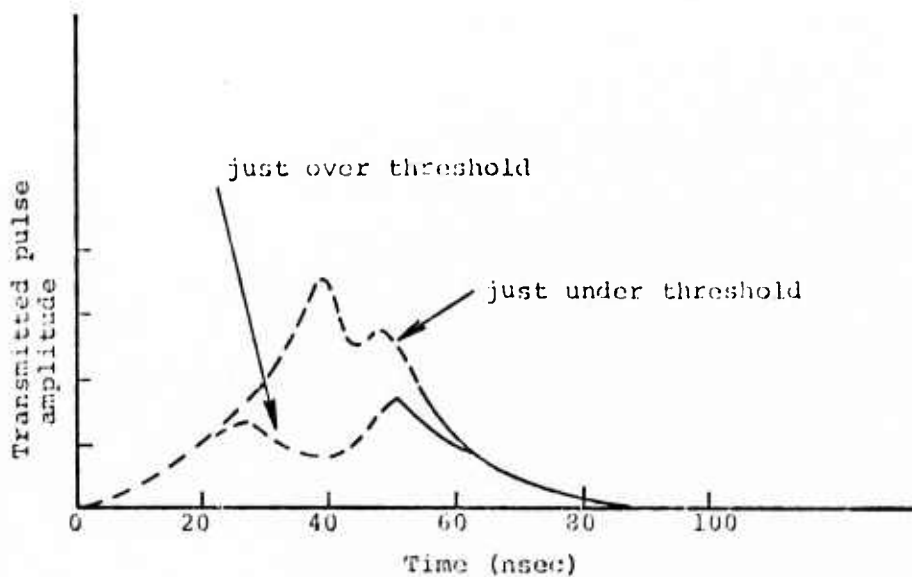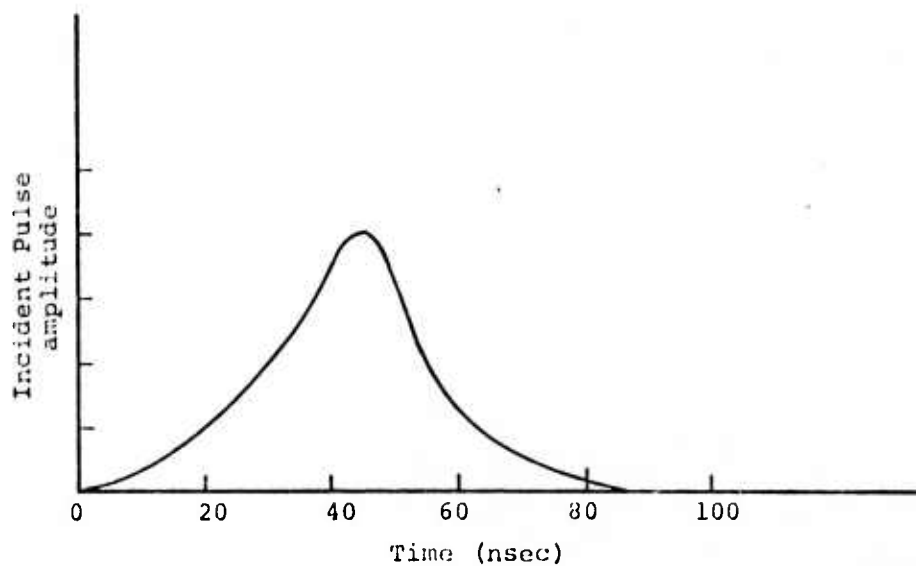
Figure 20. A plot of the incident and transmitted laser pulse with a 68μ carbon fiber located at the focus. Also shown is the emission from the breakdown plasma.

64

attenuation is maintained throughout the laser pulse. In the example shown, the threshold is not exceeded by much, however, and partial transmission is recovered as the laser fluence decreases. Also note the significant increase in plasma emission in the "just over threshold" case.

A further increase in laser fluence produces full breakdown and the transmitted pulse remains near zero for the full duration of the laser pulse. Near zero transmission implies full blocking of the beam, which indicates that the breakdown plasma expands rapidly to fill the cross section of the focal volume and subsequently propagates up the beam as a LSD wave. The open shutter photographs show a bright luminous column of diameter equal to the focal diameter propagating up the beam towards the laser source.

In any event, we have established the breakdown threshold for 68μ carbon, 6.6μ carbon and 9μ SiO_2 fibers as 2.3×10^{10} watts/cm^2, 4.6×10^{10} watts/cm^2 and 6.1×10^6 watts/cm^2 respectively for the fibers placed in air.

The carbon fiber experiments were repeated in a filtered argon environment also. In plotting the % transmission and plasma emission curves versus incident laser fluence, it was not possible to distinguish any difference for the breakdown thresholds between the fibers located in air or in argon. This result is consistent with previous measurements[28] where it was found that the breakdown threshold in N_2 and Ar were practically identical for a background pressure of one atmosphere.

In Figure 21, we summarize our results and compare with those of other investigators. First of all, we use the results of Lencioni[29] who correlated the available data at 10.6μ to obtain a plot of breakdown flux versus laser pulse length, including the dependence on particle size. In order to compare with the 1.06μ data, we have scaled the 10.6μ curves by a
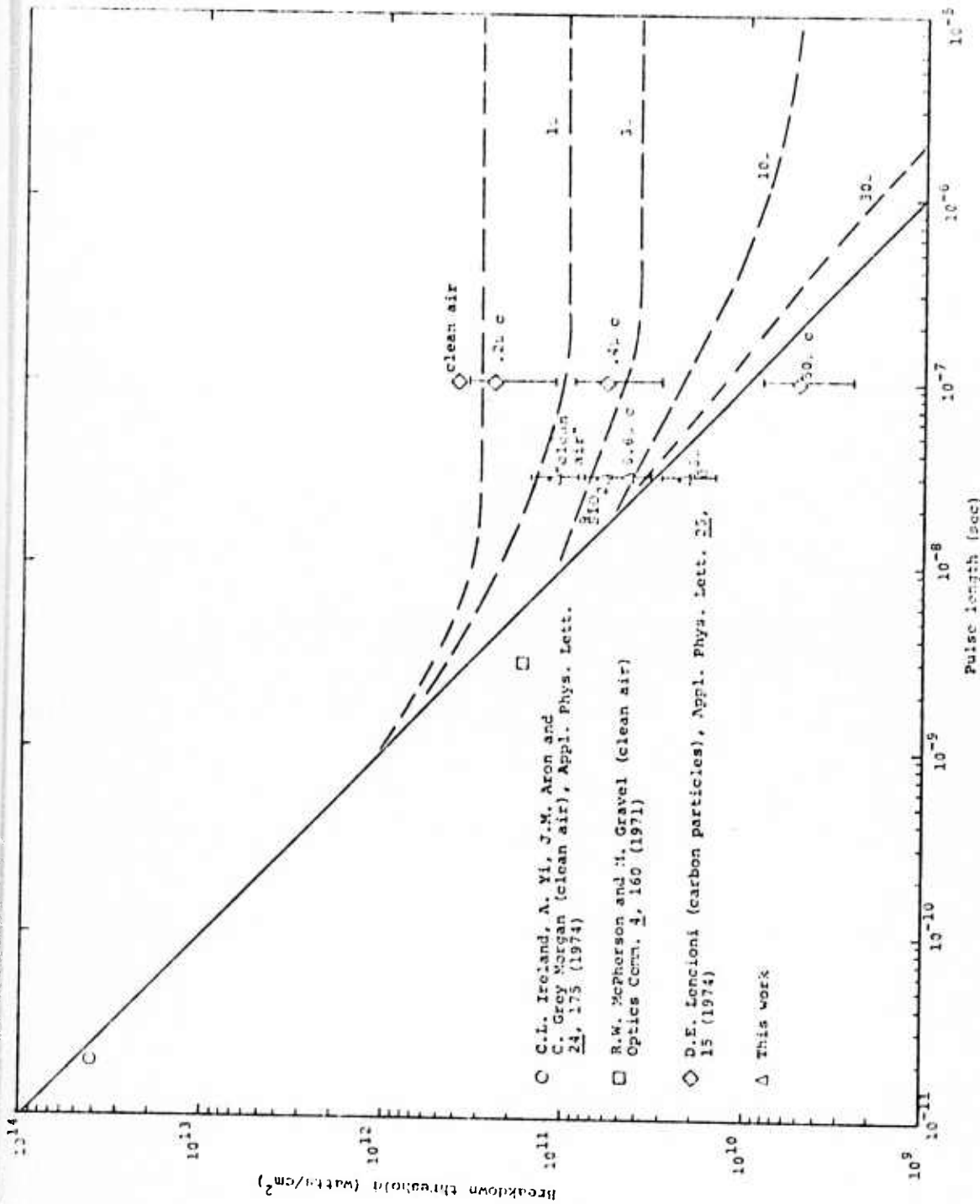
Figure 21. A plot of breakdown threshold as a function of laser pulse length summary for 1.06μ interaction. The curves are the results for 10.6μ scaled up by a factor of 100.

factor of 100. The curve shows two distinct regimes corresponding to short and long pulse propagation. For short pulse propagation, i.e., $\leq 10^{-9}$ sec, the constant energy regime exists. The curve shown has a slope of 1000 joules/cm^2. For pulse times greater than 1 nsec, the curve breaks and makes a transition to the constant flux regime. It is shown that the effect of increasing particle diameter is to decrease the threshold and to increase the pulse duration at which transition to the constant flux regime occurs.

The data obtained by us is plotted at the 30 nsec pulse duration. As can be seen, within the experimental error, which is estimated to be about ±30%, our results indicate that the $1/\lambda^2$ scaling according to the inverse bremsstrahlung arguments seems to be valid. In addition, results recently obtained by Lencioni[30] (after our experiments were completed) indicate that $1/\lambda^2$ scaling is valid. One very important feature to note here is that in addition to the fact that both our work and the work of Lencioni[30] verifies the $1/\lambda^2$ scaling, pulse length scaling information can be obtained as well. Once again, then, we have indication that the breakdown threshold versus pulse length curves are similar for both 1.06µ and 10.6µ with the appropriate wavelength scaling included.

Also in Figure 21, we have included for completeness (and to give some credibility for extending the constant energy curve to 10 picosec) the results of two recent works. First of all, the work of Ireland, et al.[31] at 20 psec is in excellent agreement with the 1000 j/cm^2 extrapolation. The work of McPherson and Gravel[32] at 3 nsec is slightly lower than the 1000 j/cm^2 curve. This small discrepancy is easily explainable, however. McPherson and Gravel conducted their experiments with a mode locked CO_2 TEA laser. The breakdown did not occur until the 5th or 6th pulse in the train. They maintain that there is evidence that the first pulses of the train,

67

while not causing visible breakdown, may have caused some pre-ionization of the air in the focal region thus lowering the threshold.

Finally, in Figure 22, the results presented in Figure 21 are plotted as breakdown threshold as a function of particle diameter. Again, we scale the 10.6µ results by a factor of 100 (corresponding to the 30 nsec pulse width) which are shown as the dashed curve.

In summary, we can draw the following conclusions from our work:

(1) There is a particle size effect on lowering the breakdown threshold for particles between 1µ (estimated size of the impurities present in the filtered air experiments) and 68µ. The smaller particles require a larger investment of energy since the rapid hydrodynamic expansion for the smaller particles imposes greater energy loss mechanisms. The larger particles expand more slowly and represent a smaller loss.

(2) At least for the two materials which we have measured, there is an independence on material composition of the fibers.

(3) For 1 atm ambient pressure, we could furthermore make no distinction between air and argon as the background gas.

(4) The breakdown phenomena are similar at both 1.06µ and 10.6µ and scale as $1/\lambda^2$ indicating that inverse bremsstrahlung is the dominant absorption mechanism.

(5) Comparison of our results with those of Lencioni[30] McPherson and Gravel[32] and with Ireland, et al.[31], indicate that pulse length scaling is similar at both 1.06µ and 10.6µ.

(6) According to the scaling arguments, particulate matter should have no effect on pulsed propagation for pulse lengths less than 1 nsec at both 1.06µ and 10.6µ.
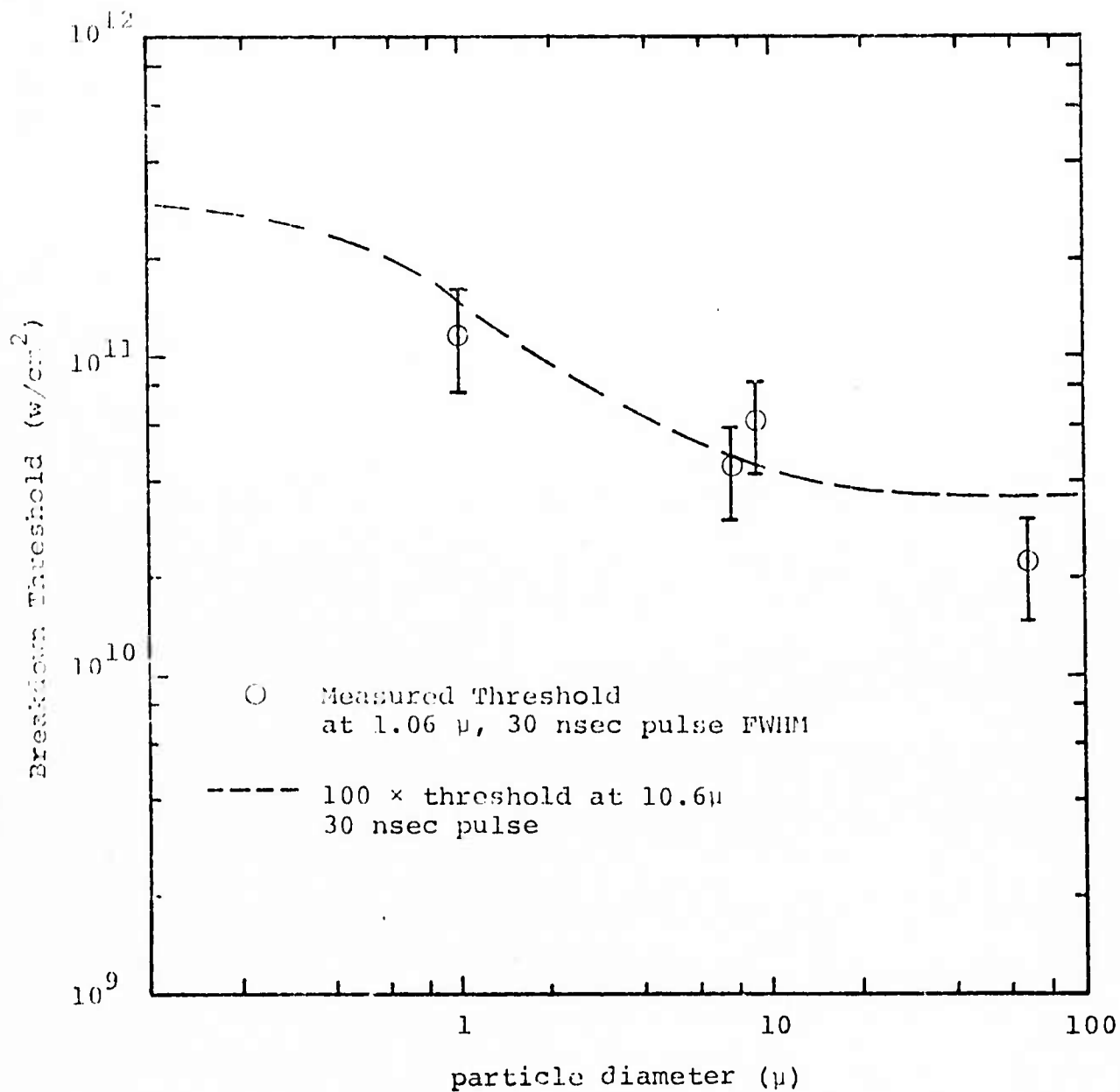
Figure 22. A plot of breakdown threshold versus particle
diameter. The point at 1μ is an estimate from
the filtered air experiments.

In addition to these conclusions regarding the phenome-
nology, one can conclude that simultaneous measurement of pulse
transmission and plasma emission produces an accurate means
for determining the breakdown threshold of gaseous as well as
particle-laden atmospheres.

APPENDIX A

DETAILS OF THE METHOD OF QUASILINEARIZATION
FOR APPLICATION TO THE LSC PROBLEM

A.1 DERIVATION OF EQUATIONS

The theoretical basis underlying the method of quasi-linearization has been presented in Section 2.4. The governing differential equation to which the method is to be applied is Equation (22a). For simplicity, we define $\lambda \equiv \lambda_c + \lambda_r$ and $j = j_c + j_r$. Thus, Equation (22a) can be written as

$$H\left(\frac{dT}{dx}, T\right) \equiv \frac{d^2T}{dx^2} = \frac{-1}{\lambda}\frac{d\lambda}{dT}\left(\frac{dT}{dx}\right)^2 + \frac{\rho_o v_o}{\lambda}\frac{dh}{dT}\frac{dT}{dx} - \frac{k_L\phi - j}{\lambda} \ , \quad (A-1)$$

over the domain

$$-\infty \leq x \leq \infty \qquad .$$

Equation (A-1) is a second order equation (or equivalently two first order equations); however, we can apply the method of quasi-linearization (Equation 22) without separating Equation (A-1) into two first order equations; viz,

$$\frac{d^2T^{k+1}}{dx^2} = \frac{dH^k}{d\left(\frac{dT}{dx}\right)}\ \frac{dT^{k+1}}{dx} - \frac{dT^k}{dx}$$

$$\quad + \frac{dH^k}{dT}\left(T^{k+1} - T^k\right) + H^k \qquad . \tag{A-2}$$

In order to simplify the notation, we define

$$p = \frac{dH}{d\left(\frac{dT}{dx}\right)} = \frac{\rho_o v_o}{\lambda}\frac{dh}{dT} - 2\frac{1}{\lambda}\frac{d\lambda}{dT}\frac{dT}{dx}$$

71

$$r = \frac{dH}{dT} = \left[\frac{d^2h}{dT^2} - \frac{1}{\lambda}\frac{dh}{dT}\frac{d\lambda}{dT}\right]\frac{\rho_o v_o}{\lambda}\frac{dT}{dx}$$

$$- \left[\frac{1}{\lambda}\frac{d^2\lambda}{dT^2} - \frac{1}{\lambda^2}\frac{d\lambda}{dT}\right]^2 - \frac{1}{\lambda}\frac{d}{dT}\left(\frac{k_L\phi - j}{\lambda}\right) \qquad (A-4)$$

$$+ \frac{k_L\phi - j}{\lambda^2}\frac{d\lambda}{dT} \qquad .$$

Then for the (k+1)st iteration, Equation (A-2) can be written as a linear second order differential equation

$$\frac{d^2T^{k+1}}{dx^2} - p^k\frac{dT^{k+1}}{dx} - r^k T^{k+1} + s^k = 0 \qquad (A-5)$$

$$-\infty < x < \infty$$

where

$$s^k = p^k\frac{dT^k}{dx} + r^k T^k - H^k \qquad . \qquad (A-6)$$

Equation (A-5) should be integrated and the boundary conditions 4, 5 and 6 applied at the far upstream ($x = -\infty$) and downstream ($x = \infty$) boundaries. In order to satisfy the boundary condition at both ends, we first integrate Equation (A-5) from $x = 0$ to $-\infty$ and then from 0 to ∞, where the temperature (T_{in}) of the wave at $x = 0$ is arbitrarily chosen (in many cases it can be chosen as the ignition temperature). Then the wave velocity will be determined by matching the slopes of the function at the matching point, $x = 0$.

In the upstream portion ($0 < x < -\infty$), Equation (A-1) can be transformed as

72

$$H = \frac{d^2T}{dx'^2} = \frac{1}{\lambda} \frac{d\lambda}{dT} \left(\frac{dT}{dx'}\right)^2 - \frac{\rho_o v_o}{\lambda} \frac{dh}{dT} \frac{dT}{dx'} - \frac{k_c \psi - j}{\lambda}$$

$$0 < x' < \infty \quad ,$$

where $x' = -x$. Obviously, by comparison, Equation (A-1) can be used for both regions with negative velocity $(-v_o)$ for the upstream portion and positive velocity (v_o) for the downstream portion. Then Equation (A-5) is valid from $-\infty \leq x \leq \infty$, with the appropriate velocity for each region,

$$\frac{d^2T}{dx^2} - p \frac{dT}{dx} - rT + s = 0 \tag{A-7}$$

$$0 \leq x \leq \infty$$

where superscripts k and (k+1) have been omitted for convenience.

To apply the method of quasilinearization, it is required that a particular solution of Equation (A-7) be integrated from $x = 0$ to ∞ with the initial condition

$$T_p = 0, \quad q_p = \frac{dT_p}{dx} = 0 \quad \text{at} \quad x = 0 \quad .$$

Then two homogeneous solutions of the homogeneous equation

$$\frac{d^2T}{dx^2} - p \frac{dT}{dx} - rT = 0 \tag{A-8}$$

are obtained with the following two sets of initial conditions

1. $T_c = 1; \quad q_c = 0 \quad \text{at} \quad x = 0$

2. $T_d = 0; \quad q_d = 1 \quad \text{at} \quad x = 0 \quad .$

73

By virtue of the properties of a linear equation, the total solution should be

$$T = T_p + C_1 T_c + C_2 T_d \tag{A-9}$$

$$q = \frac{dT}{dx} = q_p + C_1 q_c + C_2 q_d \quad . \tag{A-10}$$

Now we can apply the two point boundary conditions to deter-mine the two constants, C_1 and C_2. Applying boundary condi-tion $T = T_{in}$ at $x = 0$ to Equation (A-9) gives $C_1 = T_{in}$, and applying boundary condition $q = \frac{dT}{dx} = 0$ at $x = \infty$ determines C_2 as

$$C_2 = -\frac{q_p(\infty) + T_{in} q_c(\infty)}{q_d(\infty)}$$

Once $dT/dx = 0$ at $x = -\infty$ is satisfied, the other boundary con-dition, $T = T_o$ at $x = -\infty$, is automatically satisfied by Equa-tion (22). In practice, instead of integrating Equation (A-5) to infinity, one integrates to a large x where $\frac{dT}{dx}$ approaches zero.

Since the method of quasilinearization is an iterative scheme, an initial trial solution is guessed, then $p^k(x)$, $r^k(x)$ and $s^k(x)$ are calculated according to Equations 24, 25 and 27. Due to the drastic changes at the wave front, it is found that the integration of Equation (A-5) in x can be best performed by the following simple method. First, we divide the x coordinate from 0 to x_∞ into many intervals with dif-ferent spacing h. The value of h depends upon the changes of $p(x)$, $r(x)$ and $s(x)$ with respect to x. If h is small enough p, r and s can be considered as constants in each inter-val. Then Equation (A-5) becomes a second order linear dif-ferential equation with constant coefficients over each inter-val

$$\frac{d^2 T_{i+1}}{dx} - p(x_i) \frac{dT_{i+1}}{dx} - r(x_i) T_{i+1} + s(x_i) = 0 \quad . \quad (A-12)$$

The solutions of the above equations are straightforward and depend on the values of $p(x_i)$ and $r(x_i)$. The solutions are

$$T(x_{i+1}) = A e^{\alpha_1 h} + B e^{\alpha_2 h} + \frac{s(x_i)}{r(x_i)} \quad ,$$

where

$$A = \left[-\frac{dT_i}{dx} + \alpha_2 T_i - \frac{\alpha_2 s(x_i)}{r(x_i)} \right] \Big/ (\alpha_2 - \alpha_1) \quad ,$$

$$B = \left[\frac{dT_i}{dx} - \alpha_1 T_i + \frac{\alpha_1 s(x_i)}{r(x_i)} \right] \Big/ (\alpha_2 - \alpha_1)$$

and

$$\begin{Bmatrix} \alpha_1 \\ \alpha_2 \end{Bmatrix} = \frac{1}{2} \left[P(x_i) \pm \sqrt{P(x_i)^2 + 4r(x_i)} \right] \quad .$$

(A-13)

For $P(x_i)^2 + 4r(x_i) \geq 0$; and,

$$T(x_{i+1}) = e^{\alpha h} (A \cos \beta h + B \sin \beta h) + \frac{s(x_i)}{r(x_i)} \quad ,$$

where

$$A = T_i - s(x_i)/r(x_i) \quad ,$$

(A-14)

$$B = \frac{1}{\beta} \left\{ \frac{dT_i}{dx} - \alpha \left[T_i - \frac{s(x_i)}{r(x_i)} \right] \right\} \quad ,$$

$$\alpha = \frac{1}{2} p(x_i) \quad ,$$

and

$$\beta = \frac{1}{2} \sqrt{\left[p(x_i)^2 + 4r(x_i) \right]}$$

for $p(x_i)^2 + 4r(x_i) < 0$. For the homogeneous equation (A-8b), the above solutions are valid with $s(x_i) = 0$. After each integration with respect to x, all $T_p(x_i)$, $q_p(x_i)$, $T_c(x_i)$, $q_c(x_i)$, $T_d(x_i)$ and $q_d(x_i)$ values are stored. Then the constants C_1 and C_2 are determined from Equation (A-11). Finally the value of $T^{k+1}(x_i)$ and $q^{k+1}(x_i)$ are calculated according to Equations (A-9) and (A-10) and they are ready to be substituted into Equations (A-4) (A-5) and (A-6) to calculate the functions p, r and s. The iterative procedure continues until a convergence criterion is reached for the constant C_2 in two successive iterations.

A.2   METHOD OF SEGMENTATION

The principal numerical difficulty involved in solving a two point boundary value problem, especially where the "other" boundary condition has to be satisfied at a large value of x_∞ (or at infinity) is numerical "overflow" of the computer during the process of integration. For example, consider the following equation:

$$\frac{d^2y}{dx^2} - P \frac{dy}{dx} - R + S = 0 \qquad (A-15)$$

with boundary conditions specified as

$$y = y_0 \quad \text{at} \quad x = 0 \qquad (A-16)$$

$$\frac{dy}{dx} = 0 \quad \text{at} \quad x = \infty \quad . \qquad (A-17)$$

The quantities P, R and S are all positive constants. Assume $(P^2 - 4R)$ is positive, then the solution of Equation (A-15) is

$$y = Ae^{\alpha_1 x} + Be^{\alpha_2 x} + S/R \qquad (A-18)$$

76

where

$$\begin{Bmatrix} \alpha_1 \\ \alpha_2 \end{Bmatrix} = \frac{1}{2} \left[P \pm \sqrt{P^2 - 4R} \right] \quad .$$

Obviously, α_1 is a postive constant, whereas α_2 is negative. After applying the boundary condition at $x = \infty$, the constant A is set to zero, and the exponentially growing term $e^{\alpha_1 x}$ will not effect the solution. However, this procedure does not apply for a numerical integration. Due to the fact that the boundary condition at $x = \infty$ (or $x = x_\infty$) will not be applied until after the numerical integration from 0 to x_∞ is finished, obviously, the positive α_1 will cause the integration to be terminated whenever the term $e^{\alpha_1 x}$ is larger than the upper limit of the computer. Hence the integration cannot be continued and the problem cannot be solved. This is a very well known problem in numerical integration.

In dealing with this problem, we propose that the following procedure be applied to the method of quasilinearization. First, we divide the entire integration path into n segments which are chosen such that within each segment, the term $e^{\alpha_1 (x_{i+1} - x_i)}$ is well under the upper limit of the computer. Then, two homogeneous solutions and one particular solution can be obtained for each segment with the method described above. The total solutions in each segment are:

$$T_i = T_{ip} + C_{2i-1} T_{ic} + C_{2i} T_{id}$$

$$i = 1, 2, \cdots n$$

$$q_i = q_{ip} + C_{2i-1} q_{ic} + C_{2i} q_{id} \tag{A-19}$$

77

with initial conditions

$$T_{ip}(x_{i-1}) = 0 \quad ; \quad q_{ip}(x_{i-1}) = 0$$

$$T_{ic}(x_{i-1}) = 1 \quad ; \quad q_{ic}(x_{i-1}) = 0 \quad i = 1,2,\cdots n \qquad (A-20)$$

$$T_{id}(x_{i-1}) = 0 \quad ; \quad q_{id}(x_{i-1}) = 1 \qquad .$$

After each segment has been evaluated, the two point boundary conditions can be applied to the systems, i.e.,

$$T_1(x_o) = T_1(0) = T_{in}$$

$$q_n(x_n) = q_n(x_\infty) = 0 \qquad . \tag{A-21}$$

At the same time, matching conditions are also applied at each joint of every segment;

$$T_i(x_i) = T_{i+1}(x_i)$$

$$i = 1,2,\cdots n-1 \tag{A-22}$$

$$q_i(x_i) = q_{i+1}(x_i) \qquad .$$

Therefore there will be 2n constants C_1, $C_2 \cdots C_{2n}$ to be determined by the above 2n algebraic equations. With some simple manipulation, Equations (A-21) and (A-22) can be written as

$$C_1 = T_{in} \tag{A-23}$$

78

$$
\begin{bmatrix}
(B_2-1) & & & & & & & \\
A_3(B_3-1) & & & & & & & \\
& A_4(B_4-1) & & & & & & \\
& & ----- & & & & & \\
& & & ----- & & & & \\
& & & & A_{2n-2}(B_{2n-2}-1) & & & \\
& & & & & A_{2n-1}(B_{2n-1}-1) & & \\
& & & & & & A_{2n} & B_{2n}
\end{bmatrix}
\begin{bmatrix}
C_2 \\
C_3 \\
C_4 \\
\vdots \\
\vdots \\
C_{2n-2} \\
C_{2n-1} \\
C_{2n}
\end{bmatrix}
=
\begin{bmatrix}
D_2-A_2C_1 \\
D_3 \\
D_4 \\
\vdots \\
\vdots \\
D_{2n-2} \\
D_{2n-1} \\
D_{2n}+C_{2n+1}
\end{bmatrix}
\; ,
$$

$$(A-24)$$

where

$$A_{2i} = T_{ic}(x_i)$$

$$A_{2i+1} = q_{id}(x_i) - T_{id}(x_i)\frac{q_{ic}(x_i)}{T_{ic}(x_i)}$$

$$B_{2i} = T_{id}(x_i) \qquad\qquad i = 1,2,\cdots n$$

$$B_{2i+1} = \frac{q_{ic}(x_i)}{T_{ic}(x_i)}$$

$$D_{2i} = T_{ip}(x_i)$$

$$D_{2i+1} = -q_{ip}(x_i) + T_{ip}(x_i)\frac{q_{ic}(x_i)}{T_{ic}(x_i)} \qquad .$$

Since Equation (A-24) is a tridiagonal system, it can be solved
simply and efficiently by the following method.[17]

The basic formula in Equation (A-24) can be written as

$$A_m C_{m-1} + B_m C_m - C_{m+1} = D_m \ . \quad 2 \le m \le 2n \qquad (A-25)$$

Now, let us assume a solution of C_m has the form as

$$C_m = w_m C_{m+1} + g_m \quad , \qquad (A-26a)$$

or, for C_{m-1},

$$C_{m-1} = w_{m-1} C_m + g_{m-1} \quad . \qquad (A26b)$$

Eliminating C_{m-1} between Eqs. (A-26a) and (A-26b) gives

$$C_m = \frac{1}{A_m w_{m-1} + B_m} C_{m+1} + \frac{D_m - A_m g_{m-1}}{A_m w_{m-1} + B_m} \quad . \qquad (A-27)$$

Obviously the w_m and g_m are

$$w_m = \frac{1}{A_m w_{m-1} + B_m} \qquad (A-28a)$$

$$g_m = \frac{D_m - A_m g_{m-1}}{A_m w_{m-1} + B_m} \quad . \qquad (A-28b)$$

To start the calculation procedure one first observes that

$$C_1 = w_1 C_2 + g_1 \quad .$$

However since from Equation (A-23), we know that

$$C_1 = T_{in} \quad .$$

80

It is apparent that

$$w_1 = 0 \quad \text{and} \quad g_1 = T_{in} \quad . \tag{A-29}$$

Then all the w's and g's can be calculated easily provided that

$$\frac{1}{A_n w_{m-1} + B_m} < 1 \quad .$$

With the definition of A_n and B_m, we can show that the above criterion is always satisfied. Once all w's and g's are known, it is simple to compute all constant C_n's according to Eq. (A-26a) with $C_{2n+1} = 0$.

To demonstrate the above method we choose to solve the following nonlinear second order ordinary differential equation

$$\frac{d^2 y}{dx^2} = (a - 2y) \frac{dy}{dx} - b + ay^2 \quad , \tag{A-30}$$

with boundary conditions

$$y = y_0 \quad \text{at} \quad x = 0$$

$$\frac{dy}{dx} = 0 \quad , \text{at} \quad x = \infty$$

where a and b are positive constants. This equation can be solved exactly[18] by defining a new dependent variable u as

$$u = \frac{dy}{dx} + y^2 \quad . \tag{A-31}$$

Then Equation (A-29) can be written as

$$\frac{du}{dx} - au = -b \quad . \tag{A-32}$$

81

Integration of Equation (A-31) gives

$$u = c_1 e^{ax} + b/a \quad ,$$

or

$$\frac{dy}{dx} = C_1 e^{ax} + \frac{b}{a} - y^2 \quad . \tag{A-33}$$

Due to the boundary condition at infinity, C_1 is zero. Therefore the exponential growing term e^{ax} is eliminated. Integration once more of Equation (A-33) gives

$$y = \sqrt{\frac{b}{a}} \tanh \left(C + \sqrt{\frac{b}{a}} \, x \right) \quad .$$

After applying the initial condition the final solution is

$$y = \sqrt{\frac{b}{a}} \; \frac{\sqrt{\frac{a}{b}} \, y_0 + \tanh \sqrt{\frac{b}{a}} \, x}{1 + \sqrt{\frac{a}{b}} \, y_0 \tanh \sqrt{\frac{b}{a}} \, x} \quad . \tag{A-34}$$

We plot the above solution for the case where $a = 10$, $b = 40$ and $y_0 = 1$ in Figure A-1. Also shown is the first few iterations of the numerical solution by using the method of quasi-linearization. Notice that since $a = 10$, the exponentially growing factor is e^{10x}. Therefore in the numerical calculation the total integration path (from 0.0 to 10.0) has to be divided into 5 to 8 segments (the number of segments is determined automatically by the computer program whenever the value of integration exceeds a prescribed limit). Without segmentation, the integration can only proceed to about $x = 1.5$ without an "overflow". However, as one can see from Figure A-1, the slope of the first integration will not approach zero unless the integration is carried beyond $x = 6.0$.
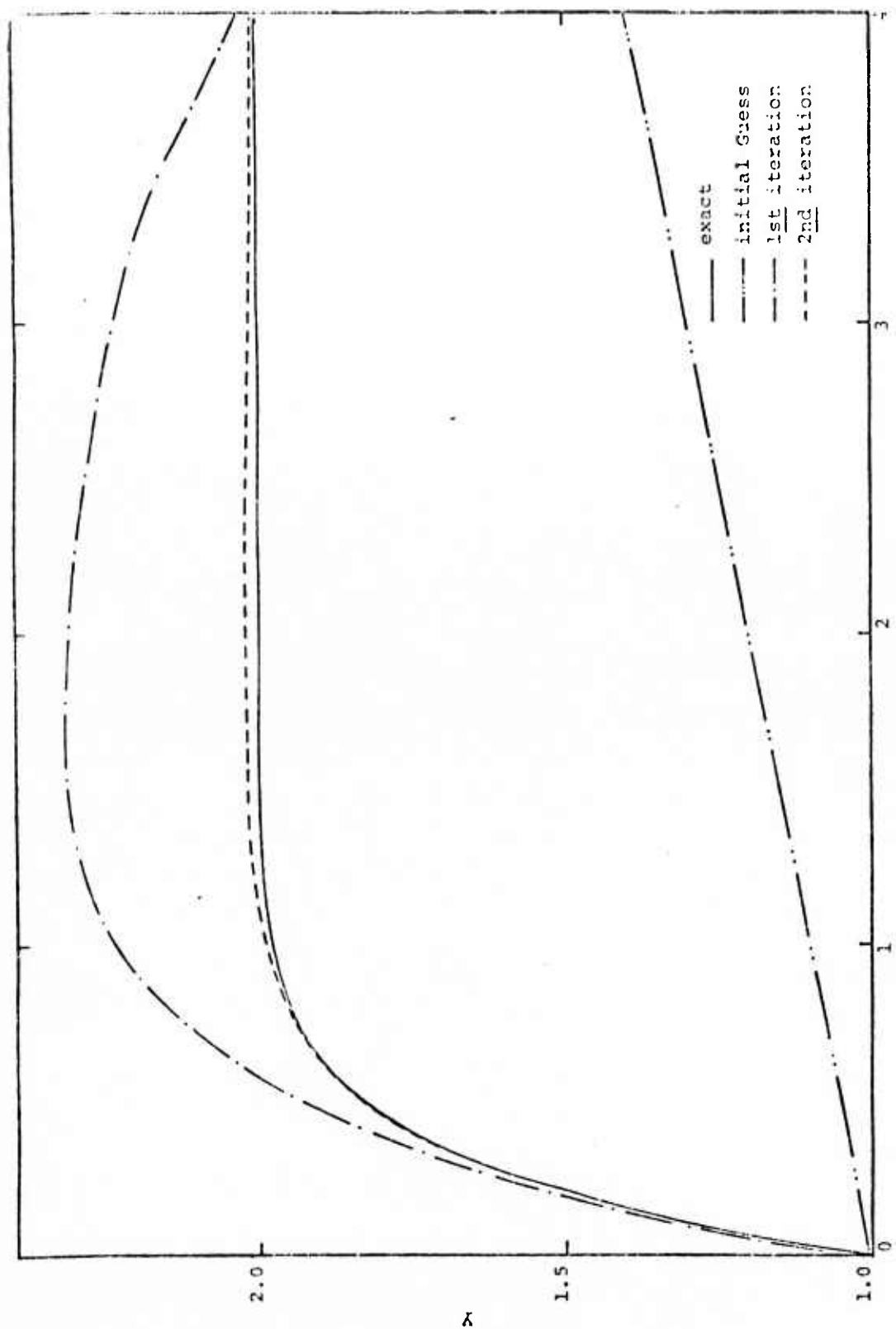
82

Figure A.1 Comparison between exact solution and numerical solution by method of quasilinearization for a sample problem.

83

Therefore the method of segmentation is very important in applying the method of quasilinearization to some nonlinear equations. Also it is shown in Figure A-1 that in general the method of quasilinearization is a powerful method. With an un-inspired guessing of the initial trial function, after only three iterations, the numerical solution coincides with the exact solution to within a half of one percent.

A.3   NUMERICAL METHOD

Because of the highly nonlinear coefficients in Equation (A-2) (see Section 2.3), certain precautions must be taken before routinely applying the method of quasilinearization. Since an iterative procedure is used, the intermediate solution will either overshoot or undershoot the exact solution. It is found that excessive overshoot or undershoot will cause a termination of the numerical scheme. With a large value of temperature (T_i), λ can cause "overflow" because of the exponential fitting of λ, Equation (14). On the other hand, a negative T_i (although it is physically meaningless, it can occur in an intermediate stage of an iteration scheme) will stop the calculation due to the undefined operation of raising a negative number to a partial power, such as the calculation in Equation (9). To avoid these problems, the calculated temperatures are forced to exist in the range of $10 \leq T_i/10^4 \leq 0$. At the same time, special care must be exercised on the initial trial function. Another problem which existed in the iterative procedure is the zoning problem. It is found that in the iterative process, the slope of the temperature, dT_i/dx, can change violently from one iteration to another before it approaches the final solution. Due to this change, the values of α (Equation (A-13) and (A-14)) will become exceedingly large such that the integration of q_i or T_i is terminated due to "overflow"
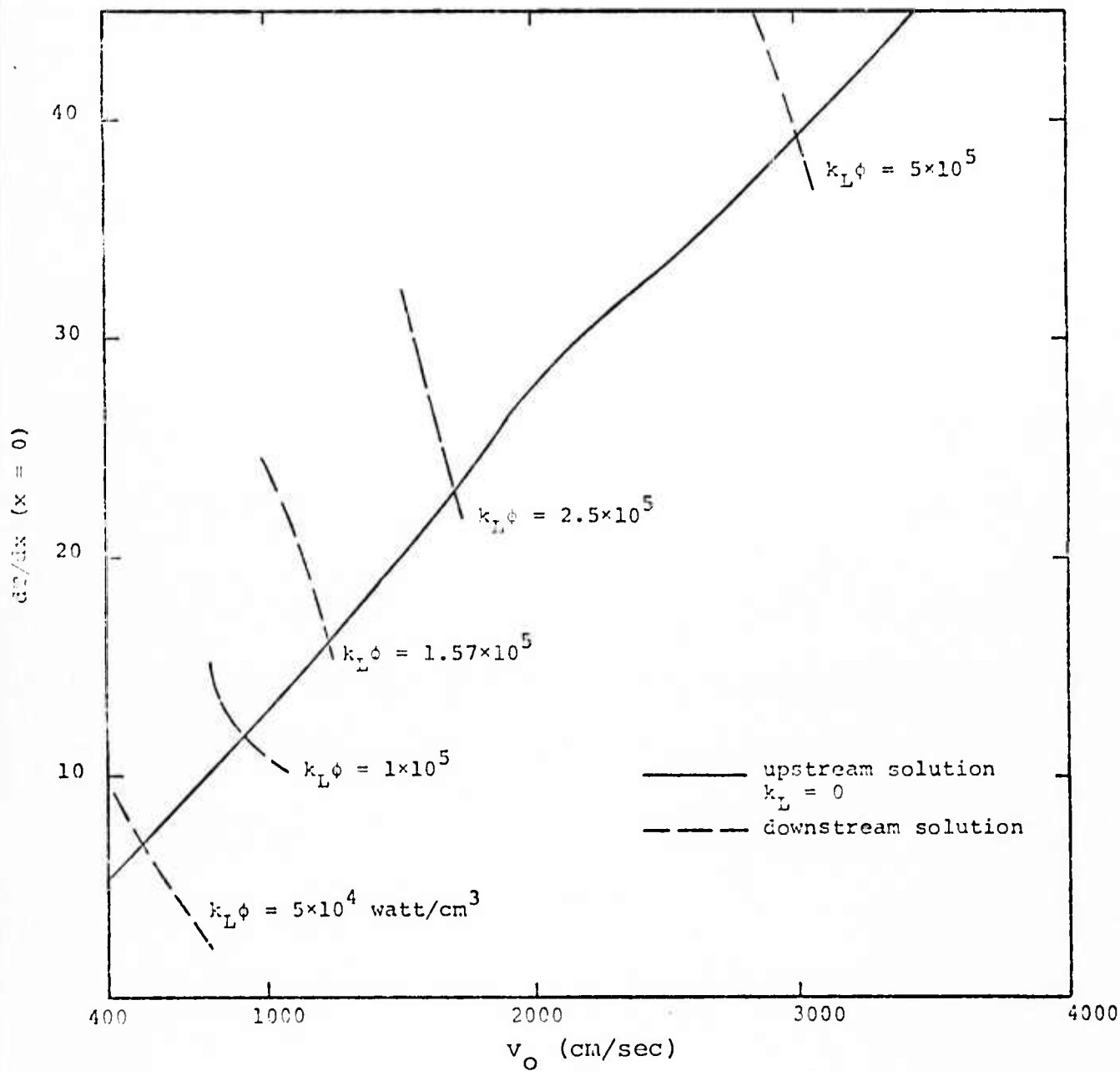
Figure A.2   Eigenvalue velocity v_0 determined by graphical matching of the stop at x_0 for cases where $j_c = 0$.

within one integration step (this can not be helped by the
method of segmentation, since a segment consists of more than
one step). Therefore a rezone capability is built in the
numerical program to reduce the size of the integration step
to continue the integration.

As we mentioned before, because of the above numerical
difficulties, the initial trial function must be carefully
selected in order to assure a fast convergent solution. To
demonstrate the method of selection of the initial trial
function, we will describe the procedure to obtain a solution
for the case of Bunkins[1] experiment. A neodynium laser is
incident on air with spot size $R \simeq 0.125$ cm and the absorbed
flux of $k_L \phi \simeq 1.57 \times 10^6$ watts/cm^3.[6] To obtain a solution,
we have to construct the initial trial function from a
simpler situation where the solution can be easily obtained.
Let us rewrite the correlation function of λ; Equation (14)
as

$$\lambda = 2.2 \times 10^8 \ e^{a(T/10^4 - 1.75)} \qquad T \leq 17500 \ °K$$

$$\tag{A.35}$$

$$= 2.2 \times 10^8 \ e^{3(T/10^4 - 1.75)} \quad , \ T > 17500 \ °K$$

where a = 6.4. The first step consists of using an arbitrarily
chosen exponential function as the initial function for tem-
perature to solve the case where $k_L \phi = 1.57 \times 10^6$, a = 3 and
neglecting the conductive energy loss, i.e., $j_c = 0$ (or R
equal to a large number, for example $R = 12.5$ in Equation (3))
with a given velocity v_o. In general, it takes about eight
to twelve iterations to obtain a solution with less than one
percent of error in two consecutive iterations. Then by
using the final solution of the above case (a = 3, $R = 12.5$)
as the initial trial function we can obtain a solution within
two to eight iterations for the case where a = 3, R = 5. By
the same method, we then proceed to compute solutions for

cases where $a = 3$, $R = 1.25$; $a = 3$, $R = 5$; $a = 3$, $R = .25$; $a = 3$, $R = .125$; $A = 5$, $R = .125$; $a = 6$, $R = .125$; and finally, for Bunkin's case where $a = 6.4$ and $R = .125$. Usually Usually two to four iterations are needed for each case, except when the iterated solutions oscillate between two limits with a very slow convergence. Then an average method is used and usually it takes about four to eight iterations to converge to a final solution. Instead of using the ith iterated solution (T_i) as the trial solution for $(i+1)$th iteration, an average method using $(T_i + T_{i-1})/2$ as the trial solution for T_{i+1} is utilized in order to expedite the convergence process. Each iteration takes about four seconds of computation time on the UNIVAC 1108.

As we described in Section 2.2, the LSC propagation problem is an eigenvalue problem. The propagation velocity must be determined by matching the upstream and downstream solutions at $x = 0$. All of the above described numerical methods can be applied to either the upstream solution (negative v_o) or to the downstream solution (positive v_o) with a given velocity. Then by varying the velocity, the gradient of the temperature at $x = 0$ will change accordingly. Finally, a graphical matching (Figure A-2) (or a numerical matching on the computer) of the slope of the upstream and downstream temperature profile determines the propagation velocity. With the velocity known, we then calculate the matching temperature profile of a propagating LSC wave.

APPENDIX B

USER'S GUIDE TO PROGRAM TEMP

TEMP is programmed in FORTRAN IV and run on the UNIVAC 1108. It is a double precision program. This program is designed to solve the temperature profile of a one-dimensional steady state laser supported combustion wave. The numerical method used in this program is the method of quasilinearization with the method of segmentation (see Appendix A). TEMP calculates the downstream temperature profile as well as the upstream temperature profile depending on the sign of the given velocity. For a positive velocity the downstream temperature profile will be computed whereas a negative velocity will give the upstream profile. In order to obtain rapid convergence, usually the initial function for any iteration is the final solution of iteration (see Appendix A). Therefore a tape is required to store the final solution for each case.

In the following paragraphs, we first define the input variables and output variables. Then a typical run with input and output will be displayed. Finally a listing of TEMP will be included.

INPUT VARIABLES

MSTART   an integer switch.
  0; the initial function is arbitrarily set in the program
  1; the initial function is read from the tape.

JBLOCK   an integer number
  When MSTART = 1, the initial function will be read from "JBLOCK" th block in the tape.

TIN   a double precision number.

     The ignition temperature or a starting temperature at $x = 0$ in 10^4 °K, usually TIN = 1.2.

RHO   a double precision number.

     The density of air at far upstream. RHO = 1.18×10^{-3} g/cm^3.

U   a double precision number.

     The given propagation velocity (cm/sec)

     U > 0; downstream temperature profile is calculated.

     U < 0; upstream temperature profile is calculated.

AX   a double precision number.

     Exponent of correlation formula of λ (Eq.

FLUX   a double precision number.

     The quantity $k\phi_o$ (erg/cm^3 sec)

RADIUS   a double precision number.

     The radius of incident laser beam (cm).

EPS   a double precision number.

     Convergent criterion

OUTPUT VARIABLES

     All variables are in double precision, except K.

K2   Constant C_2

KOLD   Constant C_2 in previous iteration

X   X coordinate (cm)

TP   Particular solution, T_p

QP   Particular solution, q_p

TC   Homogeneous solution, T_c

QC   Homogeneous solution, q_c

T   Temperature (10^4 °K)

DT   Temperature gradient (10^4 °K/cm)

P   Function $p(T, dT/dx)$

R   Function $r(T, dT/dx)$

S   Function $s(T, dT/dx)$

E1   E1 = α_1,   when   k = 0
            E1 = α,   when   k = 1

E2   E2 = α_2,   when   k = 0
            E2 = β,   when   k = 1

K   An integer switch
            K = 0, exponential type solution
            K = 1, sinusoidal type solution

Table A.1 shows a typical input data of TEMP. Notice
that the initial trial function is read from the 9th block
in the tape (see Section 6 for detail of numerical calcula-
tion). Table A.2 shows the output of the calculation for the
input data shown in Table A.1.

TABLE B.1

TYPICAL INPUT DATA FOR TEMP

```
$INPUT
MSTART    =           +1
JBLOCK    =           +9
TIN       =           .120000000000000000000+001
RHO       =           .130000000000000000-002
U         =           .160000000000000000+004
AX        =           .339999999999999990+001
FLUX      =           .100000000000000000+012
RADIUS    =           .150000000000000000+000
EPS       =           .100000000000000000-001

$END
```

TABLE 3.2

TYPICAL OUTPUT DATA FOR TEMP

AVERAGE CONVERGENT METHOD IS USED

K2= 1.2000+000   7.3765+001
K2= 7.3765+001 KOLD = 9.7799+001 PHI=

AVERAGE CONVERGENT METHOD IS USED

K2= 1.2000+000   9.0310+001
K2= 9.0310+001 KOLD = 7.3765+001 PHI=

AVERAGE CONVERGENT METHOD IS USED

K2= 1.2000+000   9.0376+001
K2= 9.0376+001 KOLD = 9.0310+001 PHI=
IT CONVERGES

X	TP	QP	TC	QC	T	DT	P	R	S	E1	E2	K
.0005	.0000	.0000	.1000+001	.0000	.1200+001	.0921+002	-.1092+004	-.1669+005	-.6956+005	-.1550+02	-.1076+04	0
.2000-005	.1389-006	.1388+000	.1000+001	-.3331-001	.1200+001	.8912+002	-.1091+004	-.1665+005	-.6942+005	-.1549+02	-.1075+04	0
.4000-005	.5550-006	.2771+000	.1000+001	-.6647-001	.1200+001	.8902+002	-.1090+004	-.1662+005	-.6928+005	-.1547+02	-.1074+04	0
.6000-005	.1247-005	.4148+000	.1000+001	-.9950-031	.1201+001	.8943+002	-.1089+004	-.1659+005	-.6914+005	-.1546+02	-.1073+04	0
.8000-005	.2214-005	.5519+000	.1000+001	-.1324+000	.1201+001	.8883+002	-.1087+004	-.1655+005	-.6901+005	-.1544+0.	-.1072+04	0

94

TABLE B.3

LISTING OF TEMP

```
FOR,IS TEMP,TEMP

C     THIS CODE USES A QUASI-LINEARIZATION TECHNIQUE TO COMPUTE TEMPERATURE

      IMPLICIT DOUBLE PRECISION (A-H, O-Z)
      DOUBLE PRECISION LAMDAC,LAMDAR
      REAL IE1, IE2
      COMMON/AAX/AX
      PARAMETER KP=50, KP2=100, IP=1201, IN=10,100=3603
      COMMON DADT,DBDT,D2ADT,D2BDT,DCDT,B,C
     1,LAMDAC, LAMDAR, DLCDT,DLRDT,D2LCDT,D2LRDT,PHI,DKLDT,DPDT,AJ,AJC,
     2DJDT,DJCDT
      COMMON/TDT/XX(IP),TE(IP),DTDX(IP)
      COMMON /SUMKL/ FC(IP),GC(IP),HC(IP),SKL(IP),FKL(IP),IT,TO,FLUX,AL(
     1IP),RADIUS
      COMMON /FCNS/ P(IP),R(IP),S(IP),IM
      DIMENSION IKL(KP),TP1(KP),TC1(KP),WC1(KP),QP1(KP),CON(KP2),A(KP2),
     1AB(KP2),D(KP2),AS(KP2),W(KP2),TD1(KP),WD1(KP)
      DIMENSION IE1(IP), IE2(IP), IE(IP),WD(IP),TJ(IP)
      DIMENSION PC(IP),TC(IP),QP(IP),TP(IP),W(100)
      DIMENSION HH(14), NN(IN)
      DATA NN/1,51,101,151,301,401,601,801,1001,1201/
      DATA HH/0.D0,2.D-7,2.D-6,2.D-5, 1.D-4,1.D-3,1.D-2,2.5D-2,5.D-2,1.D
     1-1/
      DIMENSION CK(100)
      EQUIVALENCE (G(1),AX(1))
      NAMELIST/INPUT/MSTART,TIN,RHO,U,JBLOCK,AX,RADIUS,FLUX,EPS
      IG=LOC(DTDX(IP))-LOC(XX(1))+2
      KP1=KP-1
      KPM=KP-2
      IPP=IP
      DO 87 J=1, KP2
   87 CON(J)=1.
   21 READ(5,INPUT,END=100)
      WRITE (6,INPUT)
      KCC=0
      IAV=0
      NC=0
      G= RHO*U
C     IF (MSTART .EQ. 1) GO TO 22
C     ASSUME THE TEMPERATURE VARIES LINEARLY FROM  0000.DEGK TO 1000.DEGK
      X=-HH(2)
      M=1
      IF(U)220,221,221
  220 TTIN=TIN-.03
      DTIN=TTIN*100.
      TTJN=0.
      EXTX=100.
      GO TO 222
  221 TTIN=2.-TIN
      DTIN=20.*TTIN
      TTIN=-TTIN
```

```
      TTJN=2.
      EXTX=5.
222   DO 7 J=2,IN
      H=HH(J)
      N=JN(J)
      DO 5 I=M,N
      X=X+H
      XX(I)=X
191   EX=EAP(-EXTX*X)
      TE(I)=TTJN/TTIN*EX
      DTDX(I)=DTIN*EX
  5   CONTINUE
  7   M=N
      GO TO 23
 22   CALL NTRAN (11,13)
      DO 24 K=1,JBLOCK
      CALL NTRAN(11,2,IQ,N,LQ,22)
      IF (LQ .NE. IQ) RETURNS
 24   CONTINUE
 23   CONTINUE
      PRINT 1,TE
 3    FORMAT('DTDX = ',/(1H ,1P10E16.4))
 1    FORMAT('T = ',/(1H ,1P10E16.4))
      PRINT 13
C
C     BEGINNING OF ITERATIVE LOOP ON TEMPERATURE
      PRINT 333, CX
333   FORMAT (1H1, 'CX=' D16.4)
      ICT=0
10    CONTINUE
      ICT=ICT+1
      IPE=IPP
      KL=1
      IKL(1)=1
      DO 20 I=1, IP
      IF (TE(I) .LE. 0. .OR. TE(I) .GT. 3.D1) GO TO 88
      GO TO 89
 88   TE(I)=TE(I-1)
 89   CONTINUE
 20   CONTINUE
      TO=.03
C
C     COMPUTE DERIVATIVES DADT,D2ADT,DBDT,D2BDT,DCDT, AND B
      DO 50 I=1,IP
      IT=I
      CALL DERI(TE(I), DTDX(I))
      OB=1./B
      OB2=OB**2
      P(I)=OB*(1.E-4*G*DADT-2.*DBDT*DTDX(I))
      R(I)=DTDX(I)*OB2*(G*(B*D2ADT-DADT*DBDT)*1.E-4-(B*D2BDT-DBDT**2)*DT
     1DX(I))-(DCDT*OB-C*OB2*DBDT)*1.E-4
      S(I)=P(I)*DTDX(I)+R(I)*TE(I)-OB*(1.E-4*G*DADT-DBDT*DTDX(I))*DTDX(I
     1)+C/B*1.E-4
 13   FORMAT (1H0, 'XX, TE, DADT, LAMDAC, DLCDT, D2LCDT, LAMDAR, DLRDT,
```

96

```
      1D2LRDT, B, DBDT, D2BDT'/1X, 'DTDX, FKL, SKL, DKLDT, PHI, DPDT, AJ,
     2 DJDT, AJC, DJCDT, C, DCDT'//)
 171  FORMAT (12(1X, D13.4)/2X, 11(D10.4, 1X), D9.3)
 60   CONTINUE
      INTEGRATE TO OBTAIN DTDX
      X=0.
      XX(1)=0.
      QP(1)=0.
      TP(1)=0.
      QC(1)=0.
      TC(1)=1.
      QD(1)=1.
      TD(1)=0.
      N1=1
      DO 61 M=2, IN
      N=NN(M)-1
      H=HH(M)
      DO 60 I=N1,N
      I1=I+1
      X=X+H
      SR=S(I)/R(I)
      SAL=P(I)**2+4.*R(I)
      IF (SAL) 63,63,64
 63   BETA=.5*SQRT(-SAL)
      AA=.5*P(I)
      IE(I)=1
      IE1(I)=AA
      IE2(I)=BETA
      MKL=MKL+1
      EA=EAP(AA*H)
      BA=BETA*H
      CBA=COS(BA)
      SBA=SIN(BA)
 76   C1=TC(I)
      C2=(QC(I)-AA*C1)/BETA
      D1=TD(I)
      D2=(QD(I)-AA*D1)/BETA
      P1=TP(I)-SR
      P2=(QP(I)-AA*P1)/BETA
      QP(I1)=EA*((AA*P1+BETA*P2)*CBA+(AA*P2-BETA*P1)*SBA)
      IF (ABS(QP(I1)) .GT. 1.D8 ) GO TO 74
 176  TP(I1)=EA*(P1*CBA+P2*SBA)+SR
      QC(I1)=EA*((AA*C1+BETA*C2)*CBA+(AA*C2-BETA*C1)*SBA)
      TC(I1)=EA*(C1*CBA+C2*SBA)
      QD(I1)=EA*((AA*D1+BETA*D2)*CBA+(AA*D2-BETA*D1)*SBA)
      TD(I1)=EA*(D1*CBA+D2*SBA)
 65   FORMAT (1X, 6(1X, D11.4), 13X, D11.4)
      GO TO 60
 64   SAL=SQRT(SAL)
      AL1=.5*(P(I)+SAL)
      AL2=.5*(P(I)-SAL)
      IE(I)=0
      IE1(I)=AL1
```

97

```
      IF2(I)=AL2
      IKL=IKL+1
      A21=AL2-AL1
      AL1H=AL1*H
      EA1=EXP(AL1*H)
      EA2=EXP(AL2*H)
  75  C1=(-QC(I)+AL2*TC(I))/A21
      C2=(QC(I)-AL1*TC(I))/A21
      D1=(-QD(I)+AL2*TD(I))/A21
      D2=(QD(I)-AL1*TD(I))/A21
      P1=(-QP(I)+AL2*TP(I)-AL2*SR)/A21
      P2=(QP(I)-AL1*TP(I)+AL1*SR)/A21
      QP(II)=AL1*P1*EA1+AL2*P2*EA2
      IF (ABS(QP(II)) .GT. 1.D8 ) GO TO 74
 175  TP(II)=P1*EA1+P2*EA2+SR
      QC(II)=AL1*C1*EA1+AL2*C2*EA2
      TC(II)=C1*EA1+C2*EA2
      QD(II)=AL1*D1*EA1+AL2*D2*EA2
      TD(II)=D1*EA1+D2*EA2
  42  FORMAT (1X, 7(1X,D11.4))
  60  CONTINUE
  61  NI=N
  35  IKL(KL+1)=IPE
      TCI(KL)=TC(IPE)
      QCI(KL)=QC(IPE)
      TDI(KL)=TD(IPE)
      QDI(KL)=QD(IPE)
      TPI(KL)=TP(IPE)
      QPI(KL)=QP(IPE)
      KL2=KL*2
      CON(1)=TIN
      CON(KL2+1)=0.
      COMPUTE TEST VALUE K=-QP/QC AND TEST
  73  CONTINUE
      COLD=CON( 2)
      IF (KL .EQ. 1) GO TO 83
      W(1)=0.
      AG(1)=CON(1)
      KL1=KL-1
      DO 201 L=1,KL1
      L1=2*L
      L2=L1+1
      L0=L1-1
      AB(L2)=QCI(L)/TCI(L)
      AB(L1)=TDI(L)
      A(L1)=TCI(L)
      A(L2)=QDI(L)-TDI(L)*AB(L2)
      D(L1)=-TPI(L)
      D(L2)=-QPI(L)+TPI(L)*AB(L2)
      W(L1)=1./(A(L1)*W(L0)+AB(L1))
      W(L2)=1./(A(L2)*W(L1)+AB(L2))
      AG(L1)=(D(L1)-A(L1)*AG(L0))*W(L1)
 201  AG(L2)=(D(L2)-A(L2)*AG(L1))*W(L2)
      W(KL2)=1./(TCI(KL)*W(KL2-1)+QDI(KL))
```

```
      AG(KL2)=(-QP1(KL)-QC1(KL)*AG(KL2-1))*W(KL2)
      DO 202 L=KL2,2,-1
  202 CON(L)=W(L)*CON(L+1)+AG(L)
      GO TO 185
   81 PRINT 11, (CON(JK),JK=1,KL2)
   11 FORMAT (2(3X,1PD12.4))
      PRINT 6 CON( 2),COLD,PHI
    6 FORMAT(' K = ',1PD12.4,' KOLD = ',1PD12.4,1X,'PHI=',D12.4)
      DO 70 J=1,KL
      MKK=IKL(J)
      MK=IKL(J+1)-1
      J2=2*J
      J1=J2-1
      DO 71 I=MKK,MK
      TE(I)=TP(I)+CON(J1)*TC(I)+CON(J2)*TD(I)
      DTDX(I)=QP(I)+CON(J1)*QC(I)+CON(J2)*QD(I)
   71 CONTINUE
   70 CONTINUE
   36 IF (IPE .EQ. IPP) GO TO 82
      IPI=IPE+1
      DO 86 I=IPI,IPP
      TE(I)=TE(IPE)
      DTDX(I)=DTDX(IPE)
   86 PRINT 4 XX(I), TP(I),QP(I),TC(I),QC(I),TE(I),DTDX(I),P(I),R(I),S(I
     1),IE1(I),IE2(I),IE(I)
C     TEST ON K
   42 IF (ABS((ICT/4-ICT/4.) .GT. 1.E-6) GO TO 142
      PRINT 3
      DO 141 I=1, IP, 10
      PRINT 4 XX(I), TP(I),QP(I),TC(I),QC(I),TE(I),DTDX(I),P(I),R(I),S(I
     1),IE1(I),IE2(I),IE(I)
  141 CONTINUE
  142 CONTINUE
      IF (ABS((CON( 2 )-COLD)/COLD) .GT. EPS ) GO TO 10
  135 PRINT 121
  121 FORMAT (3X,'IT CONVERGES')
  178 PRINT 3
  153 DO 143 I=1,IP,10
  143 PRINT 4 XX(I), TP(I),QP(I),TC(I),QC(I),TE(I),DTDX(I),P(I),R(I),S(I
     1),IE1(I),IE2(I),IE(I)
  133 CALL NTRAN (11,1,IQ,Q,LQ,22)
      IF (LQ .NE. IQ) RETURN
  100 GO TO 21
C
   83 CON(2)=(-QP(IP)-CON(1)*QC(IP))/QD(IP)
  185 KC=KL+1
      CK(KC)=CON( 2)
      IF (IAV .EQ. 1) GO TO 177
      IF (KC .LT. 3) GO TO 81
      KC1=KC-1
      KC2=KC-2
      KC3=KC-3
      IF (CK(KC) .GT. CK(KC1)) GO TO 81
      IF (CK(KC1) .LT. CK(KC2)) GO TO 81
```

```
      IF (CK(KC2) .GT. CK(KC3))GO TO 81
      CKCK=(CK(KC)+CK(KC1))/2.
      IF (CKCK .LE. 3.05) GO TO 81
      IAV=1
177   CONTINUE
      PRINT 132
132   FORMAT (1H , 5X, 'AVERAGE CONVERGENT METHOD IS USED'//)
      KCC=KCC+1
 35   PRINT 11, (CON(JK), JK=1, KL2)
      PRINT 6, CON( 2),COLD
      DO 33 J=1,KL
      MKK=IKL(J)
      MK=IKL(J+1)-1
      J2=2*J
      JI=J2-1
      DO 34 I=MKK,MK
      TE(I)=(TP(I)+CON(JI)*TC(I)+CON(J2)*TD(I)+TE(I))/2.
      DTDX(I)=(QP(I)+CON(JI)*QC(I)+CON(J2)*QD(I)+DTDX(I))/2.
 34   CONTINUE
 33   CONTINUE
145   IF (KCC .LE. 8) GO TO 36
      PRINT 179
179   FORMAT (3X,'NEEDS MORE AVERAGE ITERATION')
      GO TO 178
 74   IF (KL .EQ.KIM) GO TO 84
      IF (KKL .LE. 1) GO TO 29
      MKL=0
      TPI(KL)=TP(I)
      TCI(KL)=TC(I)
      TDI(KL)=TD(I)
      QPI(KL)=QP(I)
      QCI(KL)=QC(I)
      QDI(KL)=QD(I)
      TP(I)=0.
      QP(I)=0.
      TC(I)=1.
      QC(I)=0.
      TD(I)=0.
      QD(I)=1.
      KL=KL+1
      IKL(KL)=I
      IF (IE(I)) 75,75,76
 76   IPE=I-1
      GO TO 85
 29   PRINT 4 XX(I), TP(I),QP(I),TC(I),QC(I),TE(I),DTDX(I),P(I),R(I),S(I
     1),IE (I),IE2(I),IE(I)
      RETURN 0
  3   FORMAT (1H0,6X,'X', 1CX,'TP', 9X,'QP', 9X,'TC', 9X,'QC',1CX,'T',1C
     1),'D1',9A,'P',9X,'R', 7X,'S',8X,'E1',7X,'E2',4A,'K'//)
  4   FORMAT (   (L1)1(.4,1X), 2(E9.4,1X),I1)
      END
JFOR, IS SIMP,SIMP
      SUBROUTINE SIMP (Y,H,IN,Z)
      IMPLICIT DOUBLE PRECISION (A-H, O-Z)
```

```
      DIMENSION Y(201)
      Z=0.
      IF (IN-2) 2, 3, 4
   4  V=H/3.
      DO 1 I=3, IN, 2
   1  Z=Z+(Y(I-2)+4.*Y(I-1)+Y(I))*V
      AIN=IN
      B=AIN/2.
      M=IN/2
      D=B-M
      IF (D .GT. .1) GO TO 2
   3  Z=Z+(Y(IN)+Y(IN-1))*H/2
   2  RETURN
      END
.FOR,IS DERI,DERI
      SUBROUTINE DERI(TK,DTDX)
      IMPLICIT DOUBLE PRECISION (A-H,O-Z)
      DOUBLE PRECISION LAMDAC, LAMDAR, K2I
      PARAMETER IP=1201
      COMMON /SUMKL/ FC(IP),GC(IP),HC(IP),SKL(IP),FKL(IP),IT,TC,FLUX,A(
     )IP),RADIUS
      COMMON DADT,DBDT,D2ADT,D2BDT,DCDT,H,C
     1,LAMDAC, LAMDAR, DLCDT,DLRDT,D2LCDT,D2LRDT,PHI,DKLDT,DPDT,AJ,AJC,
     2DJDT,DJCDT
      COMMON/AAX/AX
      T=TK
      X=1./T
C
C     A=5.03636E11*(T/1.E4)**2CM**2/SEC**2
      DADT=1.00726E12*T
      D2ADT=1.00726E12
      FORMAT(' DADT = ',1PE13.4,' D2ADT = ',1PE13.4)
C
C     B=LAMDAC + LAMDAR
C     LAMDAC=.129E7/COSH(5.*(T/1.E4-1.45)) ERG/SEC-CM-DEGK
C     LAMDAR=1.164E7*(T/1.E4)**3/K2*EXP(-UI)*(UI**4+4.*UI**3+12.*UI**2
C           +24.*UI+24.) ERG/SEC-CM-DEGK
C     UI=12.65/(T/1.E4)
C     K2=1.774(T/1.E4)**(-.71) CM**(-1)
C
      IF (T .GT. 1.75D3) GO TO 21
      BEX=EXP(AX*(T-1.75))
      B=2.2D8*BEX
      DBDT=AX*B
      D2BDT=AX*DBDT
      GO TO 22
  21  TT=T
      IF (T .GT. 3.D3) TT=3.D3
      BEX=EXP(3.*(TT-1.75))
      B=2.2D8*BEX
      DBDT=3.*B
      D2BDT=3.*DBDT
  22  CONTINUE
      HCOS=COSH(5.*(T-1.45))
```

```
      LAMDAC=.12957/(COS
      HSIN=SINH(5.*(T-1.45))
C     COMPUTE DCDT=DKLDT*PHI+DPDT*KL-DJDT
C
   41 T4=T**4
      T3=T**3.34
      TC4=TC**4
      AJ=5.7834E8*T*T3*(T4-TC4)
      AJCC=7.46309/RADIUS**2
      AJC=AJCC   *(ATAN(HSIN)-ATAN(SINH(5.*(TC-1.45))))
      C=FLUX-AJ-AJC
      DJCDT=2.9/RADIUS**2*LAMDAC
      DJDT=5.7834E4*(T3*(8.34*T4-4.34*TC4))
      DCDT=-(DJDT+DJCDT)*1.D4
    9 FORMAT(' PHI = ',1PE13.4,' DKLDT = ',E10.4,' DPDT = ',E10.4,' FK
     1= ',1PE10.4,' DJDT = ',1PE10.4,' DCDT = ',E10.4)
   11 FORMAT(' AJ = ',1PE10.4,' AJC = ',E10.4,' C = ',E10.4
     1.' DJCDT = ',E10.4)
   12 FORMAT(1H , 15E8.3)
C
      RETURN
      END


A FIN
```

APPENDIX C

APPROXIMATE TREATMENT OF RADIAL EXPANSION

According to Baker[21] the radial position of a cylindrical blast wave is given by the formula

$$R_s = \sqrt{R_o a_o t} \qquad , \qquad (C-1)$$

where R_o is the characteristic radius, a_o is the speed of sound in the ambient air, and t is the time, extrapolated to the time that the shock was hypothetically initiated at a line source.

If we assume that the radial velocity of a mass element behind the shock is proportional to its radial position,

$$u(r) = \frac{\dot{R}_s r}{R_s} , \qquad (C-2)$$

then

$$u(r) = \frac{r}{2t} \qquad . \qquad (C-3)$$

The change in mass in a cylindrical volume of radius R and length ℓ is given by

$$m = \rho u(R) S \qquad , \qquad (C-4)$$

where ρ is the density (assumed constant in the cylinder) and S is the curved surface of the cylinder. From this formula we get

$$\dot{m} = \rho \frac{R}{2t} 2\pi R\ell$$

$$= m/t \qquad , \qquad (C-5)$$

103

where m is the mass in the volume of interest.

The time for a blast wave to reach R after being initiated at a line source is

$$t_0 = \frac{R^2}{R_o a_o} \qquad (C-6)$$

The characteristic radius is given by Baker as

$$R_o = \sqrt{\frac{4E_o}{B\gamma p_o}} \quad , \qquad (C-7)$$

where E_o is the internal energy per unit length in the blast source, p_o is the ambient pressure, γ is the ratio of specific heats, and B is a function of γ. For air, $\gamma \approx 5/2$, and, therefore, from Baker, $B \approx 4$. For a perfect gas

$$E_o = (\gamma-1)^{-1} kT \quad R^2 \rho_o$$

$$= (\gamma-1)^{-1} p \pi R^2 \rho_o \quad , \qquad (C-8)$$

where p is the pressure, T is the temperature, and ρ_o is the density of the gas behind the shock, at the time t_o, i.e., when the shock is assumed to be started at R. Therefore,

$$R_o = R\sqrt{\frac{\pi \rho_o}{\gamma(\gamma-1)} \frac{p}{p_o}} \quad , \qquad (C-9)$$

and from Equation (C-6),

$$t = t_o + t'$$

$$= \frac{R}{a_o}\sqrt{\frac{\gamma(\gamma-1)}{\pi \rho_o} \frac{p_o}{p}} + t' \quad , \qquad (C-10)$$

where t' is the is the time after shock is initiated at radius R.

The difference equations presented in Section 3.4 are modified in the following way:

1. The continuity equation (Eq. 3.10 of Chapman)[20] has $\dot{m}_j^{n+1}$ added to the right side.

2. The momentum conservation equation (Eq. 3.1 of Chapman) has $\dot{m}_j^{n+1} u_j^{n+1}$ added to its right side.

3. The energy conservation equation (Eq. 31) has $\dot{m}_j^{n+1} e_j^{n+1}$ added to its right side.

These equations are then solved iteratively until convergence at time t^{n+1} is achieved.

Since $\dot{m}$ is a weak function of the pressure, it is assumed that only one shock is propagating from an element at any one time. The shock is initiated whenever the ratio p/p_o is larger than some value η_{on}, and is turned off when the pressure ratio returns to some other value η_{off}, where $\eta_{on} > \eta_{off}$.

APPENDIX D

A QUALITATIVE DESCRIPTION OF
LASER-INDUCED BREAKDOWN

In order to obtain a qualitative theoretical description of the breakdown process, it is necessary to consider the equations which govern the electron density and electron energy gain and loss processes in the laser field. It can be shown that the electron continuity and energy conservation equations can be written respectively as:

$$\frac{dN_e}{dt} = (\nu_i - \nu_a)N_e - D\nabla^2 N_e - \alpha_R N_e^2 \qquad (D-1)$$

and

$$\frac{d\varepsilon}{dt} = \left[\frac{e^2 E^2}{m(\omega^2 + \nu_e^2)} - \frac{2m}{M}\varepsilon\right]\nu_c - I_p\nu_i \qquad (D-2)$$

Here

ν_i = ionization rate

ν_a = attachment rate

D = diffusion coefficient

α_R = recombination rate

E = laser electric field strength

m = electron mass

ω = laser frequency

ν_c = electron collision frequency

I_p = ionization potential

N_e = electron number density

ε = electron energy .

In Equation (D-1), the electron density increases due to ionizations, and decreases due to attachment, diffusion and recombination processes. As shown in Equation (D-2), we consider the electron energy to increase due to inverse bremmstrahlung and to decrease by elastic collisions with atoms (and ions) and by inelastic processes which are here limited to ionization.

At the start of the process, the number of electrons in the cascade increases exponentially, i.e., the rate of change of electron density is approximately constant. Neglecting recombination during this early phase, it can be shown that Equation (D-1) reduces to

$$\frac{N_e(t)}{N_o} = \exp\{\nu_i - \nu_a - D/\Lambda^2\}t = 2^k \qquad , \qquad (D-3)$$

where k is the number of electron generations produced during time t. It is common to assume that breakdown occurs once some critical number of electrons, N_{cr}, is formed or equivalently after some critical number of electron multiplications, k_{cr}, is attained. Accordingly, we find from Equation (D-3),

$$\nu_i \simeq \frac{D}{\Lambda^2} + \nu_a + \frac{(\ln 2)k_{cr}}{\tau_p} \qquad (D-4)$$

where we have defined τ_p as the laser pulse time required to create breakdown, i.e., to generate $N_e = N_{cr}$.

The breakdown threshold can now be defined by use of the energy balance equation and requiring that during the laser pulse time, τ_p, over which the electron number density has increased to N_{cr}, that sufficient energy has been added

107

to the electron gas to create that number of electrons and to balance any other energy losses which may have occurred. Accordingly, combining Equations (D-2) and (D-4), we find for the breakdown laser, flux, F_t,

$$F_t = \frac{ncI_p(\omega^2+\nu_c^2)}{4\pi e^2\nu_c} \left\{ \frac{k_{cr}\ln 2}{\tau_p} + \nu_a + \frac{\mathcal{D}}{\Lambda^2} + \frac{2n\bar{\varepsilon}\nu_c}{I_p^{:1}} \right\} \quad . \quad (D-5)$$

Here, we have used the relationship between the laser flux F and the electric field strength E;

$$E = \left(\frac{4\pi F}{c}\right)^{1/2} \quad . \quad (D-6)$$

In order to obtain Equation (D-5) we have assumed a "square" laser pulse and an average constant value for both ν_c and $\bar{\varepsilon}$ over that pulse.

For gas breakdown, one can obtain limiting behavior and approximate scaling information from Equation (D-5). For instance, for very short laser pulses, the first term in the brackets dominates the equation and we find

$$F_t \alpha \frac{I_p(\omega^2+\nu_c^2)}{\nu_c} \frac{k_{cr}}{\tau_p} \quad (D-7)$$

In this limit, breakdown is limited by the amount of energy necessary to ionize the gas $(k_{cr}I_p)$. The breakdown flux increases as τ_p decreases. This is the constant energy regime.

For long pulses, the energy loss terms become dominant and we find that

$$F_t \alpha \frac{(\omega^2+\nu_c^2)}{\nu_c} \frac{\bar{\varepsilon}}{\tau_{loss}} \quad (D-8)$$

where τ_{loss} is some characteristic loss time. This is the
limit commonly referred to as the constant flux limit of
breakdown. In this limit, the flux to break the gas down is
a constant since the energy loss rate due to diffusion,
attachment and inelastic processes increase as the pulse
length increases.

This simple picture of breakdown works fairly well, at
least qualitatively for the case of clean air. However, due
to particle interaction, the picture becomes more complicated
This is primarily due to the fact that one must now consider
the electron cascade evolution in a heated material, such as
vapor or air, subject to rapid hydrodynamic expansion rates.
In this case, the energy loss processes themselves are a func-
tion of the pulse time, thus negating the long pulse, constant
flux limit. Furthermore, it is expected (and observed) that
additional losses depending on the particle size and number
density distribution incorporate additional losses which result
in a regime intermediate between the constant energy and con-
stant flux regime.

The only real conclusion to be reached at this point
is that the concept of simple scaling with wavelength in the
case of breakdown in particle laden atmospheres is very compli-
cated. However, there are no experimental data available to
guide or confirm the model at wavelengths other than 10.6μ.*
Clearly, such data would be extremely useful in obtaining
and validating a model from which simple scaling information
may be derived. Experimental data at 1.06 μ are presented in
Chapter 4.

---

* Since the performance of the work described in Chapter 4, some
data obtained by Lencioni at Lincoln Laboratories have become
available at 1.06μ; c.f., Appl. Phys. Lett. <u>25</u>, 15 (1974).

REFERENCES

1.   Bunkin, F.V., V.I. Konov, A.M. Prokhorov and V.B. Fedorov, "Laser Spark in the Slow Combustion Regime," JETP Letter 9, 371 (1969).

2.   Generalov, N.A., V.P. Zimakov, G.I. Kozlov, V.A. Masyukov and Yu. P. Raizer, Soviet Physics JETP 34, 763 (1972).

3.   a. Klosterman, E.L., S.R. Byron and J.F. Newton, "Laser Supported Combustion Wave Study," Mathematical Sciences Northwest, Inc., Report MSNW No. 73-101-3, Feb. 1973.

      b. Klosterman, E.L., and S.R. Byron, "Experimental Study of Subsonic Laser Absorption Waves," MSNW Report No. 73-101-4, Dec. 1973.

4.   Raizer, Yu. P., "Subsonic Propagation of a Light Spark and Threshold Conditions for the Maintenance of Plasma by Radiation," Soviet Physics JETP 31, 1148 (1970).

5.   Boni, A.A. and F.Y. Su, "Propagation of Laser Supported Deflagration Waves," (To be published by Phys. of Fluid) (1974).

6.   Boni, A.A. and F.Y. Su, "Subsonic Propagation of Laser Supported Waves," presented in AIAA 7th Fluid and Plasma Dynamics Conference, Palo Alto, CA., June 17-19, 1974, AIAA 74-567.

7.   Bellman, R.E. and R.E. Kalaba, Quasilinearization and Nonlinear Boundary-Value Problems, American Elsevier Publishing Co., N.Y. (1965)

8.   Radbill, J.R., "Applications of Quasilinearization to Boundary-Layer Equations," AIAA 2 (10), 1860 (1964).

9.   Libby, P.A. and K.K. Chen, "Remarks on Quasilinearization Applied in Boundry Layer Calculation," AIAA 4, 937 (1966).

10.   Libby, P.A. and T.M. Liu, "Some Similar Laminar Flows Obtained by Quasilinearization," AIAA 6 (8), 1541 (1968).

References (Continued) -

11. Zeldovich, Ya. V. and Yu. P. Raizer, Physics of Shock Waves and High-Temperature Hydrodynamic Phenomena, Vol. 1, Academic Press, N.Y. (1966) .

12. Allen, R.A., "Air Radiation Graphs: Spectrally Integrated Fluxes Including Line Contributions and Self Absorption," AVCO-Everett Research Report No. 230 (1965).

13. Burnwell, R.W., "Inviscid Radiating Shock Layers About Spheres Traveling at Hyperbolic Speed in Air," NASA TR R-311 (1969).

14. Su, F.Y. and D.B. Olfe, "Radiation Effects on Reflected Shock Waves, I., Transparent Gas," Phys. Fluid 14, 2636 (1971)

15. Predvoditelev, A.S., E.V. Stupochenko, E.V. Samuilov and I.P. Stakhonov, Tables at Thermodynamic Function of Air for Temperature 6000° to 12,000°K and Pressure from 0.001 to 1000 atm., and 12,000° to 2,000°K and 0.001 to 1,000 atm., Associated Technical Services, Glen Ridge, N.J. (1962).

16. Hanson, C.F., "Approximations for the Thermodynamic and Transport Properties of High Temperature Air," NASA TR R-50 (1959).

17. Boni, A.A., H.D. Cohen and F.Y. Su, "A Theoretical Description of the Interaction of an Intense Laser Beam with a Solid Target, Part II," Systems, Science and Software Research Report SSS-R-73-1860 (1973).

18. Mitchell, A.R., "Computational Methods in Partial Differential Equations," John Wiley & Sons Ltd., London (1969).

19. Murphy, G.M., "Ordinary Differential Equations and Their Solutions," D. Van Nostrand Co., N.Y.(1960).

20. Chapman, M., "HELVA, A One-Dimensional Hydrodynamic Computer Code", Systems, Science and Software Topical Report SSS-R-74-2027 (1974).

21. Baker, Wilfred E., Explosions in Air, University of Texas Press, Austin, Texas (1973).

References (Continued):

22. Triplett, J. R. and A. A. Boni, "The Interaction of Suspended Atmospheric Particles with Laser Radiation," Systems, Science and Software Report SSS-R-71-1167, (June 1972). Also published as Air Force Weapons Laboratory Report AFWL-TR-72-102 (1972).

23. Nielsen, P. E. and G. H. Canovan, AFWL Laser Division Digest, LRD-71-1, Air Force Weapons Laboratory, Kirtland AFB, NM (1971).

24. Schlier, R. E., A. N. Pirri and D. J. Reilly, Air Force Weapons Laboratory Technical Report AFWL-TR-72-74 (1973).

25. Lencioni, D. E., L. C. Margnet, R. J. Hull, H. Kleiman, J. E. Lowder and R. W. O'Neil, "The Effect of Dust on 10.6 µm Laser Induced Air Breakdown," Lincoln Laboratory Project Report LTP-20 (1973).

26. Smith, D. C., R. T. Brown, F. G. Gebhardt, and P. J. Beyer, "Effects of Particulate Matter on Atmospheric Propagation of CO_2 Laser Radiation," United Aircraft Research Laboratories Report M921503-3 (1973).

27. Boni, A. A., F. Y. Su, J. R. Triplett, "A Theoretical Description of the Interaction of an Intense Laser Beam with a Solid Target," Systems, Science and Software Report SSS-R-73-1510 (1973).

28. Ready, J. F., Effects of High-Power Laser Radiation, Academic Press, N.Y., p. 220, (1971).

29. Lencioni, D. E., "The Effect of Dust on 10.6 µm Laser-Induced Air Breakdown," Appl. Phys. Lett. 23, 12 (1973).

30. Lencioni, D. E., "Laser-Induced Air Breakdown for 1.06 µm Radiation," Appl. Phys. Lett. 25, 15 (1974).

31. Ireland, C. L., A. Yi, J. M. Aron, and C. G. Morgan, Appl. Phys. Letters 24, 175 (1974).

32. MacPherson, R. W. and M. Gravel, "Segmented Dielectric Breakdown of Air by the Focused Radiation from a Mole Locked CO_2 TEA Laser," Optics Communications 4, 160 (1972).